SCUOLA DI DOTTORATO

UNIVERSITÀ DEGLI STUDI DI MILANO-BICOCCA

Dipartimento di / Department of

Scienza dei Materiali

Dottorato di Ricerca in / PhD program Scienza e Nanotecnologia dei Materiali Ciclo / Cycle XXX

Catalytic Properties of Zirconia: Role of Nanostructuring and Metal-Oxide Interface

Cognome / Surname Ruiz Puigdollers Nome / Name Antonio

Matricola / Registration number 798880

Tutore / Tutor: Prof. Gianfranco Pacchioni

Coordinatore / Coordinator: Prof. Marco Bernasconi

ANNO ACCADEMICO / ACADEMIC YEAR 2016/2017

The important thing is to not stop questioning.
Curiosity has its own reason for existing.

Albert Einstein

This thesis has been realized within the European Seventh Framework Programme – Marie Curie Initial Training Network **CATSENSE** 2014 – 2017, with grant agreement number 607417.

The goal of CATSENSE is to design novel high performance catalysts and biosensors based on gas-phase and supported metal clusters. It aims to accelerate the pace of discovery of novel nanomaterials.

Partners: Katholieke Universiteit Leuven (coordinator), University of Birmingham, Danmarks Tekniske Universitet, Università degli Studi Milano-Bicocca, Tel'Aviv University, Università degli Studi di Milano, Miba - Teer Coatings Ltd., Johnson Matthey, and IK4-Cidetec.

Abstract

Catalysis, the conversion of chemical species facilitated by a suitable catalyst, has been present in our society since ancient history, being nowadays involved in the production of around the 90% of chemicals. For this reason, catalysis is one of the widest and most active research fields in the scientific community, driven by the search of novel and more efficient catalysts for the chemical reactions indispensable for life.

Density functional theory (DFT) is a computational approach widely applied in heterogeneous catalysis. It is well suited to treat relatively big systems, and can provide a better understanding of active sites and reaction mechanisms at the atomic scale. In this thesis, we present a DFT study of the catalytic properties of an oxide widely used in catalysis: zirconium dioxide. We have investigated how the properties of zirconia are modified by two main aspects: by nanostructuring and by the presence of a metal-oxide interface, focusing in particular on the changes in the reducibility character of this oxide. Zirconia is hardly reducible oxide. However, we demonstrate that nanostructuring and metal-oxide interfaces greatly improve this property. First, we show that 1 – 2 nm zirconia nanoparticles show lower formation energies for O vacancies than bulk zirconia, via both the direct desorption of O_2 and the desorption of H_2O from the hydrogenated nanoparticle. Also, O-deficient zirconia nanoparticles are shown to be ferromagnetic at room temperature. Regarding the creation of a metal-oxide interface, we have investigated the bonding properties of Au and Ag clusters on stoichiometric and defective zirconia. Au particles deposited on zirconia promote the formation of O vacancies at the Au-ZrO_2 interface. On this basis, we studied the catalytic cycle of the CO oxidation reaction on a Au/ZrO_2 catalyst through a Mars van-Krevelen mechanism. Finally, we investigated the reducibility properties of a metal-supported zirconia thin film, a system that combine oxide nanostructuring and a metal-oxide interface.

Keywords

Catalysis, zirconia, nanostructuring, metal-oxide interface, metal clusters, gold, thin films, density functional theory

Italian Abstract

La catalisi, ossia la conversione di specie chimiche facilitata da un catalizzatore adeguato, è presente nella nostra società dai tempi antichi. Oggi, è necessaria per la produzione di circa il 90% dei prodotti chimici. Per questa ragione, la catalisi è uno dei più estesi e attivi campi di ricerca della comunità scientifica che è motivata dallo sviluppo di nuovi e più efficienti catalizzatori per le reazioni indispensabili per la vita.

La teoria del funzionale della densità (DFT) è un approccio computazionale molto usato nella catalisi eterogenea. Questo metodo è adatto per trattare sistemi relativamente grandi, e può fornire una migliore comprensione atomistica dei siti attivi e dei meccanismi di reazione. In questa tesi si presenta lo studio DFT delle proprietà catalitiche di un ossido ampiamente usato in catalisi: il diossido di zirconio. Abbiamo studiato come le proprietà della zirconia possono essere modificate da due aspetti: dalla nanostrutturazione e dalla presenza di un'interfaccia metallo-ossido, focalizzandosi particolarmente sulle variazioni della sua riducibilità. La zirconia è, infatti, un ossido difficilmente riducibile. Dimostriamo che la nanostrutturazione e l'interfaccia metalo-ossido migliorano notevolmente questa proprietà. Inizialmente mostriamo che nanoparticelle di 1 – 2 nm hanno delle energie di formazione di vacanze di ossigeno più piccole di quelle nel bulk, sia per il diretto desorbimento di O_2 sia per il desorbimento di H_2O dalla superficie idrogenata. Inoltre, si trova che le nanoparticelle di zirconia deficienti in ossigeno sono ferromagnetiche a temperature ambiente. Per quanto riguarda la creazione dell'interfaccia metallo-ossido, sono investigate le proprietà di legame di cluster di Au e Ag su entrambe le superfici di zirconia stechiometrica e diffettiva. Particelle di Au depositate su zirconia promuovono la formazione di vacanze di ossigeno nell'interfaccia Au-ZrO_2. Su questa base, abbiamo studiato il ciclo catalitico della reazione di ossidazione della CO su un catalizzatore Au/ZrO_2 attraverso un meccanismo Mars van-Krevelen. Infine, sono investigate le proprietà di riducibilità di un film sottile di zirconia supportato su metallo, un sistema che combina nanostrutturazione e interfaccia metallo-ossido.

Acknowledgements

Firstly, I would like to express my sincere gratitude to my advisor Prof. Gianfranco Pacchioni for his support and guide. His advices and immense knowledge have been invaluable.

I also want to thank Prof. Francesc Illas from Barcelona for an interesting and productive collaboration, and above all, for offering the possibility to do this PhD.

Thanks to my colleagues Dr. Elisa Albanese, Dr. Philomena Schlexer, Dr. Hsin-Yi Tiffany Chen, Dr. Lara Ferrighi, Dr. Sergio Tosoni, Dr. Daniele Selli, Gianluca Fazio, Martina Datteo and Kostanza Ronchi, for so many interesting discussions and Italian lessons.

Thanks to my family and friends from Barcelona, specially to my mother, for her everyday support and advices.

Finally, thanks to Jordi, who directly made possible this work.

CONTENTS

Chapter 1

Introduction

1 Introduction to Catalysis

The word catalysis was first introduced by Baron J. J. Berzelius in 1835. He was describing that capacity of some substances or materials, called catalyst, of facilitating chemical reactions without being consumed. In other words, he was describing materials with a catalytic activity that makes possible to perform a chemical reaction at softer conditions than in the absence of them, for instance at lower temperatures and/or lower pressures. The reason is that a catalytic material affects the rate of the reaction, but the chemical composition at the equilibrium is always determined only by the thermodynamics.

Clearly, the use of a catalyst supposes more benefits than the use of another substance that takes part in the reaction stoichiometrically. For example, the energy consumption is largely reduced, which permits to save fuel costs; the energy saving brings to reduce the environmental impact of the whole process. Also, the catalyst is not consumed during the process and can be used continuously in many reactions. The last point, however, would be the ideal case, but this is not always the real situation: there are factors that can decrease the activity or selectivity of a catalyst in time, as it will be seen later.

Nowadays, catalysis is indispensable for the production of fuels and of around the 90% of the fine chemicals, in their transportation, and for environmental cleaning. In fact, it has been present already 8000 years ago, starting in ancient Egypt and Mesopotamia. An example is the use of yeast for the fermentation of the sugar in grain or grapes to produce ethanol. However,

the first recognition of heterogeneous catalysis occurred in 1813, when L. J. Thénard obtained N_2 and H_2 by decomposition of NH_3 onto heated Fe, Cu, Ag, Au, and Pt catalysts.[1] In the following years, the research for pure transition metals that catalyze simple reactions started to increase.[1] The best example of the social impact that can have the research for efficient catalysts has been the synthesis of ammonia. In the beginning of the XX century, the supplies of NH_3 were insufficient for the world's fertilizer industry. The scientific community was appealed to develop a method of fixing atmospheric N_2 to solve the problem. Catalysts as simple as Os, Ur, and Fe_3O_4 were tested, but the final formulation achieved was Fe supported on 2.5-4% Al_2O_3, 0.5-1.2% K_2O, 2-3.5% CaO and 0-1% MgO, still used today. The industrial process known as the Haber-Bosch process was finally applied in 1911, producing 18 kg of ammonia per day.[2] Today's world production is more than 160 metric tons per year. This process has had a big impact on the efficiency of the agricultural production in the world. Without it, the global population could not be sustained. In other words, the population growth of the second half of the XX century would not have occurred. This is illustrated in Figure 1.1, where the population growth is correlated with the growth in the production of ammonia. Also, there is a comparison with an estimation of the population growth if the Haber Bosch process had not been developed. In this hypothetic case, the world's population grows gradually and increases from around 1800 million in 1900 to around 3500 million in 2000, while in reality the population has been triplicated in those 100 years –from around 1800 to 6000.[3]

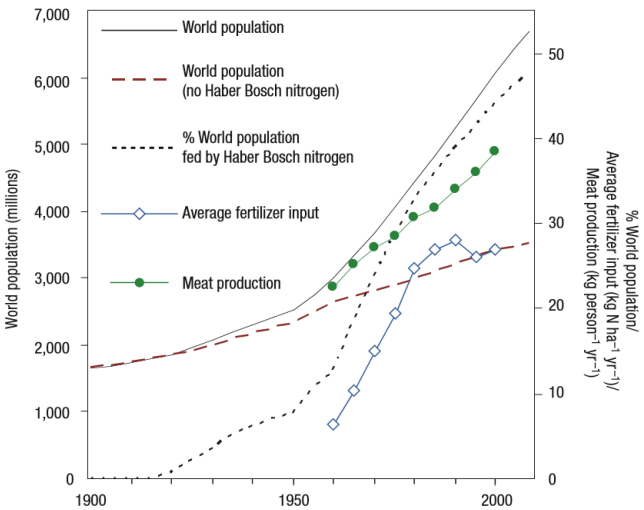

Figure 1.1 Growth of world's population and nitrogen consumption in the XX century. From Ref. 3

Another example of a catalytic process very important in everyday life is the oxidation of CO to CO_2 over metals. Motor vehicles are provided of catalytic converters that consist of a metal casing with Pd and Rh on an oxide support. The combustion gases –CO and unburned hydrocarbons– react on Pd with O_2 to form CO_2 and H_2O. Also, N_2O and NO, present also in the exhaust gases, react on Rh with the CO to form CO_2 and N_2.

1.1 Heterogeneous Catalysis

There are mainly three types of catalysis, depending of the form of the catalytic species. Homogeneous catalysts are present in the same phase as reactants and products, usually in a liquid solvent. Enzymes are organic macromolecules that catalyze biological reactions, usually used as homogeneous catalysts. Heterogeneous catalysts, however, are present in a different phase than the chemical reactants and products, usually in the solid phase. This provides some key advantages: the catalyst separation is easier, and there is a higher tolerance to extreme operating conditions. For these reasons, this type of catalysis is favored in industry.

A heterogenous catalytic reaction implies the adsorption and activation of the reactant species. A strong chemical bond is formed, which is called chemisorption, with energies usually between 80 and 400 kJ/mol (0.8 – 4 eV). Once the surface sites are being occupied, no molecules can be adsorbed, so only a monolayer of chemisorbed species is possible. Then, this catalytic process provides an alternative but more complex sequence of elementary steps compared to the same reaction in the gas phase (Figure 1.2). Also, reactants or products can be weakly adsorbed by van der Waals forces, which is called physisorption, with energies between 20 and 50 kJ/mol (0.2 – 0.5 eV). Physisorbed states may serve as precursor states of chemisorption. In this case, however, more than one monolayer can be adsorbed on the surface.

The reaction can occur on the catalyst surface when all reactants are adsorbed, which is known as the Langmuir-Hinselwood (LH) mechanism. Instead, in the Eley-Rideal (ER) mechanism, a reactant from the gas phase reacts with the adsorbed species. The LH mechanism is preferred due to the extremely short time scale of the adsorption of the species from the gas phase (picoseconds). On the other hand, ER is possible at extreme conditions, for instance in reactions during plasma processing of electron materials.[4] The reaction between reactants occurred on the surface (at least one of them is adsorbed) is called the rate determining step

(RSD), as most part of the free energy of the overall reaction comes from this step. The other steps like adsorption, desorption, and diffusion are assumed to be quasi-equilibrated.

There are some properties that are required to be a good and efficient catalyst. The reaction must proceed at a suitable rate under the economically desirable conditions, that is, yield the expected quantity of desired product per unit of time. This defines the catalytic activity. As the desired product is formed in the active sites, the activity of the catalyst depends on the fraction exposed of these sites. Measuring the number of exposed sites allows reaction rates to be normalized to the quantity of active component. Then, the activity of a catalyst can be measured by the turnover frequency (TOF), or the rate expressed per active site. As it will be seen later, one way to increase the activity is by increasing the effective surface area exposed by nanostructuring the catalyst, for example by finely dispersing small clusters or nanoparticles of the catalyst on a support. This is known as nanocatalysis.

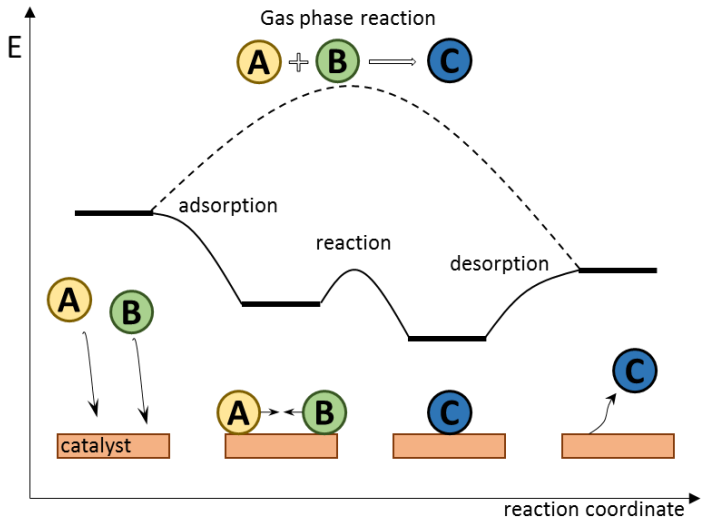

Figure 1.2 Schematic representation of the potential energy diagram for a reaction on a heterogeneous catalysis compared to that on the gas-phase.

One of the major problems related to heterogenous catalysis is the catalyst deactivation. Unwanted side products are usually formed during the process and may lead to the loss of activity, that is, to the deactivation of the catalyst or poisoning. This process usually occurs simultaneously with the wanted chemical reaction. For example, carbon is deposited on the surfaces during the catalytic cracking of gas oil, which poisons the catalyst as it blocks the

active sites. It has both a physical and chemical nature, in which an impurity or poison, is strongly chemisorbed usually in an irreversible way on the active sites, hindering the wanted reaction to occur on them. It also affects the selectivity, for instance in a catalyst where different types of adsorption sites lead to different products.[5] So, the largest ratio between the desired product and the side products is expected for a good catalyst, which is known as selectivity. Also, the adsorption enthalpy of the reactants must be sufficiently exothermic to be chemisorbed. However, it should not be so strong that the further reaction cannot proceed. The same occurs with the products formed; they should be able to desorb from the catalyst. An important example of this is the great reactivity of ZrO_2 surfaces with the CO_2 molecule. This molecule forms very stable bidentate and polydentate carbonates (CO_3^{2-}) on the ZrO_2 surface at room temperature.[6,7,8,9] This process affects ZrO_2-based catalysts in the CO oxidation reaction by two ways: first, the main product, CO_2, is not totally desorbed, and second, the surface carbonates block part of the active sites poisoning the catalyst. On the other hand, poisoning may also be used positively to adjust the selectivity of the catalyst, for example, by 'blocking' with the poison species those adsorption sites that perform an undesirable reaction.

The enormous necessity in industry and environmental applications for efficient catalysts has been driving scientists to continuously investigate how to improve the activity and selectivity of new materials. As it has been seen, initially the studied catalysts were pure metal particles. To increase the exposition of the active sites, these were finely divided and deposited on supports, which have been for a long time thought to be inert in the reaction of interest. Several parameters affect the catalytic properties of these particles, like the size, shape, surface composition, and oxidation state. However, from the second half of the XX century, many researchers started to realize that supports are no longer inert and play a fundamental role in the catalysis, which brings a number of new parameters that affect the activity and selectivity increasing the complexity of the catalytic mechanisms. For example, the support can influence the activity of the deposited catalyst by modifying its mechanical stability, morphology, by inducing strain, by enabling spillover, and by changing the electronic structure by charge transfer processes.[10] These factors will be more detailed later.

When the catalyst particle is deposited onto a substrate, three mainly types of bond can be formed. (1) A weak bond can be formed dominated by dispersion forces and polarization effects. In fact, this type of bond is always present. (2) A covalent bond can be formed by chemical mixing of the electronic states of adsorbate and substrate. (3) An even stronger bond can be formed by electrostatic interaction after charge transfer between both systems (redox process). Sometimes, the three types can occur simultaneously for the same pair adsorbate-substrate by only changing the adsorption site. Covalent and polar bonds maintain the electronic configuration of the adsorbate as in the gas phase, with only energy shifts of the electronic states due to the interface interaction. However, a charge transfer process changes the electronic configuration of both systems. The relative position and overlap between the states of the two interacting systems determines the direction and extent of the charge transfer. This is of fundamental importance in fields like electrochemistry, photocatalysis, and molecular electronics.[11]

So, heterogeneous catalysis is a very wide research field as numerous parameters and properties can be studied and controlled to design a catalyst. This research can be approached from different topics. Nanoscience is described as the evolutionary outgrowth of surface science, focusing on solid surfaces, interfaces, and gas-solid interaction. Nanotechnology is viewed as the application of the surface science. Catalysis by supported metals can be considered one of the first examples of nanotechnology.[12,13] Surface (and interface) science works in the 0.01 – 10 nm size range in the single dimension perpendicular to the surface, involving solid-gas (or vacuum), and solid-solid interfaces, never liquids or soft matter. Nanoscaling is restricted to the normal direction and spatially extended in the other two dimensions. In nanoscience and nanotechnology, materials are nanoscaled in two dimensions, becoming 1D materials (nanowires), or in three dimensions, like 0D materials (nanoparticles). The synthesis of nanostructures is currently one of the most active fields in nanoscience. However, the control of atoms and molecules is still a challenge.

1.1.1 Computational Chemistry in Catalysis

In the last decades of the XX century, experimentalists have been able to make great advances in catalysis by elucidating the structure of practically all materials like metals, semiconductors, carbon allotropes, etc. However, the complexity of real catalytic systems makes difficult to

identify the underlying mechanisms at the atomic level. A better understanding and characterization at the atomic level has been possible thanks to the joint work between new techniques of spectroscopy and microscopy with parallel advances in computers and algorithms that have made possible the computational treatment of big and more realistic chemical systems.

Theoretical simulations can have different levels of sophistication depending on the complexity of the system and expected accuracy. New algorithms and powerful computer machines are able to approach more complex structures and phenomena, although for a better understanding, many times is useful to break up such big systems into simpler ones. Among the different computational methods, the density functional theory (DFT) is the one that has most enhanced the development of the calculations in condensed matter physics. DFT methods can provide an atomic-level understanding of different aspects like the electronic and chemical properties of the catalysts, the metal-support interaction, size effects, co-adsorption of non-participant species, and the characterization of the catalytic active sites, all information that cannot be easily accessible by the experiment. So, computations can be potentially used to lead experiments and to rationalize measured data and examine models based on them.[14,15,16]

2 Oxides in Catalysis

2.1 Metal Oxide Materials. Reducibility Properties

Metal oxides constitute a class of materials with a wide range of properties that cover all aspects of material science and physics. They can be covalent or highly ionic; exhibit a semiconducting, insulating, or even a metallic behavior. Such broad spectrum of different functionalities and chemical activities, combined with their intrinsic stability, makes oxides very interesting materials for catalysis, photovoltaics, and electronics. In heterogeneous catalysis, oxides can be used as inert (inactive) supports for deposited metal particles (active), or as active catalysts, where active sites of the oxide are able to exchange or adsorb chemical species from the environment. In the latter case, the great flexibility of oxides surface reactivity stems from the presence of Lewis and Brønsted acid and basic sites, whose acidic or basic character is related to the reducible character of the oxide.

Nonreducible oxides, like SiO_2, MgO, Al_2O_3, ZrO_2, etc. are materials that do not easily lose oxygen, due to the intrinsic resistance of the corresponding metal cations to change the

oxidation state. Typically, these materials are characterized by a large band gap (> 3 eV) separating valence (VB) and conduction bands (CB). As oxygen is formally in a -2 oxidation state (O^{2-} ions), the two electrons left in the oxide by removal of a neutral O atom cannot be accommodated in the empty states of the metal cations as these lie too high in energy, corresponding to the CB of the oxide. Instead, the extra charge is trapped in specific sites (e.g. in the vacancy left by oxygen) and gives rise to new defect states in the band gap. This process implies a high energy cost. Therefore, nonreducible oxides are highly stoichiometric, stable, and chemically inert.[17,18]

On the contrary, reducible oxides have the capability to exchange oxygen in a relatively easy way. The lowest empty states available on the material (CB) are formed by cation d orbitals that lie at an energy not so far from the VB. This results in a semiconducting character, with band gaps below 3 eV. Thus, upon removal of oxygen, the excess electrons are redistributed on the cation empty levels, reducing their oxidation state from Mn^{n+} to $M^{(n-1)+}$. Examples of reducible oxides are TiO_2, WO_3, NiO, Fe_2O_3, CeO_2, etc.

A large fraction of industrial catalysis deals with oxidation or oxidative dehydrogenation reactions. Thus, the reducible character of catalysts is of fundamental importance. The generation of oxygen vacancies on these materials is then a very important aspect in the development and design of catalysts. However, the identification and characterization of oxygen vacancies on oxides is far from trivial. In recent years, several techniques have been developed to identify these centers, like the Scanning Transmission Microscopy (STM) and the Atomic Force Microscopy (AFM).

A better knowledge of the nature of vacancies is important to design materials with tailored properties. Control and engineering of O vacancies is fundamental in fields like photocatalysis,[19] information technology,[20] and gas sensors.[21] Also, the formation of surface vacancies modifies the surface reactivity towards adsorbates due to the appearance of sites with excess electrons. For instance, it has been demonstrated that prereduction in H_2 of a solid catalyst like TiO_2 and ZrO_2 have beneficial effects in reactions of transformation of biomass into fuel,[22,23,24] which is related to the presence of reduced Ti^{3+} and Zr^{3+} centers.[25,26] Also, some studies show that Au supported on reducible supports like TiO_2, Fe_2O_3, Co_3O_4 and NiO is very active for the low temperature CO oxidation reaction.[27,28,29,30,31] On nonreducible oxides like

ZrO_2 and MgO, it is expected to be less active.[32,33] We will demonstrate in this thesis, however, that an enhanced activity driven by O vacancies can be obtained for the Au/ZrO_2 catalyst in the CO oxidation reaction.

All this has prompted the scientific community to develop strategies to improve the reducibility of oxides. In general, there are three main conceptual approaches to improve this property: by doping the oxide with heteroatoms, by nanostructuring the oxide in the form of nanoparticles or thin films, and by depositing metal particles in the surface of the oxide, so a metal-oxide interface is created. These procedures are relatively novel, and in this thesis, we will focus in the last two, nanostructuring and the creation of a metal-oxide interface.

2.1.1 Zirconium Dioxide

This thesis is entirely focused on the chemistry of a particular oxide: the zirconium dioxide or zirconia (ZrO_2). This material is one of the scientifically and technologically most attractive oxides with numerous applications. It finds special attention due to its mechanical properties, stability over a wide range of temperature, and resistance to catalytic poisoning and extreme pH conditions.[34,35,36,37,38,39,40]

Zirconia has a complex polymorphism. It shows three different stable phases. Up to 1175 ºC the most stable one is the monoclinic. It the transforms into the tetragonal phase, stable up to 2370 ºC, and then into the cubic phase.[41,42] The cubic one is a fluorite-type structure; the other two can be viewed as structural distortions from the cubic. The catalytic and mechanical most interesting phase is the tetragonal (t-ZrO_2). Many times, is needed to stabilize this phase at room temperature. For this, divalent and trivalent cationic species like Mg^{2+}, Ca^{2+}, and Y^{3+} are incorporated into the ZrO_2 lattice,[43,44] being the latter case the most common dopant to stabilize t-ZrO_2, called Yttrium-Stabilized Zirconia (YSZ). The tetragonal can also be stabilized in the form of nanostructures, due to the differences in surface free energies in monoclinic and tetragonal nanoparticles.[45] For instance, it is possible to have at room temperature pure t-ZrO2 nanoparticles between 10 and 50 nm[46] and smaller.[47]

Zirconia is considered a nonreducible oxide, like MgO or SiO_2. This is connected to the highly ionic character of bonds and the large band gap (around 6 eV).[48,49] For instance, the removal of a O_{4c} ion from bulk t-ZrO_2 has a cost as large as 6.2 eV, or 6.0 eV from the (101) t-ZrO_2 surface. Such formation energies in the monoclinic and cubic phases are found to be

similar.[50,51] Theoretical investigations reveal that the charge associated to O vacancies is localized in the vacancy site, like F-centers in MgO.[52] However, in this thesis, it will be shown that this is limited to the bulk regime, and nanostructuring and metal-oxide interfaces can change this picture. Recently, the interest for preparing reduced zirconia has increased due to the interesting applications that this material can offer. For example, in the already mentioned transformation of biomass into fuels,[23,24] or in photocatalysis, where oxygen deficient zirconia shows a good activity in producing H_2 under solar light while stoichiometric zirconia is inactive. Also, dopant-free reduced zirconia is found to be ferromagnetic at room temperature,[53,54,55,56,57] a topic that will be investigated in this thesis.

ZrO_2 is employed in numerous scientific and technological areas. It is used as a gate dielectric,[58] in buffer layers for superconductor growth,[59,60] in thermal barrier coating materials,[61] as a biomaterial and excellent chromatography support,[62] because of its biocompatibility and mechanical properties, and as oxygen sensor,[63,64] thanks to the mobility of oxygen in bulk and surfaces.

In catalysis, zirconia is extensively used as a robust support and active component in several processes, because of its structure, redox and acid-base properties. It is used as a support for Au catalysts in the water gas shift reaction (WGS),[65] and in the steam reformation of methanol for the production of H_2.[66,67] It catalyzes the heterolytic splitting of H_2, which enables the use in hydrogenation reactions of CO and CO_2, a key step in the synthesis of organic molecules like methanol and olefins,[68,69] and in the hydrogenation of dienes.[70] It has been shown to be more effective in ketonization of carboxylic acids in biomass conversion than other widely used oxides like CeO_2, SiO_2 or Al_2O_3. Also, it is used as a support for Au, Ag and Cu metal particles for the oxidation of CO to CO_2.[33,71,72,73] Finally, zirconia nanoparticles are potential catalysts for the photocatalytic decomposition of pure water under UV light[74] and the photoreduction of CO_2.[74,75]

In another context, zirconia is also largely employed in Solid Oxide Fuel Cells (SOFC). Fuel cells are devices that electrochemically convert the chemical energy of a fuel gas (CO, hydrocarbons, biofuels and alcohols) into electrical energy, without the combustion of chemical species.[76] Among the different fuel cells, SOFCs show the highest electrical efficiency, by performing the electrochemical oxidation of H_2 ($H_2 + O^{2-} \rightarrow H_2O + e^-$).

Operated in the reverse mode, they are used to store energy (Solid Oxide Electrolysis Cells, SOEC).[77] Zirconia is used in SOFCs in the form of Yttrium-Stabilized Zirconia as anode with Ni nanoparticles as cathode, because of its stability over a wide range of partial pressure of oxygen, the mechanical strength and its low cost.[78] In the oxide part (anode), H_2 or fuels are oxidized by O^{2-} ions ($H_2+O^{2-} \rightarrow H_2O + 2e^-$); in the metal particles (cathode), the released electrons reduce gas O_2 to O^{2-}, reoxidizing the system. Thus, the performance of SOFC devices depends on the anode structure and the capacity of O^{2-} ions to diffuse and react,[79] which brings the necessity to understand how the oxides work in a microscopic scale.

3 Nanostructuring Oxides

3.1 Oxide Nanoparticles

It has been seen that oxides offer a broad spectrum of different functionalities and chemical activities. Recently, it has been discovered that by reducing the size of oxides down to the nanoscale regime, there appear quantum confinement effects that lead to not only the enhancement of such features but also to new and unexpected magnetic, optical, chemical, and mechanical properties that are not found in the bulk regime.[80,81,82] Nanomaterials are solids in which at least one of the three dimensions are reduced to a range of size between that of molecules and bulk systems (Figure 1.3), usually down to 1 and 100 nm, and they start to display unique and non-bulk-like properties. Nanoscaling only one dimension and leaving the other two extended in space leads to two-dimensional (2D) materials or thin films. Similarly, nanowires and nanorods are one-dimensional (1D) materials, and nanoparticles are zero-dimensional (0D) or discrete materials, in which all dimensions are nanostructured.

The special properties of oxide nanostructures come mainly from the high ratio between the number of surface and bulk atoms. In other words, with the same mass of material, nanostructuring increases the number of sites with a lower coordination than those in the bulk. These undercoordinated atoms show a higher chemical potential as their occupied electronic states –O 2p states in oxides– are destabilized with respect to the VB and those empty –cation d or f states– are stabilized with respect to the CB. In nanoparticles, these atoms are present in corners, edges, and facets, and are much more reactive than totally coordinated ones.[83,84,85,86,87] Also, nanostructures show a higher structural flexibility than bigger crystals, which allows a

better structural reorganization and therefore stabilization for example when metal particles or molecules are deposited or when an oxygen vacancy is created.

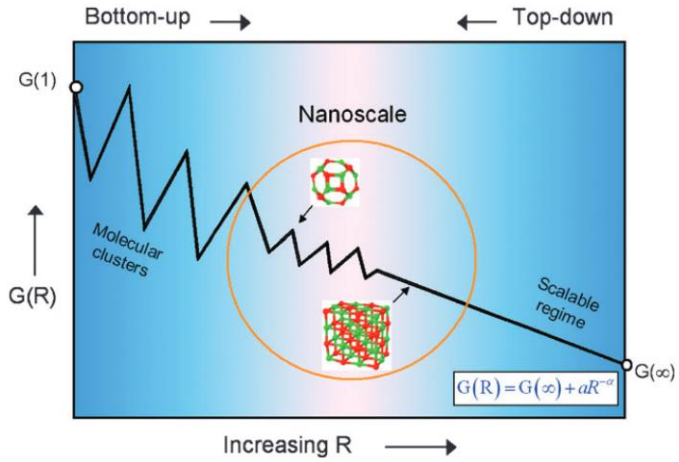

Figure 1.3 Schematic representation of an arbitrary property $G(R)$ of a solid as a function of the size R. For small sizes, the properties fluctuate sensitively with size. For larger sizes, properties enter the scalable regime until the bulk properties are recovered. From Ref. 15

Nanocrystals are attracting broad attention in emerging nanotechnologies, for instance for biological labeling and detection,[88] and in information storage media.[89,90] However, due to the high ratio of low-coordinated sites that significantly increases the reactivity, oxide nanoparticles find most applications in catalysis. This is known as nanocatalysis, where nanoparticles combine properties from both heterogeneous and homogeneous catalysis offering unique activity and selectivity.[91] For example, CeO_2 nanoparticles are used as free-radical scavengers, as in the nanoscale, the oxygen exchange and redox reactions switching between Ce^{4+} and Ce^{3+} ($2CeO_2 \rightarrow Ce_2O_3 + ½O_2$) are facilitated, enabling CeO_2 nanoparticles to regenerate the activity.[92] For instance, the energy required to release one O_{4c} from bulk CeO_2 is 4.73 eV,[93] while the release of O_{2c} from the corner of 1 – 2 nm CeO_2 nanoparticles costs around 0.8 – 1.7 eV.[94] These redox properties are exploited in biomedical applications like the protection against cellular radiation damage,[95] against oxidative stress and inflammation,[96] and for the oxidation of organic dyes without using H_2O_2.[97] Another important example are TiO_2 nanoparticles, which are of particular importance in photocatalysis. They have been extensively studied for the hydrolysis and production of H_2 under UV light,[98,99] and for their incorporation into other materials for environmental applications as a self-cleaning material.[100]

ZrO_2 nanoparticles smaller than 50 nm are found to hold a high number of oxygen vacancies, detected as surface F centers,[101,102,103] in contrast to bulk ZrO_2, which is hardly reducible. Also, the catalytic activity of ZrO_2-supported Au clusters is remarkably increased when the supporting oxide is reduced to nanoparticles in the range 5 – 100 nm.[104,105]

3.2 Supported Oxide Thin Films

Another form of nanostructured oxides treated in this thesis are oxide thin films (2D materials). These materials, once grown on a substrate, may show completely different properties from the bulk (3D) and nanoparticle (0D) counterparts. The studies of oxide films supported on metals started around 1990, most about Ti, Pd, Cr, and Fe oxide films, to obtain model systems suitable for a better characterization of oxide surfaces. Depositing few atomic layers of an oxide on a metal, it is possible to produce realistic models of oxide surfaces and with the advantage of allowing the use of characterization tools for metals and semiconductors like electron or tunneling microscopies, as the oxide is deposited on a conducting substrate.[106,107] Oxide films are also used for protection of metals by passivation,[108] in tunneling magnetoresistance sensors,[109] for gas sensing applications,[110] and in the case of ZrO_2 2D films, in solid oxide fuel cells operating at low temperatures.[76,78]

These systems introduce the topic of inverse catalysts.[111,112] There are two configurations to combine oxides and metals. One is the conventional one, in which metal nanoparticles are deposited on the oxide. This topic will be discussed in the next section. Instead, in the inverse configuration, the oxide nanostructures –thin films– are deposited on a metallic substrate. In this case, the properties of oxide films are affected by both the low-dimensionality (nanosize effects and higher fluxionality) and the presence of a dielectric boundary (interface) between the film oxide and the support in which it is grown. Sometimes, even a new phase not existing in the bulk form is formed in the 2D nanostructuring. An example of this is the lepidocrocite, a monolayer of TiO_2 with a unique crystal structure.[113,114]

Now, the film thickness is a new parameter that determines the physical properties of the oxide, as the electronic properties and structural flexibility change smoothly with the number of layers. Typically, at 10 monolayers (ML) the properties of bulk are already recovered, but such transition between thin film and bulk has no clear boundary and changes for each oxide.[115,116]

The oxide film grown on a metallic substrate exhibits new states in the energy range of its band gap. This originates from the exponential decay of the underlying metal wavefunction into the oxide, and its hybridization with the O 2p states by chemical bonding at the interface.[117,118,119] The interface states are known as Metal-Induced Gap States (MIGS), and vanish as the film thickness increases. Also, the metal-oxide film interaction is characterized by changes in the metal work function (Φ). This change is determined by the charge transfer at the metal–oxide interface and by the oxide-induced polarization of the electrons in the metal surface. This is sketched in Figure 1.4. The charge transfer to (from) the oxide creates a positive (negative) image charge on the metal surface. The created surface dipole hinders (favors) the pass of the emitted electron increasing (decreasing) thus Φ. This factor is dominant in thin films with an important covalent character like TiO_2 and SiO_2.[120,121,122] Instead, highly ionic oxides like MgO, in which the charge transfer at the metal–oxide interface is small,[123,124] compress by Pauli repulsion the electron density of the metal surface back into the bulk, lowering the surface dipole and thus Φ.[123,125,126]

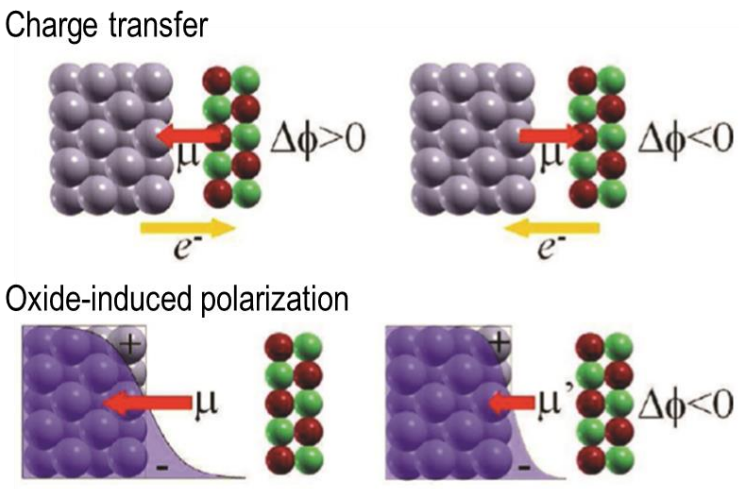

Figure 1.4 Schematic representation of the two major contributions to the change in work function induced by the growth of a thin film oxide: (top) charge transfer at the interface, and (bottom) oxide-induced polarization of the metal surface electron density. From Ref. 18

This is an important phenomenon to take into account when metal particles or molecules are adsorbed on supported thin films, as the changes in the surface work function may determine the chemical reactivity toward adsorbates. For example, Au atoms were found

experimentally[127] and by DFT calculations[119,126,127] to be negatively charged when deposited on nondefective MgO/Mo and MgO/Ag thin films by electron transfer from the substrate to Au through the dielectric barrier. Au_{20} clusters adopted a tetrahedral shape (3D) on bulk MgO, while on a MgO/Mo thin film of 4 – 5 ML an enhanced bonding of 2D clusters was found from an electrostatic interaction between the substrate and the charge transferred to the cluster.[128] O_2 molecules were also reduced to superoxo ions O_2^- when adsorbed on MgO/Mo thin films by charge transfer from Mo.[129,130] The charge transfer can be explained by the separation between the HOMO or LUMO levels of the deposited species and the Fermi level of the underlying metal. This separation creates a potential difference that induces a spontaneous charge transfer by electron tunneling through the dielectric barrier (oxide film), since the film thickness is still below the mean free path of electrons.[131]

The chemistry of thin films may not be limited to support clusters and molecules. If the interaction between the film oxide and the underlying metal is weak, and the oxide structure contains pores big enough, small molecules could intercalate and adsorb at the interface sites between the two systems. For example, CO and D2 molecules can diffuse through a SiO_2 bilayer and adsorb on the supporting Ru surface.[132] Even an entire chemical reaction can take place in those sites, as demonstrated by Mu et al. for the CO oxidation reaction at the interface between a graphene and supporting Pt.[133]

4 Creating a Metal-Oxide Interface: Deposition of Metal Clusters on Oxides

The presence of a metal-oxide interface is of fundamental importance in several modern technologies. For example, they are applied in microelectronic devices to create Schottky contacts and metal-oxide resistive random-access memories, in electrochemistry for contact electrodes, as oxide films to protect against oxidation the underlying metal (passivation), in catalysis, etc. However, the study of interfaces is not easy. They are difficult to access experimentally with the typical techniques used in surface science. Interfaces are difficult to describe also theoretically, as it involves two materials with different properties. For example, DFT methods that describe correctly one class of material, like standard GGA functionals for metals, usually perform poorly for the insulating phase of the system. On the contrary, self-interaction corrected functionals describe well semiconductors but fail in the description of metals.[19]

4.1 Metal Clusters

Clusters are aggregates of atoms forming particles of a few nanometers whose properties change with the addition or subtraction of a single atom. Their properties may be completely different from those observed in the bulk counterpart of the constituent elements, mainly due to the high surface-to-bulk atoms and quantum confinement. Similar to nanostructured oxides (section §1.3), the undercoordination of the atoms in clusters leads to high-lying d states which are much more reactive toward adsorbates (higher chemical potential). So, they exhibit an unusual catalytic activity[134,135] and a higher oxidation resistance.[136] Also, metal clusters find important applications in biomedicine due to the ability to provide selective biomolecular binding.[137,138]

It is important to distinguish between clusters and nanoparticles. Atoms in clusters cannot form any primitive unit cell that is replicated more than once in the structure. They exhibit a molecular-like nature. In a nanoparticle, a periodicity can be observed in the bulk part, that is, a unit cell is formed and replicated more than once, and the periodicity is truncated in the surfaces of the nanoparticle. However, this does not establish the boundary at which the bulklike properties are recovered. The size at which quantum confinement is negligible and the properties are converged to those of bulk is never clear and changes for each material and morphology. For example, F. Illas et al. reported from DFT calculations that the optical and electronic properties of anatase TiO_2 nanoparticles are in a nonscalable and non-bulklike regime up to around 15000 TiO_2 units (20 nm). Bigger sizes can already be considered bulk.[139]

The selectivity and activity of the clusters can be sensitively altered via small changes in size and composition, as every atom can have a substantial influence in the stability and catalytic activity.[146,140] This provides a wide range of possibilities to tune the catalytic properties with small changes. Already in 1981, it was demonstrated that certain clusters with a ‘magic’ number of atoms were especially stable. For example, K. Sattler found that the most stable Xe clusters were those with 13, 55, 147, etc atoms, the number of atoms to generate perfect icosahedrons.[138] W. Knight found that the highest stabilities for alkali metal clusters were obtained with aggregates of 2, 8, 20, etc atoms, corresponding to the number of electrons needed to fill successive shells of electrons, like in a single atom.[141] The same occurs for

deposited clusters. A thin film made of C_{900} clusters behaves like graphite, while that made of C_{20} behaves like diamond.[142]

4.1.1 Supported Clusters in Heterogeneous Catalysis

Deposition of transition metal particles with nano- and subnanometer size on various oxides is a topic of enormous interest for the investigation of the mechanisms of diffusion, nucleation and growth, and stabilization.[13,143] One of the widest applications of supported metal clusters is in the field of heterogeneous catalysis. The growth and characterization of subnanometer clusters on oxides is at the basis of nanocatalysis.[144,145]

A gas phase cluster has a large number of possible configurations, but the situation can be more complex when it is deposited on a supporting oxide. The description of a metal cluster deposited on a support is complicated by the existence of multiple isomers, spin configurations and fluxionality. The different local minima are often separated by small energy differences that facilitate the interconversion between one isomer into another. Then, at finite temperatures metal clusters change continuously shape and structure over the surface. Moreover, any structural disorder can modify the chemical properties.[146]

Metal nanoparticles can be prepared and deposited on oxides via various methods. For example, the metal or metals of interest are evaporated by laser pulses, electrical or magnetron discharges, or by collision of highly energetic gas ions. The metal atoms evaporated aggregate in the gas phase forming clusters that can then be deposited after mass-selection if needed.[147] Other methods can be chemical vapor deposition,[148] colloidal techniques,[149] deposition-precipitation,[150] and impregnation.[151] Once deposited, information about the particle size distribution on the support is obtained via techniques like scanning tunneling microscopy (STM), atomic force microscopy (AFM), transmission electron microscopy (TEM), and optical spectroscopies in the visible or infrared.

A part from the great and tunable catalytic activity and selectivity, supported clusters have become of fundamental use in catalysis also due to economic factors, and an accentuated metal-support interaction. Using small and active clusters supposes the reduction of the amount of precious metals needed for a catalytic reaction. For instance, core-shell clusters can be synthesized in which the inactive core is a much cheaper metal. Also, clusters of different metals, by synergic effects, may exhibit an enhanced activity compared to that of pure clusters.

Also, the role of the support is more accentuated in deposited nanoclusters than in bigger nanoparticles. In general, the precise control of all these factor leads not only to a better understanding of the catalytic processes at the atomic scale but to the development of novel and highly efficient catalysts.

Metal Support Interaction

The support plays a key role in the catalytic activity of the deposited metal clusters. It has been assumed for a long time that supports provide only an inert basis for metal particles. However, the more refined techniques that permitted the deposition and growth of 1 nm clusters and below made clear that, in that scale, the support is no longer inert as it induces non-negligible changes in the properties of the clusters.

The extent of the metal-support interaction depends on the composition and structure of the metal,[152] and the type of the support.[153,154] For instance, Au nanoparticles are found to be spherical deposited on TiO_2 and flat or two-dimensional on ZrO_2.[155] The catalytic activity of the deposited metal can be affected by several ways. (1) The support can modify the stability of the metal particle, and its morphology. For example, Comotti et al. deposited Au particles of the same size on TiO_2, ZrO_2, ZnO, and Al_2O_3. The different catalytic activities observed in the CO oxidation reaction suggested that the supports led to changes in the shape of the Au particles modifying thus the activities.[73] (2) The support can induce strain due to lattice mismatch.[156] The strain causes an expansion in the metal-metal bond distance, which narrows the metal d band and shifts it toward the Fermi level. This causes a higher reactivity of the metal toward reactants.[157,158] (3) Supports can also enable spillover of species from the support surface or vice versa,[159,160,161] or (4) change the electronic structure of the metal particles via charge transfer processes at the metal-oxide interface.[18,162,163] The last can at the same time modify the morphology, which is in turn another factor that affects the activity.[164,165]

The occurrence and extent of electron transfer at the metal-oxide interface depend on several factors related to both the metal particle and oxide natures. On nonreducible oxides like MgO or SiO_2, the bonding with the metal particle is dominated by polarization effects, and the charge transfer is strongly dependent on the level of defectivity of the surface. That is, stoichiometric and nonreducible oxides do not exhibit empty (occupied) electronic states with sufficient low (high) energy with respect to those occupied (empty) states of the deposited

particles in order to experiment a charge transfer. Reducible oxides like TiO_2 or CeO_2 can have empty electronic states at lower energy levels such that metals with low ionization potential can be oxidized by simply deposition on these oxides even in a stoichiometric composition.

However, charge transfer phenomena are modified when intrinsic defects, like oxygen vacancies or grain boundaries, or extrinsic defects, like dopants, are present in the oxide. It is possible to identify two main groups of defect levels: (1) new acceptor states, empty or partially occupied, above the oxide VB, for example upon p-type doping. These can trap the electronic charge of the deposited particles (oxidation). (2) Defects, like O vacancies and n-type dopants, can introduce donor levels sufficiently high in energy to be above the acceptor levels of the deposited particles, resulting in their reduction. In general, charge can flow from the surface to the particles and vice versa, resulting in modification of the catalytic properties. However, this are complex processes that are not always easy to predict. This important topic will be treated in chapter §5.2.

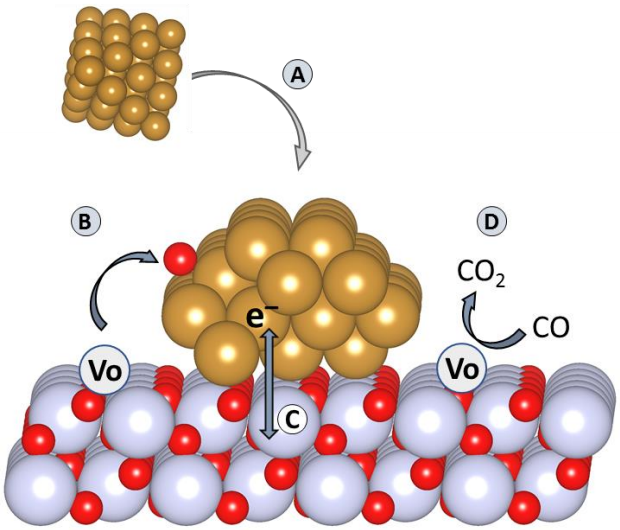

Figure 1.5 Schematic representation of the processes described in text driven by the metal-oxide interaction. A: morphology change. B: oxygen reverse spillover. C: charge transfer. D: perimeter activation.

Not only oxides can modify the properties of the deposited metal particles, but also, some oxide properties change at the metal-oxide interface. Atoms at the perimeter sites may have an altered electronic structure, so a different reactivity compared to that of sites at the clean

oxide surface (perimeter activation). A very important phenomenon is that deposited particles can catalyze the reduction of the oxide. In particular, in the periphery between the metal particle and the oxide are regions where oxygen is easier to remove. For example, only the presence of single Pt atoms greatly improves the surface reducibility of Fe_2O_3,[166] or the presence of Au particles on SiO_2 resulted in surface holes due to the desorption of volatile SiO from the Au perimeter sites.[167] This will have important consequences in catalysts by activating reactions where the transfer of oxygen is involved. It will be seen in chapter §5.3 in the CO oxidation reaction on a Au/ZrO_2 catalyst.

The easy formation of oxygen vacancies at the boundaries of the metal particle is related to another important phenomenon, the oxygen reverse spillover. In this process, oxygen atoms diffuse to the supported metal particle that can be covered by a more or less thick oxide layer. Two different situations can be distinguished. The oxygen spilled over the metal can be oxygen species adsorbed from the gas phase on the surface, or oxygen atoms of the lattice. The second case is related to the enhanced reducibility of the oxide at the interface, as this implies the formation of surface oxygen vacancies. It can be seen as a first step of the so-called strong metal-support interaction (SMSI), in which an oxide layer grows over the metal particle and, in some cases, can be completely encapsulated and lose its chemical properties.

The spillover of the lattice oxygen to the metal plays a key role in some reaction mechanisms. For example, the remarkable oxygen storage capacity (OSC) of CeO_2-based catalysts, which allows to supply lattice oxygen in an excess of reductants and be reoxidized in an excess of oxidants, is facilitated by the presence of metal particles that adsorb such lattice oxygen.[92] Also, the oxygen reverse spillover provides a self-cleaning behavior to Pt/CeO_2 catalysts after their poisoning with carbon deposits. It has been suggested that spilled over oxygen from the lattice oxidizes carbon to CO and CO_2 that are then desorbed.[168]

Chapter 2

Theoretical Methods

In this chapter, some theoretical concepts necessary to understand and discuss conveniently the results of this thesis are introduced. This does not aim entering deep in the theory but at least a general reminding of parts of the theory that may support the comprehension of the results.

1 The Schrödinger Equation

Quantum chemistry is based on applying quantum mechanics in chemical systems. In quantum mechanics, the state of a system is represented by a wavefunction, $|\Psi\rangle$. The evolution of the state with time follows the time dependent Schrödinger equation (1).[169]

$$i\hbar \frac{d\Psi(\boldsymbol{r},t)}{dt} = \hat{H}(\boldsymbol{r},t)|\Psi(\boldsymbol{r},t)\rangle \quad (1)$$

$\hat{H}$ is the Hamiltonian operator corresponding to the total energy of the system, including any applied external fields. One can then separate time- and space-dependence of Eq. (1) to obtain the time independent Schrödinger equation

$$\hat{H}|\Psi\rangle = E|\Psi\rangle \quad (2)$$

where E is the numerical value of the energy relative to the state where all electrons and nuclei are infinitely separated.

The Hamiltonian operator of a molecular system includes terms such as the kinetic energy of the electrons, $\hat{T}_e$, the kinetic energy of the nuclei, $\hat{T}_N$, potential energy from electron-electron repulsion, $\hat{V}_{ee}$, nuclei-nuclei repulsion, $\hat{V}_{NN}$, and the electron-nuclei attraction, $\hat{V}_{Ne}$. So, a non-relativistic form of the Hamiltonian for a system with no external fields is given by,

$$\hat{H} = \hat{T}_e + \hat{T}_N + \hat{V}_{ee} + \hat{V}_{NN} + \hat{V}_{Ne} = \quad (3)$$
$$-\sum_{i=1}^{N_e} \frac{\hbar^2}{2m_e} \nabla_i^2 - \sum_{I=1}^{N_N} \frac{\hbar^2}{2M_I} \nabla_I^2 + \sum_{i=1}^{N_e-1} \sum_{j>i}^{N_e} \frac{e^2}{4\pi\varepsilon_0 r_{ij}} + \sum_{I=1}^{N_N-1} \sum_{J>I}^{N_N} \frac{Z_I Z_J e^2}{4\pi\varepsilon_0 R_{IJ}} + \sum_{i=1}^{N_e} \sum_{J=1}^{N_N} \frac{Z_J e^2}{4\pi\varepsilon_0 R_{iJ}}$$

where lower case indices are used for electrons and upper case for nuclei. N_e is the total number of electrons and N_N is the number of nuclei. Z denote nucleic charges and m, M, are the mass of electron and nucleus, respectively. For any system with more than two particles, derived Schrödinger equation is almost impossible to solve analytically. Perhaps, the most indispensable approximation in quantum mechanics was proposed in 1927 by Born and Oppenheimer (BO),[170] in which the movement of nucleus is separated from that of electrons since the mass of the nucleus is much greater (a proton is 1837 times heavier than an electron). The wave function can then be written as,

$$\Psi(\boldsymbol{r}, \boldsymbol{R}) = E_e \Psi_e(\boldsymbol{r}; \boldsymbol{R}) \Phi_N(\boldsymbol{R}) \quad (4)$$

and the electronic Schrödinger equation becomes

$$T_e \Psi_e + V_{ee} \Psi_e = E_e(\boldsymbol{R}) \Psi_e \quad (5)$$

Once solved the Schrödinger equation, and then the total equation

$$T_N \Phi_\mathrm{N} + E_e \Phi_\mathrm{N} = E \Phi_\mathrm{N} \quad (6)$$

many different nuclear geometries will result in a potential energy surface (PES) for a polyatomic molecule.

Although the BO approximation has simplified the problem of molecular calculations considerably, solving the electronic Schrödinger equation is still nontrivial. The approaches to solving the electronic Schrödinger equation are divided into two main branches, *ab initio* (or first principles) and semi-empirical methods. Semi-empirical methods use a simplified Hamiltonian and adjustable parameters obtained from experiments. In *ab initio* methods, a model wavefunction is chosen and the Schrödinger equation is solved using this wave function as the only input. The accuracy of the result depends on the quality of the wavefunction chosen.

2 The Electronic Structure Problem: Computational Methods

The electronic Hamiltonian for a polyelectronic system can be expressed as,

$$\hat{\mathrm{H}}_\mathrm{e} = \sum_{\mathrm{i}=1}^{\mathrm{N_e}} \hat{\mathrm{h}}(\mathbf{r}_\mathrm{i}) + \sum_{\mathrm{i}}^{\mathrm{N_e}} \sum_{\mathrm{i>j}}^{\mathrm{N_e}} \frac{1}{\mathbf{r}_{\mathrm{ij}}} \quad (7)$$

where the first term accounts for the monoelectronic contribution and the second term for bielectronic interaction. The presence of bielectronic terms does not allow to express the solution of Schrödinger equation as a single Slater determinant. Thus, the polyelectronic function can be expressed as,

$$\Psi(\mathbf{w}_1, \mathbf{w}_2, \dots, \mathbf{w}_{N_e}) = \frac{1}{\sqrt{N_e!}} \sum_{i,j,\dots,k} C_{i,j,\dots,k} \psi_{i,j,\dots,k} =$$

$$\frac{1}{\sqrt{N_e!}} \sum_{i,j,\dots,k} C_{i,j,\dots,k} \left| \psi_i(\mathbf{w}_1) \psi_j(\mathbf{w}_2) \dots \psi_k(\mathbf{w}_{N_e}) \right| \quad (8)$$

The simplest approximation to the solution of a polyelectronic system is to use a function formed by just a single Slater determinant (monoconfigurational):

$$\Psi(\boldsymbol{w}_1, \boldsymbol{w}_2, \dots, \boldsymbol{w}_{N_e}) \approx \frac{1}{\sqrt{N_e!}} \left| \psi_i(\boldsymbol{w}_1) \psi_j(\boldsymbol{w}_2) \dots \psi_k(\boldsymbol{w}_{N_e}) \right| \quad (9)$$

The Hartree-Fock (HF) method finds the best orbitals using the variational method. Slater determinants do not include the electron correlation. In the HF method, each electron is considered to be moving in an average potential field created by the nuclei and the other N_e – 1 electrons. For a system of N_e electrons we thus have a system of N_e equations that depend on each other, so the problem has to be solved iteratively, i.e. in a self-consistent field (HF-SCF).

The HF method is adopted as the basis of many more advanced computational methods, and it is used to define the electron correlation energy. This is defined as the difference between the exact non-relativistic energy and the HF energy of the system,

$$E_{corr} = E_{exact} - E_{HF} \quad (10)$$

Within the BO approximation, the only error in the HF energy is the correlation energy, and the goal of most post-HF methods is to recover as much of the this term as possible.

We can distinguish between dynamical and non-dynamical electronic correlation. The non-dynamical correlation can be included in the calculation of the Schrödinger equation by the use of multiconfigurational wavefunctions, like Multiconfigurational Self-Consistent Field Method (MCSCF). The dynamical correlation can be obtained by means of perturbative, like the Møller-Plesset perturbation theory,[171] and variational methods, like the Configuration Interaction Method (CI).[172]

3 Density Functional Theory

The high computational cost of the *ab initio* methods described above, has motivated the search for alternative methods. One branch is density functional theory (DFT). Instead of focusing on state functions, DFT focuses on the electron probability density, $\rho(\mathbf{r})$. The basic idea in DFT is that the energy of the electronic ground state of a polyelectronic system only depends on its electron density, $\rho(\mathbf{r})$, formally proved by the Hohenberg-Kohn theorem.[173] Thus, it is not necessary to know the wavefunction that describes the chemical system. Since the electron density only depends on its three space coordinates, DFT is a notably less exigent method (wavefunction methods depend on the three space coordinates of each electron, that is, 3N variables).

The function of the electron density is the probability of finding an electron in a volume $d\boldsymbol{r}$ with arbitrary spin, and it has to fulfill the following conditions

$$\rho(\boldsymbol{r}) = N_e \int \dots \int \left|\varphi(r_1, \dots, r_{N_e})\right|^2 dr_1, \dots, dr_{N_e} \tag{11}$$

$$\int \rho(\boldsymbol{r}) d\boldsymbol{r} = N_e \qquad \rho(r \to \infty) = 0 \tag{12}$$

3.1 Hohenberg and Kohn Theorems

The first theorem of Hohenberg and Kohn says that the electron density of the ground state cannot be derived from two different external potentials, V_{ext} (the potential from the external charged nucleus), except if they differ by a constant. This proves that any observable of a stationary and non-degenerate ground state is uniquely determined by $\rho_0(\mathbf{r})$ and can be written as a functional of the electron density, Eq. (13). It stablishes that the electron density is determined by the external potential and the inverse relation (V-representability).

$$E_0 = E_0[\rho(\boldsymbol{r})] \tag{13}$$

The second theorem, the variational principle theorem, stablishes that the energy of the ground state can be variationally obtained, and the electron density minimizing the total energy is the exact electron density of the non-degenerate ground state. Then, it defines the correct external potential.

$$E_0 \leq E[\rho(\boldsymbol{r})] \tag{14}$$

The functional of the electron density can be divided into a part corresponding to the interaction between the electron density and the external potential, and a second contribution

$F[\rho]$, Eq. (15), which is a universal functional that depends on the electrons, including their kinetic energy $T[\rho]$ and the Coulombic repulsion between them $V_{ee}[\rho]$.

$$E[\rho] = \int \rho(\boldsymbol{r}) V_{ext} d\boldsymbol{r} + F[\rho] \qquad F[\rho] \equiv T[\rho] + V_{ee}[\rho] \tag{15}$$

3.2 The Kohn-Sham Method

According to Kohn and Sham, the electron density of a polyelectronic system (with N_e electrons) can be represented by non-interacting electrons with the same density as in the real system, and it is expressed by the sum of squares of N monoelectronic spinorbitals, the Kohn-Sham orbitals, ϕ_i.[174]

$$\rho(\boldsymbol{r}) = \rho_{KS}(\boldsymbol{r}) = \sum_i^N |\phi_i(\boldsymbol{r})|^2 \tag{16}$$

The kinetic energy of the non-interacting system is expressed as,

$$T_s[\rho] = \sum_i^N \left\langle \phi_i \left| -\frac{1}{2}\nabla^2 \right| \phi_i \right\rangle \tag{17}$$

The total energy of the fictitious system can be expressed as a functional of the non-interacting electron density, and can be obtained by minimizing,

$$E[\rho] = T_s[\rho] + \int \rho(\boldsymbol{r}) V_{ext}(\boldsymbol{r}) dr + \frac{1}{2}\int \frac{[\rho(\boldsymbol{r})\rho(\boldsymbol{r}')]}{|\boldsymbol{r}-\boldsymbol{r}'|} d\boldsymbol{r} d\boldsymbol{r}' + E_{XC}[\rho] \tag{18}$$

$$E = T_s + E_{ext} + J + E_{XC} \tag{19}$$

whose terms are the kinetic energy of electrons, T_S, the attraction between the external potential and the density, E_{ext}, the Coulombic repulsion between electrons, J, and the difference between the kinetic energy of the non-interacting and the real systems, as well as the exchange and correlation energies

$$E_{XC}[\rho] \equiv T[\rho] - T_s[\rho] + V_{ee}[\rho] - J[\rho] \tag{20}$$

The set of states that minimize the KS functional is found solving in a self-consistent mode the Kohn-Sham equations

$$\left(-\frac{1}{2}\nabla^2 + V_{eff}(\boldsymbol{r})\right)\phi_i(\boldsymbol{r}) = \varepsilon_i \phi_i(\boldsymbol{r})$$

$$V_{eff}(\boldsymbol{r}) = V_{ext}(\boldsymbol{r}) + \int \frac{\rho(\boldsymbol{r}')}{|\boldsymbol{r}-\boldsymbol{r}'|} d\boldsymbol{r}' + V_{XC}(\boldsymbol{r}) \tag{21}$$

The exchange and correlation potential can be obtained by means of the derivative of the exchange and correlation functional with respect to the density

$$V_{XC}(\boldsymbol{r}) = \frac{dE_{XC}[\rho]}{\rho(\boldsymbol{r})} \quad (22)$$

It is worth noting that the KS equations are equivalent to the Hartree-Fock equations but here the correlation is included. However, this exchange and correlation functional is not known. If the functional were known exactly, the DFT methods would yield the exact solution of the real system, which is of course not yet achieved.

3.3 Exchange and Correlation Functionals

The development of new and better exchange and correlation functionals is one of the most important research fields in computational chemistry and physics. The strategy that is usually followed is the so-called Jacob's ladder, which is a five steps ladder corresponding to the levels of quality of the functionals being the last the universal and divine one that yields the exact solution for all systems.

The first and simplest functional to describe the exchange and correlation energy is the one based in the Local Density Approximation (LDA). For an open shell system, the same formalism can be applied considering two electron densities, one for each spin state (LSDA approach). It is based on the supposition that the electron density does not change with the position. The density is then equivalent to that of the uniform electron gas, for which the exact exchange and correlation functional is known. Thus, this functional can be separated into two terms: exchange and correlation, Eq. (27). The first is directly derived from the electron gas model, and for the correlation part the most used approach is that of Vosko, Wilk and Nussair[175]

$$E_{XC}[\rho] = \int \rho(\boldsymbol{r})\varepsilon_{XC}[\rho]d\boldsymbol{r} = \int \rho(\boldsymbol{r})\varepsilon_{X}[\rho]d\boldsymbol{r} + \int \rho(\boldsymbol{r})\varepsilon_{C}[\rho]d\boldsymbol{r} \quad (23)$$

$$E_{XC}^{LDA}[\rho] = E_X[\rho] + E_C[\rho]$$

$$E_X[\rho] = -\frac{3}{4}\left(\frac{3}{\pi}\right)^{\frac{1}{3}}\rho(\boldsymbol{r})^{\frac{1}{3}} \quad (24)$$

This functional can yield good results for metals, since the behavior of electrons in metals is similar to the uniform electron gas. On the other hand, the bonds are overestimated and it fails in the description of strongly correlated systems like magnetic oxides.

Other functionals for the exchange and correlation part are based in the Generalized Gradient Approximation (GGA). These potentials consider that the functional depends on the

density in each point of the space and on the gradient of the density in such points (semilocal approximation)

$$E_{XC}^{GGA}[\rho] = \int f(\rho(\boldsymbol{r}), \nabla\rho(\boldsymbol{r}))d\boldsymbol{r} \quad (25)$$

This type of functionals can also be separated into exchange and correlation, and it is possible to do combinations of different parts. The functional employed in the calculations through all this work is the Perdew Becke Ernzerhof functional (PBE),[176] Eq. (26). This is a modified version of the previous Perdew Wang (PW91) functional,[177] which is shown to give better results with lower number of parameters, which reduces the computational cost.

$$E_X[\rho] = \int \rho(\boldsymbol{r})\varepsilon_X(\boldsymbol{r})d\boldsymbol{r} = \int \rho(\boldsymbol{r})\varepsilon_X^{LDA}(\boldsymbol{r})F_X\big(s(\boldsymbol{r})\big)d\boldsymbol{r} \quad (26)$$

$$F_X(s) = 1 + k - \frac{k}{1+\frac{\mu s^2}{k}}$$

$$s(\boldsymbol{r}) = \frac{|\nabla\rho(\boldsymbol{r})|}{2(3\pi^2)^{\frac{1}{3}}\rho(\boldsymbol{r})^{\frac{4}{3}}}$$

3.4 Hybrid Density Functionals

Hybrid density functionals are probably the most used functionals. These are a linear combination of the exchange and correlation contributions of known functionals as LDA and GGA with a part based on the wavefunction, like the HF exchange. These complex functionals are parametrized with thermodynamic data of molecules. The fraction of the Fock exchange is connected to the dielectric constant of the material.[178] For instance, the optimum fraction of Fock exchange for bulk ZrO_2 is 20.8% as this value provides quantitative agreement with experiments.[179,180] However, there are standard functionals with a fixed amount of Fock exchange. The most used is the B3LYP, created by Becke, with a 20% of Fock contribution[181,182]

$$E_{XC}^{B3LYP} = \beta E_X^{HF}[\{\psi_i\}] + (1-\beta)E_X^{LDA}[\rho] + a\Delta E_X^{B88}[\rho] + E_C^{VWN}[\rho] + c\Delta E_C^{LYP}[\rho] \quad (27)$$

and the PBE0 functional, which is the addition of a 25% of Fock exchange to the PBE density functional.

It is important to note that all functionals lack some property or quality, like for instance the subestimation of the band gap in semiconductors, or the electronic localization. The universal exchange-correlation functional giving an equally accurate description of all observables is still to be developed. This problem is due to the self-interaction error present in

DFT, which comes from the interelectronic term in the formulation that does not exclude the interaction of one electron with itself. This fact can be partly attenuated with semiempirical corrections like the DFT+U approach, with the correcting Hubbard U parameter.[183,184]

3.5 The Hubbard U Correction

In classical approximate density functionals, the electronic self-interaction is not completely cancelled in the Coulomb integrals. They do not properly account for the exchange interaction and tend to over-delocalize valence electrons and stabilize metallic ground states. Thus, insulating and semiconductor materials are not well represented with standard DFT functionals.

To represent the insulating character, a strong Coulomb repulsion between electrons must prevail over their kinetic energy that tends to delocalize them, such that they are forced to be localized on atomic-like orbitals (Mott insulators). Then, band theory also fails at capturing the physics of these materials. The motion of localized electrons is strongly correlated, meaning that a multi-determinant wavefunction is needed and the full account for the many-body terms of the electronic interactions. This is not trivial in DFT since the electrons interaction is expressed as a functional of the electron density and an effective single particle Kohn-Sham basis is used to represent the density.

A good and simple approximation to partly solve this failure is the Hubbard model. It uses a real-space second quantization formalism to better represent the localization of electrons on atomic orbitals. This model defines the Hubbard Hamiltonian as the sum of two terms

$$H_{Hub} = t \sum_{\langle i,j \rangle,\sigma} \left(c_{i,\sigma}^{\dagger} c_{j,\sigma} + h.c. \right) + U \sum_i n_{i,\uparrow} n_{i,\downarrow} \qquad (28)$$

The first is a single-particle term that describes the movement (hopping) of the electrons between different sites, i.e. electron delocalization. The amplitude of the first term, *t*, is proportional to the dispersion or bandwidth of the valence states, as the extension of the bands over a large energy interval (highly dispersed) comes from strong orbital overlaps, which promotes the electron delocalization. The second term accounts for the short-range or on-site Coulomb repulsion between electrons by means of the product of the occupation numbers, *n*, of atomic states on the same atom. The amplitude of this term is denoted by the Hubbard *U* parameter. The insulating character emerges when the Coulomb repulsion between electrons in the same atom is higher than their energy to delocalize, that is, when $U >> t$. So, the material

becomes an insulator since electrons cannot overcome the Coulomb repulsion from those in the neighboring sites.

The application of the Hubbard model on a DFT approach, denoted as DFT+U, has become one of the most widely used numerical methods to represent the effects of the static electronic correlation. It consists in the addition of a simple correction to the exchange-correlation functional. The +U approach is very easy to implement in existing DFT codes, and very importantly, does not imply very high additional computational costs. Also, the strength of the correction is easily tuned with the U parameter in order to semiempirically optimize the capture of the physics of the system.

The Hubbard Hamiltonian is applied only on the correlated electronic states (typically *d* and *f* orbitals), and the outcome energy, E_{Hub}, is added to that from the standard density functional, E_{DFT}

$$E_{DFT+U} = E_{DFT}[\rho(r)] + E_{Hub}\left[\{n^{I\sigma}_{mm'}\}\right] - E_{dc}[\{n^{I\sigma}\}] \quad (29)$$

Since the standard density functional treats both non-correlated and correlated electronic states, it is necessary to subtract from the E_{DFT} term the part of the interaction energy that is already included in the Hubbard Hamiltonian so repeated electron interactions are avoided in the calculation ($-E_{\mathrm{dc}}$).

The Hubbard term is a functional of the occupation numbers of the correlated electronic states. These are defined as projections of occupied Kohn-Sham orbitals (ψ^{σ}_{kv}) in the states of a localized basis set (ϕ^{I}_{m})

$$n^{I\sigma}_{mm'} = \sum_{k,v} f^{\sigma}_{kv} \langle \psi^{\sigma}_{kv} | \phi^{I}_{m'} \rangle \langle \phi^{I}_{m} | \psi^{\sigma}_{kv} \rangle \quad (30)$$

n is the occupation number that ranges from 0 and 1, being *n* = 1 the occupation by 2 electrons, *m* is the index of the states localized on the same atomic site *I*, f^{σ}_{kv} are the Fermi-Dirac occupations of the Kohn-Sham states, *k* and *v* the index of k-points and electronic bands, respectively, and σ the spin state. With this definition of the occupation numbers, the Hubbard potential acting on the Kohn-Sham wavefunction that is correcting the total electronic Hamiltonian can be written as

$$V|\psi^{\sigma}_{k,v}\rangle = V_{LDA}\left|\psi^{\sigma}_{k,v}\right\rangle + \sum_{I,m} U^{I}\left(\frac{1}{2} - n^{I\sigma}_{m}\right)\left|\phi^{l}_{m}\right\rangle\left\langle\phi^{l}_{m}\middle|\psi^{\sigma}_{k,v}\right\rangle \quad (31)$$

which leads to the density functional

$$E = E_{DFT} + \sum_I \left[\frac{U^I}{2}\sum_{m,\sigma\neq m',\sigma'} n_m^{I\sigma} n_{m'}^{I\sigma'} - \frac{U^I}{2} n^I(n^I - 1)\right] \quad (32)$$

The Hubbard potential is repulsive for half-occupied orbitals ($n_m^{I\sigma} < ½$), while it is attractive for the rest. This means that this correction to the Hamiltonian penalizes the partial occupation of localized orbitals, which come from the hybridization of neighboring orbitals and delocalization among them. Then, the Mott localization is instead promoted ($n_m^{I\sigma} \rightarrow 1$).

In addition, the higher electron localization emerged from the on-site Coulomb repulsion leads to the lifting of degenerate states around the Fermi level so to the opening of a band gap in the Kohn-Sham eigenvalues. In fact, the calculation can lower the symmetry of the system so that it converges to one of the possible degenerate insulating states separated by a finite gap. This leads to a better representation of the electronic structure of a wide range of solid materials whose band gap is usually under-estimated with standard DFT functionals.

4 Dispersion Forces

The GGA type exchange-correlation density functionals do not include the long-range dispersion forces. As it will be demonstrated in section §3.2.1, dispersion forces may be important for the description of the adsorption processes of clusters and molecules, and the creation of interfaces. To account for them, the semi-empirical pairwise forcefield implemented by Grimme, named as DFT+D2, was considered in the calculations when needed.[185] This method consist in the addition of an extra term to the DFT energy

$$E_{DFT+D2} = E_{DFT} + E_{disp} \quad (33)$$

$$E_{disp} = -s_6 \sum_{i=1}^{N-1}\sum_{j=i+1}^{N} \frac{C_6^{ij}}{R_{ij}^6} \frac{1}{1+e^{-d\left(\frac{R_{ij}}{R_r}-1\right)}} \quad (34)$$

where s_6 is a global scaling factor that depends only on the DFT functional employed, C_6^{ij} is a coefficient for the *ij* pair, R_{ij} is the interatomic distance between *i* and *j* atoms, R_r is the sum of the van der Waals radii of *i* and *j* atoms, and *d* is a constant set to 20. The C_6^{ij} coefficients are defined as the geometric mean of the atomic C_6 coefficients, $C_6^{ij}=(C_6^i \cdot C_6^j)^{1/2}$, which are empirically determined by the ionization potential (*IP*) and polarizability (α) of each atom according to $C_6^i = 0.05 \cdot N \cdot IP^i \cdot \alpha^i$, with N = 2, 10, 18, 36, 54 for atomic elements belonging to the rows 1 – 5.

5 Periodic Systems

The representation of the solid state of matter is notably simplified due to the imposition of periodic conditions. The Schrödinger equation needs to be solved only for the atoms that form the unit cell of the model, and a translation operator, $\hat{T}_R$, replicates the wavefunction or the electron density of any point inside the unit cell to the equivalent points outside that. So, in order to optimize the computational time, the unit cell needs to be the smallest one that can describe the system correctly.

Because the atoms in crystals are arranged in a regular periodic array, the electrons are subjected to a potential, $U(\mathbf{r})$, that has the periodicity of the underlying Bravais lattice

$$U(\boldsymbol{r}+\boldsymbol{R}) = U(\boldsymbol{R}) \tag{35}$$

with $\boldsymbol{R}$ being the lattice vectors. The full Hamiltonian for solids contains the one-electron potential terms that describe the interactions of the electrons with nuclei and the pair potentials that describe the interactions between electrons. In the independent electron model, such interactions are described by a periodic and effective one-electron potential $U(\boldsymbol{r})$, equation (35). These independent electrons are the Blöch electrons, which are not like free ones but those not subjected to any potential. The periodicity of the potential leads to the formulation of the Blöch's theorem.[186]

$$\hat{H}\Psi = \left(-\frac{1}{2}\nabla^2 + U(\boldsymbol{r})\right)\Psi = \varepsilon\Psi \tag{36}$$

5.1 Blöch's Theorem

The Blöch's theorem stablishes that the eigenstates of the one-electron Hamiltonian can be chosen to have the form of a plane wave multiplying a function with the periodicity of the Bravais lattice,

$$\Psi_{n\boldsymbol{k}}(\boldsymbol{r}) = e^{i\boldsymbol{k}\cdot\boldsymbol{r}}u_{n\boldsymbol{k}}(\boldsymbol{r}) \tag{37}$$

with $u_{nk}(\boldsymbol{r}+\boldsymbol{R}) = u_{nk}(\boldsymbol{r})$. The quantum number n is the band index ($n = 1,2,3\ldots$), corresponding to independent eigenstates with different energies but with the same vector number $\boldsymbol{k}$. The function is invariable under the translation of a lattice vector $\boldsymbol{R}$

$$\hat{T}_{\boldsymbol{r}}\Psi_{n\boldsymbol{k}}(\boldsymbol{r}) = \Psi_{n\boldsymbol{k}}(\boldsymbol{r}+\boldsymbol{R}) = e^{i\boldsymbol{k}\cdot(\boldsymbol{r}+\boldsymbol{R})}u_{n\boldsymbol{k}}(\boldsymbol{r}) = e^{i\boldsymbol{k}\cdot\boldsymbol{R}}e^{i\boldsymbol{k}\cdot\boldsymbol{r}}u_{n\boldsymbol{k}}(\boldsymbol{r}) = e^{i\boldsymbol{k}\cdot\boldsymbol{R}}\Psi_{nk}(\boldsymbol{r}) \tag{38}$$

In Blöch's theorem, because of the periodic boundary conditions, the electronic Schrödinger equation in the form

$$\hat{H}_{\boldsymbol{k}} u_{\boldsymbol{k}}(\boldsymbol{r}) = \left(\frac{1}{2} \left(\frac{1}{i} \nabla + \boldsymbol{k} \right)^2 + U(\boldsymbol{r}) \right) u_{\boldsymbol{k}}(\boldsymbol{r}) = \varepsilon_{\boldsymbol{k}} u_{\boldsymbol{k}}(\boldsymbol{r}) \tag{39}$$

is restricted to a single primitive cell of the crystal. As wave vector $\boldsymbol{k}$ is a parameter in the Hamiltonian, the energy levels of electrons in a periodic potential are described in terms of a family of continuous functions $\varepsilon_n(\boldsymbol{k})$ varying with $\boldsymbol{k}$ (band structure of the solid).

In a system with N_e free electrons, the electronic ground state is constructed by occupying all one-electron levels ε_n with an energy lower than the Fermi level, ε_F. The Fermi level is determined by requiring that the total number of one-electron levels with energies below ε_F be equal to N_e. When the lowest levels are filled by a given number of electrons, it can lead to different situations. A certain number of bands can be completely filled and the rest remain empty, or instead the highest occupied bands remain partially filled. In the first case, the energy difference between the highest occupied level and the lowest empty is the band gap. Insulators, for instance, are materials that show a band gap that highly exceeds the thermal energy (k_bT) at room temperature, meaning that at those conditions, electrons of the valence band cannot be promoted to the conduction band. Intrinsic semiconductors, however, show a band gap that is comparable to that quantity. In the second case, for each partially occupied band, there is a surface in the $\boldsymbol{k}$ space that separates the occupied from the unoccupied levels, known as the Fermi surface. So, it is a constant energy surface in $\boldsymbol{k}$ space. In this case, solids show metallic properties provided that a Fermi surface exists.

6 Search of the Transition State. The Nudged Elastic Band

A very important problem in theoretical chemistry and solid-state physics is the search of the minimum energy path (MEP) to go from reactants to products and the potential energy maximum along this MEP. This point provides the activation energy barrier for the chemical process.

An efficient and intuitive method to calculate the MEP is the Nudged Elastic Band method (NEB).[187,188,189] In this approach, a chain of images or atomic structures of the system is generated between the initial and final energy minimums i.e. reactants and products, usually by equidistant interpolation of the atomic coordinates. All images are optimized simultaneously and in a concerted way, so parallel computers or cluster networked computers can be used very efficiently.

In the NEB method, the force acting on each image *i* is

$$\vec{F}_i = -\vec{\nabla}V(\vec{R}_i)|_\perp + \vec{F}_i^s \cdot \hat{\tau}_\parallel \hat{\tau}_\parallel \quad (40)$$

in which the first term, $-\vec{\nabla}V(\vec{R}_i)|_\perp$, represents the true potential, that is, the gradient of the potential energy surface. In this, only the component perpendicular to the images chain is considered by subtracting the parallel component, $\vec{\nabla}V(\vec{R}_i)|_\perp = \vec{\nabla}V(\vec{R}_i) - \vec{\nabla}V(\vec{R}_i)\hat{\tau}_\parallel \hat{\tau}_\parallel$. The second term is the parallel component of an elastic force defined as

$$\vec{F}_i^s = k_{i+1}(\vec{R}_{i+1} - \vec{R}_i) - k_i(\vec{R}_i - \vec{R}_{i-1}) \quad (41)$$

where *k* is analogous to an elastic constant that maintains the images together in the chain. A scheme of these forces acting on the images moving along the PES is shown in Figure 2.1. The projection of the perpendicular component of the potential and the parallel component of the spring force is called *nudging*. As the spring force does not interfere with the relaxation of the structures along the $\vec{\nabla}V$ direction (perpendicular to the path), in the end the images will satisfy $\vec{\nabla}V|_\perp = 0$, that is, they will lie in the MEP. Also, since the spring force only affects the distribution of the images within the elastic band, the choice of *k* is arbitrary.

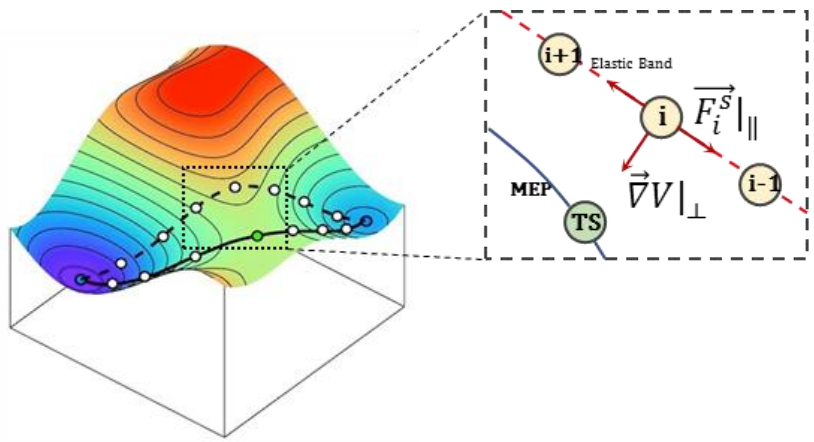

Figure 2.1. Scheme of the forces acting on each image of the elastic band in the NEB method.

When the energy of the system changes rapidly along the elastic band and the restoring force (F_i^s) is weak, the band can lose its straightness and derive in convergence problems. For example, this occurs when covalent bonds are broken and formed. To solve this, a switching function, $f(\varphi)$, that gradually introduces the perpendicular component of the spring force is introduced in the equation

$$\vec{F}_i = -\vec{\nabla}V(\vec{R}_i)|_\perp + \vec{F}_i^s \cdot \hat{\tau}_\parallel \hat{\tau}_\parallel + f(\varphi)(\vec{F}_i^s - \vec{F}_i^s \cdot \hat{\tau}_\parallel \hat{\tau}_\parallel) \quad (42)$$

If the angle φ between adjacent images becomes 90º, f(φ) = 1 and the perpendicular force is also applied. If the angle is 0, f(φ) = 0 and the perpendicular component is cancelled. Often, a small amount of this force component is enough to straighten the band and improve the convergence of the MEP optimization.

7 Computational Methodology of this Thesis

All calculations through this thesis are based on the density functional theory (DFT), in a spin-polarized or nonpolarized approach according to the needs, and were performed using the Vienna Ab Initio Simulation Package (VASP 5.2 and 5.3).[190,191] In some specific calculations and for comparative purposes, DFT calculations were also performed using the FHI-AIMS 5.2 package.[192] The computational details of these calculations will be detailed in the introduction of the corresponding section in the Results and Discussion chapter.

In VASP software, valence and core electrons are treated with a different approach. Core electrons were described by the Projector Augmented Wave (PAW) pseudopotential.[193,194] For the description of valence electrons, the Generalized Gradient Approximation (GGA) was considered for the exchange-correlation density functional, within the Perdew-Burke-Ernzerhof (PBE) formulation.[176] As explained in chapter 2, the treatment of transition metal oxides like ZrO_2 with approximated GGA density functionals suffers from the self-interaction error, which leads to an over-estimated electron delocalization leading to a wrong reduction of the band gap. This error was partly attenuated by using the PBE+U approach proposed by Dudarev et al.[184,195,196] that implements the semiempirical Hubbard U correction. In all calculations, the U = 4 eV correction was applied for the 4d states of Zr atoms. This value has been verified by other works[197] and by us to provide a good qualitative description of the electronic and geometric structures of bulk zirconia.

Planewaves were used as a basis set, up to a kinetic energy cutoff of 400 eV in all calculations and up to 600 eV in bulk calculations for reference. A total energy threshold determining self-consistency of the electron density was set to 10^{-5} eV for single and geometry optimizations, and to 10^{-6} eV for calculations of Density of States (DOS). In geometry optimizations, atoms were allowed to relax until the ionic forces were smaller than |0.01| eV/Å.

A (2x2x2) supercell of bulk of tetragonal zirconia has been optimized using an energy cutoff of 600 eV for the planewave basis set, and a *Γ*-centered Monkhorst-Pack (11x11x11) *k*-point grid to sample the Brillouin zone. The lattice parameters a_0 = 3.652 Å and c_0 = 5.214 Å were obtained, which are in good agreement with the experimental values, 3.64 and 5.27 Å.[198]

The obtained lattice parameters have been kept as reference for the construction of all zirconia models of this work. The calculated band gap was 4.6 eV. This value is still smaller than the experimental observation, 5.78 eV, (ref) attributed to the inherent error of the PBE density functional. The (101) surface of tetragonal zirconia has been modeled as a 5-layer slab with a minimum of 20 Å of vacuum. The dimensions of the supercell and the k-point grid used for each slab model will described in the corresponding section of chapter 4.

Dispersion forces have always been considered in the calculations. The DFT+D2 approach proposed by Grimme (see section §2.4) produces an overestimate of the dispersion interaction when oxides are involved. Thus, we employed a slightly modified D2 approach. As proposed by Tosoni and Sauer,[199] the C_6 and R_0 parameters of the D2 approach for the oxide cations, Zr, were replaced by those corresponding to the preceding noble gas in the periodic table (Kr), since the size of this atom is closer to that of the oxidized Zr^{4+} ion. We denote this method as DFT+D2'.

The adsorption energy of adsorbates (X = metal clusters, molecules) onto a substrate (S) has been calculated as

$$E_{ads} = E(X/S) - E(X_{(g)}) - E(S) \quad (43)$$

The formation energy of the different zirconia structures has been defined with respect to metallic Zr bulk, $Zr_{(s)}$, and molecular O_2, according to the equation

$$E_f = \frac{1}{n}E(Zr_nO_m) - E\left(Zr_{(s)}\right) - \frac{m}{2n}E(O_{2,(g)}) \quad (44)$$

where Zr_nO_m can be any morphology and stoichiometry of the oxide. $E(Zr_{(s)})$ is the energy per atom of the *hcc* unit cell of metallic Zr. $E(O_{2,(g)})$ is the energy of an O_2 molecule in the gas phase and in the $^3\Sigma_g$ electronic ground state. The formation energy of a neutral oxygen vacancy in zirconia was calculated according to

$$E_{f,Vo} = E(ZrO_{2-x}) - E(ZrO_2) + \frac{1}{2}E(O_{2,(g)}) \quad (45)$$

where ZrO_{2-x} and ZrO_2 refer to reduced and stoichiometric zirconia, respectively. All energies refer to structurally optimized systems. Negative E_{ads} values indicate a gain in energy (exothermic process), while positive values indicate an energy cost (endothermic process).

Finally, atomic charges have been estimated with the Bader decomposition scheme.[200] Effective Bader charges are defined as $Q_{eff} = Z_{VAL} - q$, with Z_{VAL} the number of valence electrons considered by VASP and q the charge output from the Bader analysis.

Chapter 3

Nanostructuring Zirconia

1 Atomic Structure and Stability of Zirconia Nanoparticles[1]

1.1 Introduction

The properties of zirconia can change from one polymorph to another. Although the monoclinic phase is the thermodynamically stable one at temperatures up to 1175 ºC,[41,42] the tetragonal is the most interesting phase regarding the catalytic and mechanical properties. Some ways to stabilize this phase at room temperature described in the Introduction chapter, are among others, the doping with Mg^{2+}, Ca^{2+}, or Y^{3+} cations, and nanostructuring down to sizes smaller than 10 nm.[47] However, within the nanoscaled tetragonal phase, properties and stability may also change drastically with different morphologies and sizes as we are in a non-scalable regime. Thus, the goal of this section is the study of the role of low dimensionality and morphology on the thermodynamic stability and reducibility properties of zirconia.

The zirconia nanoparticles designed and characterized in this section are the computational models that will be used in all the chapter to study the chemistry of nanoscaled zirconia. So, in the characterization of these systems, we have also studied the effect of the approach used to treat the exchange-correlation energy. In particular, we compare PBE and PBE+U results to those calculated with the hybrid PBE0 functional. Thus, the robustness of the conclusions is limited to the selected models and not to the computational approach.

[1] The content of this section is published in A. Ruiz-Puigdollers, F. Illas, G. Pacchioni. Structure and Properties of Zirconia Nanoparticles from Density Functional Theory Calculations. *J. Phys. Chem. C* 2016, 120, 4392, and A. Ruiz Puigdollers, F. Illas, G. Pacchioni. ZrO_2 Nanoparticles: A Density Functional Theory Study of Structure, Properties and Reactivity. *Rend. Fis. Acc. Lincei* 2017, 28, 19.

Computational Details

PBE and PBE+U calculations have been performed with VASP 5.3 as described in Chapter §2.6. For hybrid PBE0 calculations, we used the FHI-AIMS 5.2 code. This software uses an all-electron atom-centered numerical basis set, which is more accurate and appropriate for hybrid functionals than the VASP basis sets based on planewaves. To assess the possible influence that the different basis set may have when compared with VASP results, PBE calculations were also performed with the all-electron numerical basis set in FHI-AIMS.

1.2 Models of Zirconia Nanoparticles

Designing the structure of a representative model for zirconia nanoparticles is not easy. In fact, the determination of the exact geometry of a nanostructured oxide is still far from being solved. Nanoparticles are relatively small systems with numerous different atomic configurations possible, which leads to a potential energy surface too complex to be explored with high-level ab initio methods. However, heterogeneous catalysis focuses rather on relatively large nanoparticles, but still computationally feasible, whose properties can be scalable to the bulk regime. Since this work is more focused on the reactivity of the surfaces, whether the nanostructures are in the global minimum or not is not an important issue.

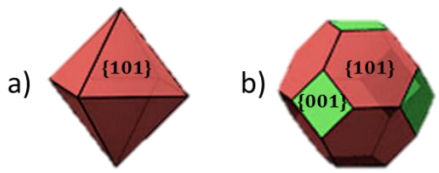

Figure 3.1. Schematic representation of (a) octahedral and (c) cuboctahedral models for zirconia nanoparticles.

A good starting point to design nanostructured zirconia models is the analysis of the lattice plane orientations in bulk zirconia. This idea is analogous to the Wulff construction at the nanoscale. So, to create the nanoparticle models, bulk tetragonal zirconia was cleaved along the normal directions of O-terminated {101} surfaces, which is the most stable surface in this phase. It resulted in octahedral or bipyramidal-shaped nanoparticles whose eight facets exhibit an O-terminated (101) surface, Figure 3.1a. Then, the six Zr corners of the octahedral nanoparticles were removed resulting in O-terminated {001} facets in the corners, Figure 3.1b. This model is referred as cuboctahedron or truncated octahedron.

The designed octahedral-based shape for zirconia nanoparticles is consistent with the relative thermodynamic stability between surfaces in tetragonal zirconia, since the O-

terminated {101} and {001} ones are the most stable for this phase.[201,202,203] This kind of model was found by Grena et al. in a Car-Parrinelo molecular dynamics to be the stable shape when zirconia nanoparticles are surrounded by water.[204] Also, 2 nm nanoparticles of CeO_2, an oxide with the same fluorite-type structure as ZrO_2, were experimentally characterized to be octahedral and cuboctahedral.[205] The same most stable morphology for CeO_2 nanoparticles was found by Neyman et al. by computationally exploring their configurational space.[93,206] Also the chemically related TiO_2 adopts at the nanoscale octahedral and cuboctahedral shapes.[207,208]

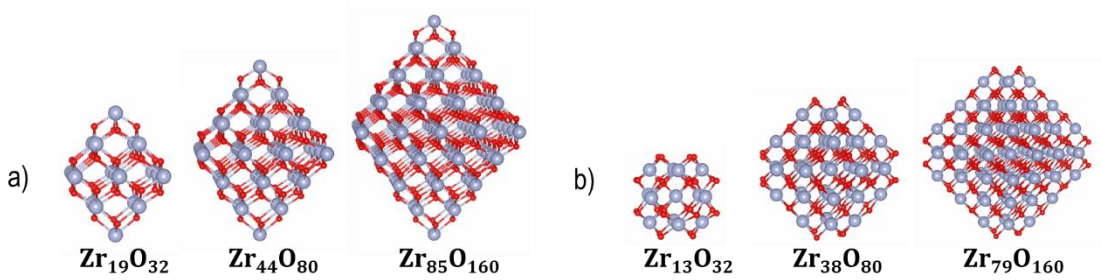

Figure 3.2. Models of (a) octahedral $(ZrO_{2-x})_n$ and (b) cuboctahedral $(ZrO_{2+x})_n$ nanoparticles. Zr is represented by big blue atoms and O by small red atoms.

The six models generated for zirconia nanoparticles are shown in Figure 3.2. The {101} cleavage from the bulk end up in the compositions $Zr_{19}O_{32}$, $Zr_{44}O_{80}$, and $Zr_{85}O_{160}$, and in diameter sizes after optimization at the PBE+U level of 0.90, 1.40, and 1.92 nm, respectively. Upon removing the Zr corner atom –cutting along the {001}–, the cuboctahedral shaped models resulted in compositions $Zr_{13}O_{32}$, $Zr_{38}O_{80}$, and $Zr_{79}O_{160}$. The octahedral nanoparticles are oxygen deficient (reduced), while the cuboctahedral are oxygen rich (oxidized). To obtain the ZrO_2 stoichiometry, one possibility is to remove the excess O atoms from the oxidized nanoparticles. However, this would lead to facets that do not exhibit the bulk-like surfaces. Instead, a different number of corner Zr atoms was removed from the octahedral models. Thus, three, four, and five Zr atoms were removed from the corners of the octahedral models generating the $Zr_{16}O_{32}$, $Zr_{40}O_{80}$, and $Zr_{80}O_{160}$ stoichiometric nanoparticles, referred as partly truncated octahedral, Figure 3.3.

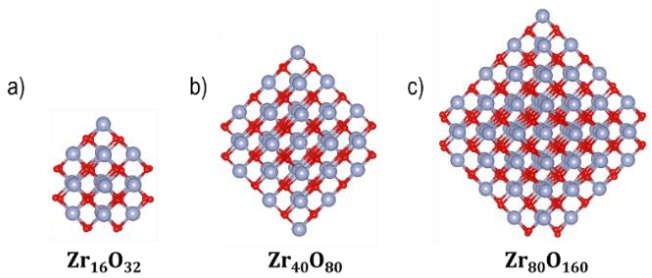

Figure 3.3. Models of partly truncated octahedral ZrO_2 nanoparticles. Zr is represented by big blue atoms and O by small red atoms.

Table 3.1. Optimized (PBE+U) average coordination number of Zr ions, $<N>_{Zr}$, and minimum, maximum, and average Zr-O, $d_{Zr\text{-}O}$, Zr-Zr, $d_{Zr\text{-}Zr}$, bond distances in Å.

	$\langle N\rangle_{Zr}$	$d_{Zr\text{-}O,min}$	$d_{Zr\text{-}O,max}$	$\langle d_{Zr-O}\rangle$	$d_{Zr\text{-}Zr,min}$	$d_{Zr\text{-}Zr,max}$	$\langle d_{Zr-Zr}\rangle$
ZrO_2 bulk	8.00	2.16	2.30	2.23	3.65	3.68	3.67
				Partly truncated octahedral			
$Zr_{16}O_{32}$	5.38	1.94	2.49	2.14	2.97	3.65	3.35
$Zr_{40}O_{80}$	6.10	1.96	2.45	2.18	3.26	3.50	3.38
$Zr_{80}O_{160}$	6.75	2.04	2.92	2.20	3.37	3.54	3.44
				Octahedral			
$Zr_{19}O_{32}$	5.47	2.11	2.24	2.18	3.18	3.18	3.18
$Zr_{44}O_{80}$	6.18	2.11	2.25	2.19	3.18	3.51	3.29
$Zr_{85}O_{160}$	6.59	2.09	2.40	2.22	3.28	3.67	3.54
				Cuboctahedral			
$Zr_{13}O_{32}$	6.15	2.11	2.18	2.15	3.48	3.51	3.49
$Zr_{38}O_{80}$	6.42	2.03	2.44	2.18	3.29	3.57	3.43
$Zr_{79}O_{160}$	6.78	2.08	2.31	2.20	3.42	3.68	3.55

In order to estimate structural relaxation after the optimization with respect to the bulk phase, the average, minimum, and maximum Zr-O and Zr-Zr bond distances, calculated at the PBE+U level, are summarized in Table 3.1. Despite that the crystallinity of the tetragonal phase is not entirely conserved after geometry optimization, the average Zr-Zr bond distance can provide an estimate of the degenerate lattice parameter (a_0) of a tetragonal unit cell. All nanoparticles showed an average Zr-Zr distance smaller than the bulk lattice parameter, 3.65 Å, and it increased with the size as the bulk regime is approached. The decrease of the lattice constant from bulk to the nanoscale is an expected behavior since a significant fraction of ions in nanoparticles form shorter bonds, mainly those in the surface, to compensate the undercoordination, so total Zr-Zr average decreases. This lattice contraction has been demonstrated by Yoshiasa et al. and by Thomas et al. with experimentally prepared 5 nm and

1.5 nm t-ZrO_2 nanoparticles, respectively.[209] Also, from Table 3.1, it can be noted that the smaller nanoparticles the wider the range of variation of both Zr-Zr and Zr-O bond distances (the difference between maximum and minimum), due to a larger local structural relaxation and loss of crystallinity. In short, smaller nanoparticles are more fluxional objects.

1.3 Formation Energies

In this section, a description of the thermodynamic stability of the different nanoparticles is provided as a function of composition and size, and compared to the regular (101) ZrO_2 surface. We have calculated the formation energy per Zr atom and with respect to the elemental components (Eq. 44) at PBE, PBE+U, and PBE0 levels in order to compare the effect of the exchange-correlation functionals on the stability of the zirconia nanostructures, Table 3.2. As described in §3.1.1, PBE0 calculations have been performed with a numerical basis set. However, practically the same results were obtained at PBE level using both the numerical and planewave basis sets. This allows to compare the PBE and PBE+U results with those PBE0, as the basis set seems to have a negligible effect on the formation energies. In the following, the discussed PBE results will refer to those calculated on a planewave basis set.

Table 3.2. Formation energies in eV per Zr atom from PBE, PBE+U, and PBE0 calculations for bulk t-ZrO_2, partly truncated octahedral, octahedral, and cuboctahedral ZrO_2 nanoparticles.

	PBE[a]	PBE[b]	PBE+U	PBE0
ZrO_2 bulk	-10.30	-10.38	-8.19	-11.00
	Partly truncated octahedral			
$Zr_{16}O_{32}$	-8.61	-8.63	-6.27	-9.02
$Zr_{40}O_{80}$	-9.25	-9.30	-6.91	-9.73
$Zr_{80}O_{160}$	-9.48	-9.52	-7.17	-9.86
	Octahedral			
$Zr_{19}O_{32}$	-7.43	-7.45	-5.03	-7.80
$Zr_{44}O_{80}$	-8.41	-8.44	-6.09	-8.88
	Cuboctahedral			
$Zr_{13}O_{32}$	-7.74	-7.75	-5.33	-8.09
$Zr_{38}O_{80}$	-9.05	-9.07	-6.77	-9.59

[a]Computed with planewave basis set.
[b]Computed with all-electron atom-centered numerical basis set.

Comparing the different density functionals, the Hubbard U correction to the PBE functional clearly yields smaller formation energies, or less negative. So, improving the gap has a negative effect on the energetic stability. Instead, the hybrid PBE0 functional provides

slightly larger (more negative) formation energies compared to PBE. Also, the effect of the U correction is size sensitive. The PBE+U formation energy changes around 30% with respect to PBE in smaller nanoparticles, and 21% in bulk. Instead, the PBE0 values are always 5% larger than PBE ones. Knowing that the experimental formation energy for bulk ZrO_2 is -11.41 eV[210] (obtained at 298.15 K), it can be concluded that the PBE0 approach reproduces with greater accuracy the energetics of these systems.

The dependence of the formation energies with the size of the structures has been evaluated by plotting them against the average coordination number of the Zr ions, $\langle N \rangle_{Zr}$ (the average number of O ions directly coordinated to each Zr ion), Figure 3.4. Interestingly, within the same configuration –octahedral, cuboctahedral, and partly truncated octahedral– the formation energies, calculated at the PBE+U level, correlate linearly with $\langle N \rangle_{Zr}$ and converge to the bulk value, with regression coefficients of 0.99. This derives an important concept: from the correlation obtained, formation energies of bigger nanoparticles with sizes not yet computationally feasible could be extrapolated.

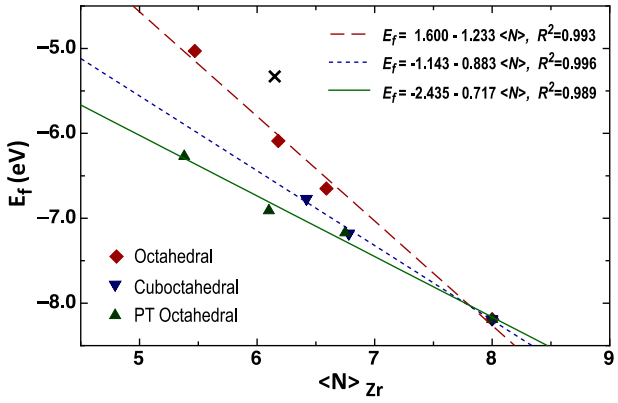

Figure 3.4. PBE+U formation energies in eV per Zr atom for zirconia nanoparticles and bulk ($\langle N \rangle_{Zr}$ = 8.0). The fitted linear correlation between the nanoparticles and the bulk value for each morphology is indicated. $Zr_{13}O_{32}$ is not included in the correlation of cuboctahedral nanoparticles (black cross).

By comparing the different morphologies, the partly truncated octahedral structures are clearly the most stable, since these maintain a full ZrO_2 stoichiometry. Octahedral nanoparticles, despite they exhibit the most stable (101) surface in all facets, they are oxygen deficient, as seen in §3.1.2, which destabilize the nanoparticles with respect to those stoichiometric. Also, due to a higher symmetry, octahedral nanoparticles underwent a lower structural relaxation than those partly truncated, so a lower stabilization. This indicates that the relative stability of the exposed facets, which is the main argument of the Wulff

construction, is not enough to predict the stability of a given morphology. Other reasons like the special electronic structure play a key role, as it will be seen later.

Finally, the formation energies of cuboctahedral nanoparticles are only slightly larger (less negative) than those of stoichiometric structures, in spite of the large amount of low-coordinated O ions in {001} facets. The instability comes from the presence of peroxide-like O atoms due to the excess of O atoms with respect to the number of Zr ions. However, this is true for this definition of the formation energy (Eq. 44), but it will be shown later that these systems are thermodynamically unstable with respect to the formation of $O_{2,(g)}$.

1.4 Oxygen Vacancies

We created a neutral O vacancy in each nanoparticle and considering several sites with different coordination number. The formation energies defined as Eq. 45 and at PBE+U level are reported in Table 3.3. In the regular (101) surface, the formation of an O vacancy costs 5.97 eV in the surface (O_{3c}) and 5.67 eV in the subsurface (O_{4c}). These values are typical of a nonreducible oxide, and are in good agreement with previous reported results.[179] In the stoichiometric nanoparticles, O_{2c} sites are the most favorable position to create a vacancy, with formation energies of +3.94 ($Zr_{16}O_{32}$), +3.80 ($Zr_{40}O_{80}$), and +2.62 eV ($Zr_{80}O_{160}$). The O_{3c} sites in the surfaces of the nanoparticles have a lower formation energy than those O_{3c} in the (101) surface: +5.89 ($Zr_{16}O_{32}$), +4.86 ($Zr_{40}O_{80}$), and +4.42 eV ($Zr_{80}O_{160}$). Thus, O atoms in low coordinated sites are the easiest to remove, representing the important catalytic sites in redox reactions where the transfer of an O atom is involved. Also, the preference to localize the extra charge in a singlet state in the vacancy rather than to reduce Zr^{4+} ions to Zr^{3+} (resulting in a triplet state) is generally observed in the nanoparticles, as it occurs in the extended (101) zirconia surface and in nonreducible oxides.

A clear trend between the formation energies with size cannot be easily defined. The stability of the O vacancies depends mainly on two factors: the stability of the acceptor Zr 4d gap state, in other words, where the extra charge is localized in the nanoparticle (electronic effect), and the local structural relaxation around the vacancy (geometric effect). These factors become even more important in nanostructured materials, which makes the stability of the O vacancies a non-scalable property.

In the octahedral nanoparticles, the formation energies of O vacancies are higher than those in the stoichiometric ones, as these systems are already reduced containing reduced Zr sites. Instead, the cuboctahedral structures show negative formation energies. This means that they

are actually unstable and would spontaneously release O_2 to the gas phase. We attribute this instability to the selected bulk-like models. Previous DFT studies predicted that 1-1.5 nm ZrO_2 nanoparticles do not exhibit a bulk-like morphology in oxidizing environments but they are passivized with molecular and peroxide-like O_n^q groups on the surface.[211]

Table 3.3. Formation energies in eV of *n*-coordinated O_{nc}-vacancies of zirconia bulk and nanoparticles, in singlet (S) or triplet (T) electronic ground state.

	Corner – O_{2c}	Corner – O_{3c}	Facet – O_{3c}	Inner – O_{4c}
ZrO_2 bulk	-	-	+5.97 (S)	+5.67 (S)
	Partly truncated octahedral			
$Zr_{16}O_{32}$	+3.94 (S)	-	+5.89 (S)	+5.15 (S)
$Zr_{40}O_{80}$	+3.70 (S)	+4.16 (T)	+4.86 (T)	+5.11 (S)
$Zr_{80}O_{160}$	+2.62 (S)	+5.26 (S)	+4.42 (T)	+2.17 (S)
	Octahedral			
$Zr_{19}O_{32}$	-	+6.11 (S)	-	+4.16 (S)
$Zr_{44}O_{80}$	-	+5.86 (T)	+6.69 (S)	+4.74 (S)
	Cuboctahedral			
$Zr_{13}O_{32}$	-2.35	-	-	-2.63
$Zr_{38}O_{80}$	-1.02	-	-1.02	-0.10

1.5 Electronic Structure from Bulk Zirconia to Nanoparticles

Detailed information on the electronic structure of bulk ZrO_2 and $(ZrO_2)_n$ nanoparticles was obtained from their Projected Density of States (PDOS). We also tested the performance of the different density functionals on the electronic structure.

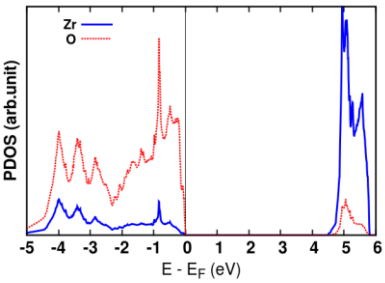

Figure 3.5. Projected Density of States (PDOS) of ZrO_2 bulk, from a PBE+U optimization. The zero of energy corresponds to the Fermi level.

In Figure 3.5, the PDOS of bulk ZrO_2 is shown. The VB is composed by occupied O 2p states of O^{2-} ions, and the CB is composed by empty Zr 4d states of Zr^{4+} ions. At the PBE+U level of theory, a KS band gap of 4.43 eV was obtained. Differently, stoichiometric nanoparticles are partly truncated octahedrons that contain a large fraction per volume of both

low-coordinated Zr and O ions, mainly those of edges and corners. This gives rise to empty Zr 4d states that are stabilized with respect to the CB, Figure 3.6. In other words, low-lying empty states appear in the gap that can act as electron acceptors. This means that, in a redox process in which the nanoparticle is reduced (oxygen loss or hydrogenation), the reducing electrons will be first localized in the low-coordinated Zr sites that will change from Zr^{4+} to Zr^{3+}. Similarly, low-coordinated O ions give rise to O 2p states destabilized with respect to the VB, Figure 3.6. High-lying occupied states appear in the gap that can act as electron donors, which will be the first transferred in an oxidation process. This is the interesting feature of the oxide nanostructuring that is not present in bulk and extended surfaces (Figure 3.5). Note, however, that the $Zr_{40}O_{80}$ nanoparticle at the PBE+U level, exhibits a *clean* band gap with no defective gap states. This is attributed to a special symmetry of the designed model for this composition. It will be seen that, due to this, this nanoparticle has a general behavior which is reminiscent of that of the bare surface. In general, the special electronic structure of nanoparticles will play a fundamental role in the reactivity of ZrO_2 since it may enhance the interaction with deposited metal catalysts and molecules, the tendency to accept new electrons, and the photocatalytic activity by effectively reducing the transition energies (band gap).

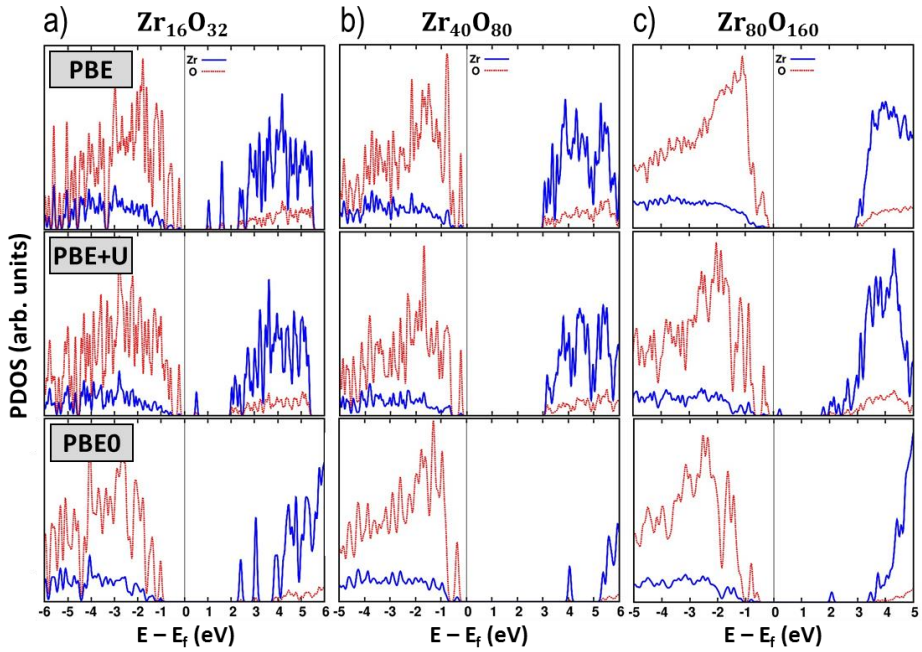

Figure 3.6. Projected Density of States (PDOS) of (a) $Zr_{16}O_{32}$, (b) $Zr_{40}O_{80}$, and (c) $Zr_{80}O_{160}$ stoichiometric nanoparticles from PBE, PBE+U, and PBE0 calculations. The zero of energy corresponds to the Fermi level.

As expected, these electronic features are sensible to the density functional considered. The PDOS are clearly qualitatively different between the three approaches considered, Figure 3.6. A comparison of the band gaps calculated with the different methods is provided in Table 3.4. To calculate the band gap in nanoparticles, we considered both the Kohn-Sham HOMO-LUMO gap and the difference between the estimated edges of VB and CB without considering localized gap states that come from low coordinated sites. In all cases, the Hubbard U correction to the PBE functional enhances the gap, as expected, but still remains below the experimental value in the case of ZrO_2 bulk and surface. The PBE0 functional instead overestimates it compared to the PBE value, and even above the experimental value in bulk and surface. However, it is important to note that the experimental gap is usually obtained from polycrystalline samples, and the definition of the band gap in the experimental techniques may differ from that considered in DFT ($HOMO_{KS} - LUMO_{KS}$).

Table 3.4. Band gaps in eV of bulk, (101) surface, and stoichiometric nanoparticles of ZrO_2, from PBE, PBE+U, and PBE0 calculations.

	Gap	PBE	PBE+U	PBE0
t-ZrO_2 Bulk	CB – VB	3.72	4.43	6.13
t-ZrO_2 (101)	CB – VB	3.45	4.01	5.94
$Zr_{16}O_{32}$	CB – VB	3.26	3.28	5.33
$Zr_{40}O_{80}$	CB – VB	3.59	3.80	6.12
$Zr_{80}O_{160}$	CB – VB	3.61	3.63	5.20
$Zr_{16}O_{32}$	HOMO – LUMO	1.27	0.75	3.44
$Zr_{40}O_{80}$	HOMO – LUMO	3.27	3.37	4.40
$Zr_{80}O_{160}$	HOMO – LUMO	3.22	0.44	2.67
experiment		5.5[a] [212], 5.68[a] [49], 5.78[b] [48]		

[a]From Photoemission Spectroscopy + Inverse Photoemission Spectroscopy (PES+IPS) experiments.
[b]From Reflectance Spectroscopy (VUV) experiments in Y-doped ZrO_2.

Thus, defining the best DFT approach may depend on the observable of interest. For instance, the PBE0 is a computationally expensive approach that overestimates the gap but reproduces accurately the energetics. The PBE+U is much less expensive that partly corrects the KS gap but underestimates the formation energies. However, any of them provides a scalable trend between the band gap and the size.

Octahedral nanoparticles, since they have an oxygen deficient stoichiometry, display an electronic structure that is analogous to that of stoichiometric zirconia with O vacancies. The $Zr_{19}O_{32}$, $Zr_{44}O_{80}$, and $Zr_{85}O_{160}$ stoichiometries are equivalent to 6, 8, and 10 O vacancies in a regular lattice, respectively. This means that these systems contain 12, 16, and 20 excess

electrons. When a single neutral O vacancy is created in an oxide, the two excess electrons can be coupled in a singlet state (non-magnetic) or in a triplet state (magnetic), as explained in the Introduction chapter. However, in the octahedral nanoparticles, the coupling of the reducing 12, 16 and 20 electrons is not so trivial. They can arrange in low-spin states (diamagnetic or antiferromagnetic), or in multiple magnetic states (totally or partially ferromagnetic), whose relative energies depend on the temperature. The next section §5 will deep on these magnetic properties of the octahedral reduced nanoparticles.

Cuboctahedral nanoparticles are characterized by an O-rich composition. Formally, there are 6, 4, and 2 excess O atoms in $Zr_{13}O_{32}$, $Zr_{38}O_{80}$, and $Zr_{79}O_{160}$, respectively. These O atoms are not fully reduced and maintain an atom-like electronic configuration with two unpaired electrons in O 2p states. This results in a global net magnetic moment of 12, 8, and 4, respectively, with the spin density localized on surface O sites. The partial occupation of the O 2p states generates low-lying empty acceptor states in the gap, which modifies the chemistry of the nanostructured oxide giving a strong oxidizing power. However, as it has been seen before, bulk-like cuboctahedral nanoparticles are not realistic models for oxidizing conditions, being even unstable with respect to the formation of $O_{2,(g)}$.

2 Reactivity of ZrO_2 Nanoparticles: Au and AuCO Adsorption[2]

2.1 Introduction

One of the most active known catalysts is that formed with Au particles for a large variety of chemical reactions. Au has been deposited probably in all oxides and tested its catalytic activity. For example, ZrO_2 supported Au particles is widely used in reactions like the water gas shift (WGS),[65] the methanol synthesis from CO_2 and H_2,[213] the CO oxidation,[33,71,72,73] and the hydrogenation of 1,3-butadiene.[214,215]

It is well-known that the support has a fundamental effect on the catalytic activity. Upon deposition of the metal catalyst, several factors come into play to improve the reactivity of the metal, like changes in the electronic structure by chemical bonding, possible charge transfer at the interface (see §1.4.2). For instance, it has been found that charging negatively deposited Au particles enhances their activity in the CO oxidation reaction,[216,217] or instead charging positively increases the activity in hydrogenation reactions[214,215] and the WGS reaction.[218]

Regarding the morphologies of the support, extended and non-defective (stoichiometric) zirconia surfaces as well as those with point defects and grain boundaries have been investigated as a support for many metal particles.[162] However, the influence of oxide nanostructuring on the adsorption properties has received less attention. Oxides in the form of nanoparticles are expected to show a better reactivity due to undercoordination that leads to a special electronic structure and fluxionality. For example, Au catalysts supported on 5 – 15 nm zirconia nanoparticles show 10 times higher activity than those supported on 40 – 200 nm nanoparticles.[72] Even an inactive metal catalyst become active when deposited in a nanostructured oxide instead of on extended surfaces.[219] Also, in contrast to the bulk regime, surfaces on nanoparticles are more irregular, with the presence of steps, kinks, and corners, in which most of the chemical reactions take place.[84-87] So steps in surfaces are also expected to be more reactive toward metal catalysts and molecules. In this section, we systematically compare the adsorption properties of a Au atom on the terraces and steps of the (101) t-ZrO_2 surface, and on stoichiometric and O deficient ZrO_2 nanoparticles. The comparison between the different supports aims at providing a general picture of the role played by the undercoordination and nanostructuring on the adsorption and electronic properties of a metal atom on zirconia.

[2] The content of this section is published in A. Ruiz Puigdollers, F. Illas, G. Pacchioni. Effect of Nanostructuring of the Reactivity of Zirconia: A DFT+U Study of Au Atom Adsorption. *J. Phys. Chem. C* 2016, 120, 17604.

Computational Details

The (101) t-ZrO_2 surface was modeled with a 3 x 2 supercell with 5 layers ($Zr_{60}O_{120}$ slab model). The step between (101) terraces was modeled by cutting the (156) t-ZrO_2 surface in a 2 x 1 supercell with 5 layers ($Zr_{100}O_{200}$ slab model, Figure 3.7). We always considered a minimum vacuum of 15 Å above the surface. The same partly truncated octahedral and octahedral zirconia nanoparticles described in previous section §3.1.2 were used for stoichiometric and O deficient nanostructured zirconia, respectively. Due to the large dimension of the slab supercells and the zero-dimensional character of the nanoparticles, all calculations were performed at the *Γ*-point.

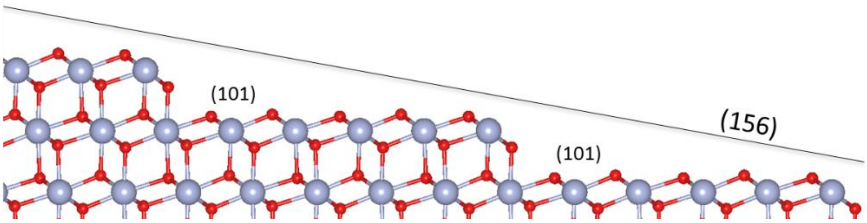

Figure 3.7. Structure of the stepped (156) ZrO_2 surface. Zr is represented by big blue atoms, and O by small red atoms.

2.2 Au Adsorption on Stoichiometric ZrO_2

2.2.1 Regular and Stepped (101) Surfaces

First, a Au atom was deposited on the (101) terrace of t-ZrO_2, in both the regular (101) and stepped (156) slab models. The preferred configuration is a bridge position between a Zr_{7c} and O_{3c} surface sites, Figures 3.8(a,b). Despite the same structure, in the regular (101) slab model, Au is adsorbed with an energy of -0.90 eV, while in the (156) slab a slightly higher energy is obtained, -1.05 eV, Table 3.5. In the edge of the step, two stable configurations were found for the Au adsorption. In both, Au forms a bridge between low-coordinated Zr_{6c} and O_{2c} sites along the step, named here *edge I* and *edge II* positions, Figures 3.8(c,d), respectively. It is important to note that, in the *edge II* configuration, the Au atom partially extracts the low-coordinated O atom from the edge. Also, this is the preferred configuration with an adsorption energy of -1.62 eV compared to -1.32 eV in *edge I* configuration. This is a first indication that undercoordination may promote the reduction of the oxide by the easier loss of low-coordinated O atoms.

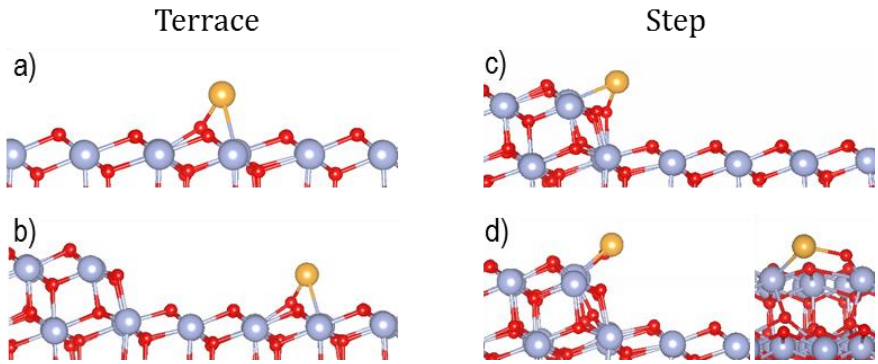

Figure 3.8. Structures for Au adsorption on the (a) (101) terrace of the (101) slab model, (b) (101) terrace of the (156) stepped model, (c) edge I, and (d) edge II. Zr is represented by big blue atoms, O by small red atoms, and Au by big golden atoms.

The calculated Bader charge on the deposited Au atoms is always virtually zero (between -0.14 and -0.17 |e|). So, Au maintains the atom-like electronic configuration $5d^{10}\ 6s^{1}$ showing also a local magnetic moment around 0.4 μ_B. This indicates that the bonding is characterized by a polar covalent mixing, and no net charge transfer occurs at the Au_1/ZrO_2 interface. Comparing the step and terrace sites, the Au binding energies are clearly enhanced on step sites due to the undercoordination. The higher reactivity of steps has been also observed on MgO (-1.26 eV vs -0.89 eV)[220] and on TiO_2 (-0.78 eV vs -0.25 eV).[87] However, while on MgO Au remains neutral like on ZrO_2, as both are nonreducible oxides, it is oxidized on TiO_2 (reducible oxide).

Table 3.5. Adsorption energies, $E_{ads,Au}$, magnetic moment, μ_{Au}, and Bader charge, q_{Au}, of a single Au atom adsorbed on the terrace and steps of the (101) surface and on nanoparticles of zirconia.

system	site	$E_{ads,\ Au}$ (eV)	μ_{Au} (μ_B)	q_{Au} (|e|)	
(101) slab	ZrO bridge	-0.90	0.4	-0.16	Fig. 3.8a
(156) slab	terrace	-1.05	0.4	-0.17	Fig. 3.8b
	edge I	-1.32	0.4	-0.17	Fig. 3.8c
	edge II	-1.62	0.4	-0.14	Fig. 3.8d
$Zr_{80}O_{160}$	corner O_{2c}	-2.31	0	+0.26	Fig. 3.9a
	corner Zr_{4c}	-2.81	0	-0.60	Fig. 3.9b
	edge ZrO bridge	-1.17	0.2	+0.05	Fig. 3.9c
$Zr_{40}O_{80}$	corner Zr_{4c}	-1.32	0.1	-0.44	Fig. 3.9d
	edge O_{2c}	-2.62	0.4	-0.16	Fig. 3.9e
	edge ZrO bridge	-2.32	0.4	-0.16	Fig. 3.9f
$Zr_{16}O_{32}$	corner O_{2c}	-1.10	0	+0.40	Fig. 3.9g
	edge O_{2c}	-1.36	0	+0.33	Fig. 3.9h

2.2.2 Stoichiometric Nanoparticles

Different Au adsorption properties were investigated on the nanoparticles. The most stable adsorption sites are, as expected, in low coordinated sites in corners and edges. On $Zr_{80}O_{160}$, Au is adsorbed in the Zr_{4c}-terminated and O_{2c}-terminated corners, Figures 3.9(a,b), with an energy of -2.81 and -2.31 eV, respectively, Table 3.5. In the edge, it was adsorbed with a lower energy (-1.17 eV). Note that, in the corners, the binding energy is more than twice the energy found on the regular (101) terrace (-0.90 eV). Interestingly, the Au atom was oxidized by simply deposition on the O_{2c}-terminated corner (Bader charge of +0.26 |e|), and reduced on the Zr_{4c}-terminated corner (Bader charge of -0.60 |e|). On $Zr_{40}O_{80}$, the most stable adsorption sites are instead Zr-O bridge positions in the edge, Figures 3.9(e,f), with binding energies -2.63 and -2.32 eV, respectively. In the Zr_{4c} corner, Au is adsorbed with an energy of -1.32 eV, Figure 3.9(d). Although this adsorption site is less stable, the Au atom is reduced, showing a Bader charge of -0.44 |e|. On the $Zr_{16}O_{32}$ nanoparticle, Au was adsorbed in an edge site between two O_{2c} ions (-1.10 eV) and on top of an edge O_{2c} ion (-1.36 eV), Figures 3.9(g,h). In both cases, the Au atom was oxidized, showing Bader charges of +0.40 and +0.33 |e|, respectively.

The adsorption properties are clearly enhanced on the nanoparticles with respect to the extended surfaces. Already in the steps between (101) terraces, the binding energies are lowered due to a higher chemical potential of the low coordinated step sites, but no charge transfer occurred. The higher reactivity of the nanoparticles can be attributed to two main aspects. One is the higher structural flexibility that stabilizes the adsorption by larger local relaxations around the Au atom. The second is the special electronic structure different from the surfaces, as seen in Figure 3.6, that gives rise to redox processes that promote the Au binding by new electrostatic interactions. In particular, on top of a corner Zr site, the attractive Zr-Au interaction shifts downward the Au 6s level such that it receives charge from the highest occupied O 2p levels, as seen in $Zr_{80}O_{160}$ and $Zr_{40}O_{80}$ where a Zr-Au^- bond was formed. Instead, the repulsive Au-O interaction shifts upward the Au 6s level such that the 6s electron is transferred to the low-lying Zr 4d states, as occurred on O_{2c} sites of $Zr_{80}O_{160}$ and $Zr_{16}O_{32}$ where O-Au^+ bonds were formed. This oxidative adsorption did not exist in $Zr_{40}O_{80}$ since it does not exhibit empty gap Zr 4d states at PBE+U, Figure 3.6.

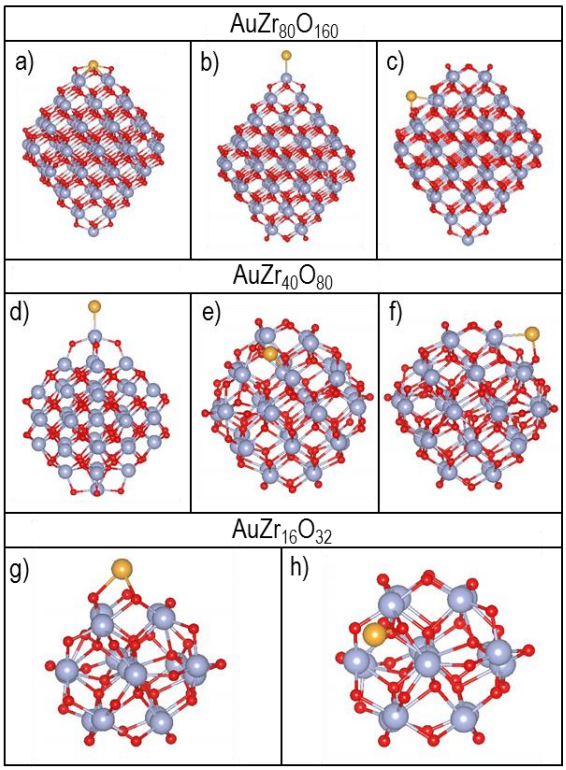

Figure 3.9. Structures for Au adsorption on (a,b) corner and (c) edge sites of $Zr_{80}O_{160}$, (d) corner and (e,f) edge sites of $Zr_{40}O_{80}$, and (g) corner and (h) edge sites of $Zr_{16}O_{32}$. Zr is represented by big blue atoms, O by small red atoms, and Au by big golden atoms.

However, a clear trend of the Au adsorption properties with the size of the nanoparticles could not be drawn; we are still in a non-scalable regime. The stability and the occurrence of a charge transfer are difficult to predict and depend on the details of the electronic structure, so on the morphology rather than on the size.

2.3 CO Adsorption on Au-Decorated ZrO_2

The CO molecule can probe the electron density or charge state of metal centers. On negatively charged metals, the CO stretching frequency is red-shifted compared to the gas phase (to lower wavenumbers or cm^{-1}) depending on the extent of back donation into the CO $2\pi^*$ antibonding orbital. On positively charged metals, it is blue-shifted (to higher cm^{-1} values). However, it has been found that on neutral Au atoms the CO can induce the metal to transfer its $6s^1$ electron, which inhibits the use of CO as a probe molecule. For example, on TiO_2, a reducible oxide, the TiO_2^--Au^+-CO complex has been detected by a blue-shift of the CO frequeny,[221] in

which TiO_2 is reduced. On MgO, since it is a hardly reducible oxide, the MgO-Au^+-CO^- complex was formed red-shifting the CO frequency.[222]

We adsorbed a CO molecule on a Au atom deposited on the ZrO_2 surface and nanoparticles. On the (101) surface, where adsorbed Au was neutral, CO withdraws a 42% of the charge density giving a stretching frequency of 1943 cm^{-1}, Table 3.6, which is red-shifted with respect to that in gas phase (2126 cm^{-1}). This is the behavior observed in MgO,[222] a nonreducible oxide. Similarly, when AuCO was adsorbed on a surface O vacancy, the CO frequency was red-shifted to 1956 cm^{-1}.

Table 3.6. Schematic representation of the charge states of the species before and after the adsorption of the CO molecule. Adsorption energies, E_{CO}, and CO stretching frequencies, υ_{CO}, of the CO molecule on top the Au atom, and fraction in % of the magnetic moment localized on the ZrO_2 support, $\%\mu_{ZrO2}$, and on the CO molecule, $\%\mu_{CO}$.

Au site	Initial state	Final state	E_{CO} (eV)	υ_{CO} (cm^{-1})	$\%\mu_{ZrO2}$	$\%\mu_{CO}$
			(101) surface			
	ZrO_2	ZrO_2-CO	-0.26	2127	0	0
ZrO bridge	$ZrO_2^0 - Au^0$	$ZrO_2 - Au^{\delta+} - CO^{\delta-}$	-1.13	1943	38	42
O vacancy	$ZrO_{2-x}^+ - Au^-$	$ZrO_{2-x}^+ - Au^- - CO^{\delta-}$	-0.47	1956	62	20
			$Zr_{80}O_{160}$			
corner O_{2c}	$ZrO_2^- - Au^+$	$ZrO_2^- - Au^+ - CO^0$	-2.20	2096	100	0
corner Zr_{4c}	$ZrO_2^+ - Au^-$	$ZrO_2^+ - Au^- - CO^0$	-0.45	2014	100	0
edge ZrO	$ZrO_2^0 - Au^0$	$ZrO_2^- - Au^+ - CO^0$	-2.57	2107	100	0
			$Zr_{40}O_{80}$			
corner Zr_{4c}	$ZrO_2^+ - Au^-$	$ZrO_2^+ - Au^- - CO^0$	-0.50	2033	76	6
edge O_{2c}	$ZrO_2^0 - Au^0$	$ZrO_2 - Au^{\delta+} - CO^{\delta-}$	-1.05	1937	32	44
edge ZrO	$ZrO_2^0 - Au^0$	$ZrO_2 - Au^{\delta+} - CO^{\delta-}$	-1.09	1957	34	43

On nanoparticles, the presence of Zr 4d gap states play a key role. In the Zr-O edge site of $Zr_{80}O_{160}$, in which the Au remained neutral (Table 3.5), the CO induced the transfer of the Au $6s^1$ electron to the oxide nanoparticle, forming the ZrO_2^--Au^+-CO^0 complex, Table 3.6. This is the same behavior observed in a reducible oxide like TiO_2.[221] Hence, in $Zr_{80}O_{160}$, we did not observe in any adsorption site a charge transfer to the CO $2\pi^*$ states like in the (101) surface. When the ZrO_2^--Au^+-CO^0 complex was formed, the CO frequency remained almost unchanged compared to the gas phase (2096 and 2107 cm^{-1} vs 2126 cm^{-1}). The positive charge of Au^+ shifts the CO frequency to the blue, while the back-donation from the Au 5d states shifts to the red, compensating the effect. In the ZrO_2^+-Au^--CO^0 complex, the negative charge

of Au^- leads to a moderate red-shift (2014 cm^{-1}). On the $Zr_{40}O_{80}$ nanoparticle, however, the CO induced the transfer of the Au $6s^1$ electron to the CO $2\pi^*$ states instead to the oxide. This led to a strong red-shift (1957 and 1937 cm^{-1} in edge and facet sites, respectively) as found on the regular (101) surface. In this respect, $Zr_{40}O_{80}$ behaves as a nonreducible oxide, a clear indication that different morphologies lead to different chemistry and points out the difficulty of making predictions in the nonscalable regime.

The difference between the two nanoparticles relies in their different electronic structure. The CO molecule is a Lewis acid that destabilizes the Au 6s state. If there are empty low-lying Zr 4d gap states like in the $Zr_{80}O_{160}$ nanoparticle, the Au electron can be transferred to the oxide. On the contrary, in the absence of such states like in $Zr_{40}O_{80}$, the Au electron is transferred to the antibonding orbitals of CO. Thus, the CO induces the oxidation of the Au atom, but depending on the reducibility of the support, the charge transfer occurs either to the oxide or to CO, with the consequent changes in its stretching frequency.

2.4 Au Adsorption on Reduced ZrO_{2-x}

In this section, we studied how nanostructuring affects the reactivity of zirconia in reducing conditions. For this, we considered the adsorption of a Au atom on the (101) terrace, steps and partly truncated nanoparticles (stoichiometric) with an O vacancy ($Zr_{16}O_{31}$ and $Zr_{40}O_{79}$), and on those octahedral that were O deficient ($Zr_{19}O_{32}$ and $Zr_{44}O_{80}$).

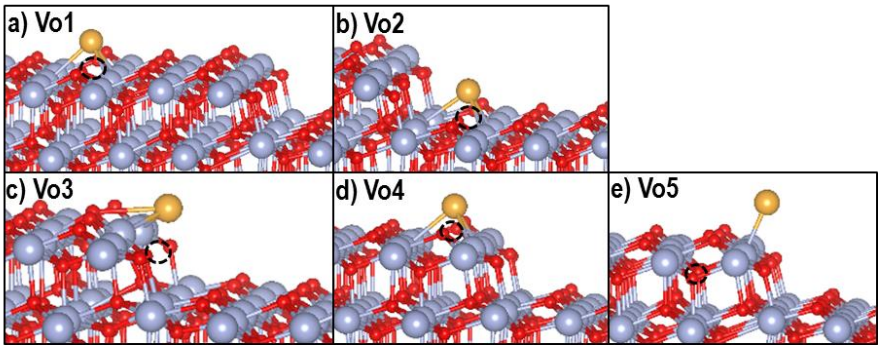

Figure 3.10. Structures for Au adsorption on the (a) Vo1, (b) Vo2, (c) Vo3, (d) Vo4, and (e) Vo5 O vacancies created on the stepped (156) slab model. Zr is represented by big blue atoms, O by small red atoms, and Au by big golden atoms. The O vacancy is indicated with a dotted circle.

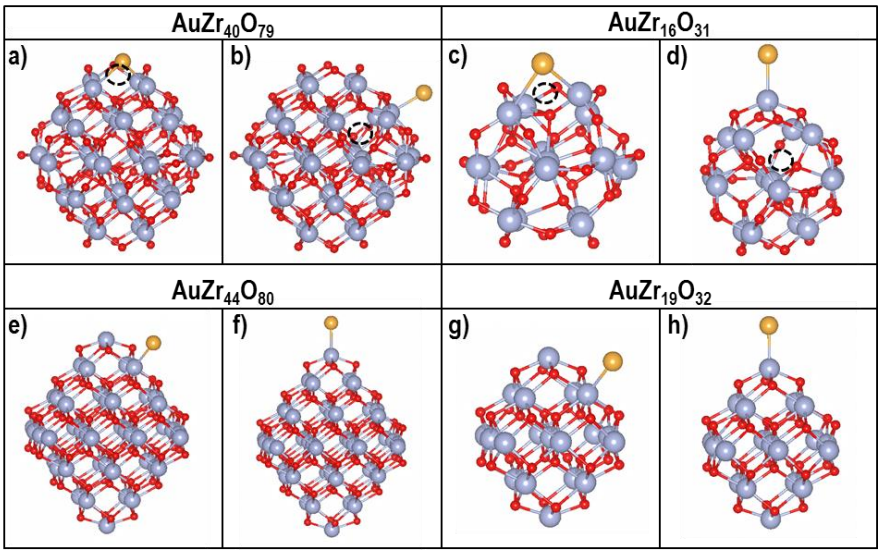

Figure 3.11. Structures for Au adsorption on top of a (a,c) surface and (b,d) inner O vacancy in $Zr_{40}O_{79}$ and $Zr_{16}O_{31}$, on top of a (e,g) Zr_{edge} ion and a (f,h) Zr_{corner} ion in $Zr_{44}O_{79}$ and $Zr_{19}O_{32}$. Zr is represented by big blue atoms, O by small red atoms, and Au by big golden atoms. The O vacancy is indicated with a dotted circle.

Table 3.7. Formation energy, $E_{f,Vo}$, of the O vacancy, adsorption energy, $E_{ads,Au}$, and Bader charges, q_{Au}, of a single Au atom adsorbed on the reduced (101) terrace and step and on nanoparticles of zirconia.

system	vacancy	Au site	$E_{f,Vo}$ (eV)	$E_{ads,Au}$ (eV)	q_{Au} (|e|)
(101) terrace	Vo1	Vo top	+5.97	-3.95	-0.89
	Vo5	Zr top	+5.78	-2.24	-0.57
(101) step	Vo1	Vo top	+5.95	-4.01	-0.90
	Vo2	Vo top	+5.95	-4.11	-0.73
	Vo3	Vo top	+5.80	-4.34	-0.83
	Vo4	Vo top	+6.13	-4.80	-0.75
	Vo5	ZrO bridge	+5.07	-2.83	-0.63
$Zr_{16}O_{31}$	corner-Vo	Vo top	+3.94	-3.63	-0.65
	inner-Vo	Zr_{corner} top	+5.15	-3.63	-0.62
$Zr_{40}O_{79}$	corner-Vo	Vo top	+3.70	-3.27	-0.63
	inner-Vo	Zr_{edge} top	+5.11	-2.43	-0.60
$Zr_{19}O_{32}$	-	Zr_{edge} top	-	-3.19	-0.62
		Zr_{corner} top		-3.36	-0.62
$Zr_{44}O_{80}$	-	Zr_{edge} top	-	-3.77	-0.62
		Zr_{corner} top		-3.77	-0.67

On the (101) terrace, Au is adsorbed on top of an O vacancy with an energy of -3.95 eV, Table 3.7, and -4.01 eV if we consider the stepped (156) model (Vo1, Figure 3.10a). For the

step, we considered 4 different positions to create an O vacancy (Vo2-Vo5). The Au binding energy is enhanced to energies of -4.11, -4.34, and -4.80 eV on the surface O vacancies Vo2, Vo3, and Vo4, respectively (Figures 3.10(b-d)). We also considered the creation of a subsurface O vacancy. The step also enhances the Au adsorption on a subsurface vacancy (-2.83 compared to -2.24 eV, in the step and terrace Vo5, respectively). In all cases, the Au atom is reduced by capturing one electron of the excess charge associated to the O vacancy, as seen by the largely negative Bader charges on Au (between -0.73 and -0.90 |e|, Table 3.7).

The deposition of Au on the reduced nanoparticles ($Zr_{16}O_{31}$, $Zr_{40}O_{79}$, $Zr_{19}O_{32}$, and $Zr_{44}O_{80}$, Figure 3.11), as expected, yields binding energies larger (more exothermic) than those on the stoichiometric $Zr_{16}O_{32}$ and $Zr_{40}O_{80}$ (around -3.2 – -3.8 eV, Table 3.7, vs around -1.3 – -2.6 eV, Table 3.6) However, the binding on the reduced nanoparticles is not as strong as on the reduced steps and surfaces (around -3.2 – -3.8 eV vs around -4 – -4.8 eV, Table 3.7). Nanostructuring to 0D structures decreases the reactivity of reduced zirconia toward Au compared to steps, which is an opposite behavior with respect to the stoichiometric nanoparticles. This is illustrated in Figure 3.12, in which the Au binding energies are plotted against the three different kinds of ZrO_2 morphologies –surface, step, and nanoparticles. At the nanoscale, zirconia becomes more reducible. Since O vacancies are more stable in the nanoparticles (lower formation energies, +3.70 and +3.94 eV vs +5.97 eV), the reactivity toward Au is reduced compared to the extended surface, where vacancies are unstable and thus more reactive.

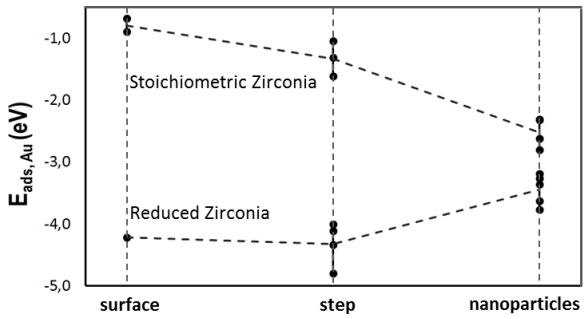

Figure 3.12. Adsorption energies, indicated with black points, of a Au atom on the three different morphologies of zirconia.

3 Reduction of Stoichiometric ZrO_2 Nanoparticles: H_2 Adsorption and H_2O Desorption[3]

3.1 Introduction

It has been said that the interest for novel forms of reduced zirconia has been increasing, thanks to its new and interesting applications found.[23,24,53,54] There are several mechanisms for the reduction of the zirconia surface. For instance, in the presence of deposited metal particles, surface O ions can spill over the metal leaving the O vacancy (reverse spillover). This process has been estimated to cost only 0.2 and 0.6 eV on a Ru_{10} cluster on TiO_2 and ZrO_2, respectively.[223] However, more typical is the reduction by a hydrogenation process and a subsequent desorption of water (dehydration), leaving behind an O vacancy per H_2 molecule.

I – hydrogenation $\quad ZrO_2 + H_2 \rightarrow H_2ZrO_2$

II – dehydration $\quad H_2ZrO_2 \rightarrow ZrO_{2-x} + H_2O$

In this process, the presence of a supported metal particle can facilitate the dissociation of H_2 and the spill over of H atoms to the surface to form OH^+ and Zr^{3+} cations. Alternatively, O ions can diffuse to the metal, react with adsorbed H atoms and desorb H_2O.[224]

However, in the absence of deposited metals, the direct reduction process $ZrO_2 + H_2 \rightarrow ZrO_{2-x} + H_2O$ is very endothermic for zirconia bulk and surfaces. For example, Hofmann et al. found from PBE calculations a reaction enthalpy of +2.71 eV.[225] In our group, an enthalpy of +3.57 eV and an energy barrier of 2.55 eV was found from DFT+U calculations for the whole process.[226] The endothermicity of the process comes from the instability of O vacancies in zirconia, as seen in the previous sections, which hinders the dehydration step, and from the low reactivity toward H_2. Since it has been seen that the reducibility of zirconia can be enhanced at the nanoscale, we assume that nanostructuring can also have an important effect on the reduction process of zirconia by H_2 adsorption and H_2O desorption. For this, we have investigated the dissociation of the H_2 molecule on the (101) surface and nanoparticles, and the subsequent formation of the $OH_{2,(ads)}$ complex to later desorb $H_2O_{(g)}$ from a thermodynamic and kinetic points of view.

The first part regarding the hydrogenation of zirconia is also motivated by the numerous applications of this oxide in catalytic reactions involving H_2, like the hydrogenation of CO,

[3] The content of this section is published in A. Ruiz Puigdollers, S. Tosoni, G. Pacchioni. Turning a Nonreducible into a Reducible Oxide via Nanostructuring: Opposite Behavior of Bulk ZrO_2 and ZrO_2 Nanoparticles Toward H_2 Adsorption. *J. Phys. Chem. C* 2016, 120, 15329, and A. Ruiz Puigdollers, F. Illas, G. Pacchioni. Reduction of Hydrogenated ZrO_2 Nanoparticles by Water Desorption. *ACS Omega* 2017, 2, 3878.

CO_2,[68] and dienes[70] in organic synthesis, and the conversion of biomasses into fuels.[22,23] Thus, understanding the interaction of zirconia with H_2 is very important to assess its performance in catalysis.

Like other nonreducible oxides, ZrO_2 bulk is known to dissociate H_2 through a heterolytic mechanism in which H^+ ions are stabilized in OH bonds and H^- ions in ZrH bonds, and no reduction of the oxide takes place (no formation of Zr^{3+} ions). Kondo et al. performed FTIR measurements on amorphous ZrO_2 exposed to H_2 and identified the heterolytic dissociation between 223 and 373 K, and the reductive homolytic splitting was possible only heating above room temperatures.[227] Hoffman et al reported from a theoretical study the heterolytic mechanism as more favorable (-0.18 eV) compared to the homolytic one (+0.84 eV).[225] A joint EPR and DFT study reported that the reduction of ZrO_2 by exposure to H_2 could occur at room temperature but under UV irradiation to generate reactive H^0 species.[228] Once formed the H atoms, these can react with the surface or diffuse into the bulk, and act as electron donors, reducing Zr^{4+} sites to Zr^{3+}. This has been confirmed by Muonic spectroscopy.[229] Moreover, the point defects, like O and Zr vacancies, and grain boundaries can stabilize H^- and H^0 species hindering the reduction of Zr sites.[230] Note, however, that these studies refer to the relative stability of H^+, H^- and H^0 species, while the thermodynamic stability of H impurities with respect to the gas-phase H_2 is an aspect that is generally neglected.

Computational details

In this section, Gibbs free energies (G) have also been calculated. For ZrO_2 and ZrO_{2-x}, G is approximated to the PBE+U energy; for $H_{2,(g)}$, $H_2O_{(g)}$, and H_2ZrO_2, they are approximated as the contribution of the zero point energy (ZPE) and entropic terms ($T{\cdot}S$) to the PBE+U energy. Thus, the Gibbs free energy for the hydrogenation and dehydration steps are approximated to

$$G_I = E(H_2ZrO_2) + ZPE_{OH,ZrH} - E(ZrO_2) - 1/2\left(E_{H_2} + ZPE_{H_2} - TS_{H_2}\right) \quad (1)$$

$$G_{II} = E(ZrO_{2-x}) - E(H_2ZrO_2) - ZPE_{OH,ZrH} + E_{H_2O} + ZPE_{H_2O} - TS_{H_2O} \quad (2)$$

In the $G(H_2ZrO_2)$ term, the vibrational internal energy, U_{vib}, and the vibrational entropy, S_{vib}, have been neglected. OH and ZrH vibrations are in the range of 3000-3700 and 1400 cm^{-1}, respectively. With these values, U_{vib} and S_{vib} terms were of the order of 10^{-6} eV only. The entropy of H_2 and H_2O gases was calculated as the sum of translational, S_{trans}, vibrational, S_{vib}, and rotational, S_{rot}, contributions

$$S_{trans} = k_B\left(\frac{5}{2} + \ln q_{trans}\right) \quad (3)$$

$$S_{vib} = k_B \left[\frac{\theta/T}{e^{\theta/T}-1} - \ln\left(1 - e^{-\theta/T}\right) \right] \quad (4)$$

$$S_{rot} = k_B \left[1 + \ln\left(\frac{IT}{\sigma}\right) + \ln\left(\frac{8\pi^2 k_B}{h^2}\right) \right] \quad (5)$$

where q is the partition function, θ the vibrational temperature ($h\nu/k_B$), and I the inertia moment. At 298 K and 1 bar, our calculated entropies for H_2 and H_2O, 131 and 189 $J \cdot mol^{-1} \cdot K^{-1}$, respectively, perfectly agree with those reported in literature.[210]

3.2 Hydrogenation of ZrO_2 Surfaces and Nanoparticles. Role of Nanostructuring

3.2.1 ZrO_2 Bulk

For the adsorption of a H_2 molecule inside the bulk of ZrO_2, only the homolytic type of splitting was possible. The two H^+ ions are bonded to two O_{4c} sites and two Zr^{4+} are reduced to Zr^{3+}, as it can be seen in the spin density plot of Figure 3.13a. The localization of the excess electron is accompanied by a polaronic distortion around the Zr ion. Although the heterolytic splitting (non-reductive) is the preferred mechanism for ZrO_2 surfaces due to its low reducibility, the ZrH^- bond is too long to be stable inside the bulk lattice. The energy cost for the homolytic splitting of H_2 in bulk zirconia is +5.12 eV, Table 3.8, even higher than the dissociation in gas phase (+4.53 eV). This is attributed to the fact that ions in bulk are in their maximum coordination number (Zr_{8c} and O_{4c}), so they are less reactive toward adsorbates. Note that these are simply total energy contributions, and that the entropy effect will make the adsorption of H_2 even more unfavorable.

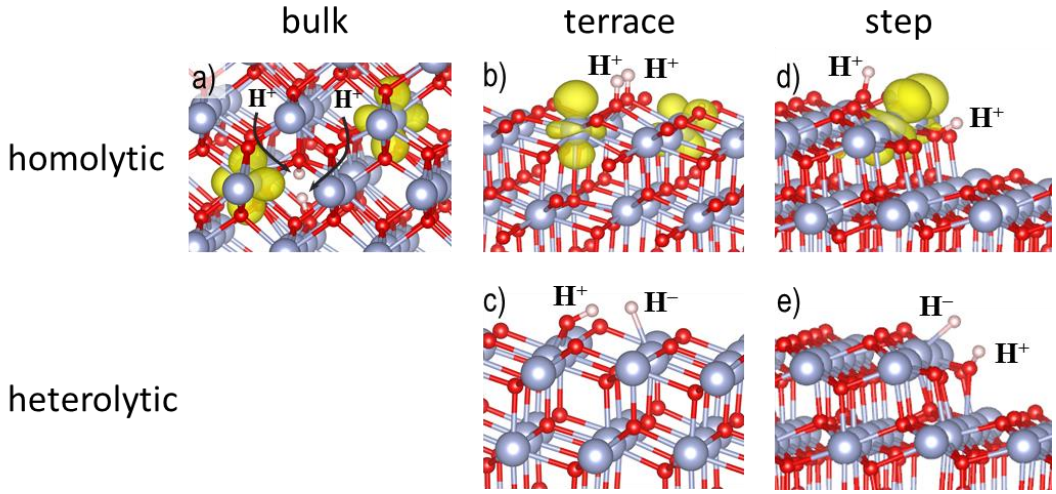

Figure 3.13. Structures of H_2 adsorbed in (a) bulk, (b,c) (101) terrace and (d,e) steps of ZrO_2, through a (top) homolytic and (bottom) heterolytic mechanism. Zr is represented by big blue atoms, O by small red atoms, and H by small white atoms. The spin density is shown in yellow (ρ_{iso} = 0.01 $e^-/Å^3$).

3.2.2 ZrO_2 Surfaces

In the (101) extended surface, the heterolytic mechanism to dissociate H_2, Figure 3.13c, is slightly exothermic, with an energy of -0.06 eV, Table 3.8. We mention that the molecule is dissociated but a residual electrostatic attraction is present, since the H-H distance remains at 2.5Å. The heterolytic is the preferred state for H_2 splitting in which the oxide surface is not reduced. For comparison, the homolytic mechanism, Figure 3.13b, has a cost of +1.69 eV.

We also considered the diffusion of one H atom to a subsurface position. From the heterolytic splitting, the adsorption of the H^+ in the subsurface implies a binding energy 1.73 eV higher than that of the surface heterolytic structure. From the homolytic splitting, moving one H^+ ion to a subsurface position costs +1.80 eV; the H_2 adsorption energy increases to +3.48 eV. Moving the two protons to the subsurface increases the binding energy to +4.42 eV, which is slightly more stable than the two OH^+ groups in bulk (+5.12 eV) due to a better structural relaxation of the top surface. Interestingly, when a proton diffuses from the surface to the bulk, so does the unpaired electron of the surface Zr^{3+} center. In general, the H diffusion into bulk destabilizes the system, so hydrogen is expected to accumulate on the surface at low hydrogen partial pressures.

3.2.3 ZrO_2 Steps

On the stepped (156) surface, while the interactions with both H^+ and H^- ions are stronger compared to the regular (101) surface, the relative stability of the heterolytic and homolytic dissociation is the same. The heterolytic is exothermic by -0.50 eV, and the homolytic is endothermic by +1.12 eV, Table 3.8 and Figures 3.13(d,e). We can conclude that the extended steps may efficiently promote the heterolytic H_2 splitting. However, the oxide is still nonreducible by simple exposure to hydrogen at the extended regime.

Table 3.8. Adsorption energy of H_2 in the bulk and on the (101) terrace and steps of ZrO_2. (*subs*: subsurface site; *surf*: surface site).

	mechanism		$E_{ads,H2}$ (eV)
bulk	homolytic	$2OH^+ + 2e^-$	+5.12
terrace	heterolytic	$OH^+ + ZrH^-$	-0.06
	homolytic	$2OH^+ + 2e^-$	+1.69
	heterolytic	$OH_{subs}^+ + ZrH_{surf}^-$	+1.67
	homolytic	$OH_{subs}^+ + OH_{surf}^+$	+3.48
	homolytic	$OH_{subs}^+ + OH_{subs}^+$	+4.42
step	heterolytic	$OH^+ + ZrH^-$	-0.50
	homolytic	$2OH^+ + 2e^-$	+1.12

Table 3.9. Adsorption energy of H_2 in the inner region and on the surface of ZrO_2 nanoparticles.

	system	mechanism	$E_{ads,H2}$ (eV)
inside	$Zr_{40}O_{80}$	homolytic	+2.19
		heterolytic	+0.01
surface	$Zr_{80}O_{160}$	homolytic	-1.79
		heterolytic	-1.05
	$Zr_{40}O_{80}$	homolytic[a]	-0.71
		heterolytic[a]	-0.69
		heterolytic[b]	-1.80
	$Zr_{16}O_{32}$	homolytic	-1.62
		heterolytic	-0.30

[a]Zr_{4c}-terminated corner. [b]O_{2c}-terminated corner.

3.2.4 ZrO_2 Nanoparticles

A completely different picture is obtained when H_2 is adsorbed and dissociated on the zirconia nanoparticles. Starting with the adsorption of H_2 in the inner sites, it is found that both homolytic and heterolytic mechanism are possible, in contrast to what occurred in bulk ZrO_2 where the heterolytic one was not possible. This is attributed to the higher structural flexibility of the nanoparticles than can accommodate the ZrH^- in the interior. The homolytic splitting is endothermic as in the bulk, with an energy of +2.19 eV, Table 3.9. However, the Zr^{3+} sites are not localized close to the protons but in low coordinated Zr sites in the edges, Figure 3.14a. The heterolytic mechanism is thermoneutral, Figure 3.14b, with a binding energy of +0.01 eV, but still the preferred mechanism like in the extended surface.

On the surface of the nanoparticles, we considered neighboring adsorption sites in the corners, as the low coordination of these sites are expected to have a higher reactivity. Interestingly, both types of splitting are exothermic processes, but the most striking result is that now the reductive homolytic splitting is the thermodynamically preferred mechanism. On the corner sites of $Zr_{80}O_{160}$ and $Zr_{16}O_{32}$, the H_2 splits homolytically with an energy of -1.79 and -1.62 eV, respectively, more stable than the heterolytic ZrH^- and OH^+ structures (-1.05 and -0.30 eV, respectively, Figures 3.14(c,d,h,i)). However, for the $Zr_{40}O_{80}$ nanoparticle, a different picture is obtained. It has been seen, in Figure 3.6, that the electronic structure of this nanoparticle resembles that of the bare (101) surface, as it does not exhibit empty Zr 4d gap states. Then, it is actually a less reducible system than the other nanoparticles. We found that in the Zr_{4c}-terminated corner H_2 dissociates homolytically with an energy of -0.71 and

heterolytically with an energy of -0.69 eV, Figures 3.14(e,f). However, if the molecule is adsorbed in the O_{2c}-terminated corner, the non-reductive heterolytic splitting is more stable with an energy as large as -1.80 eV, Figure 3.14g.

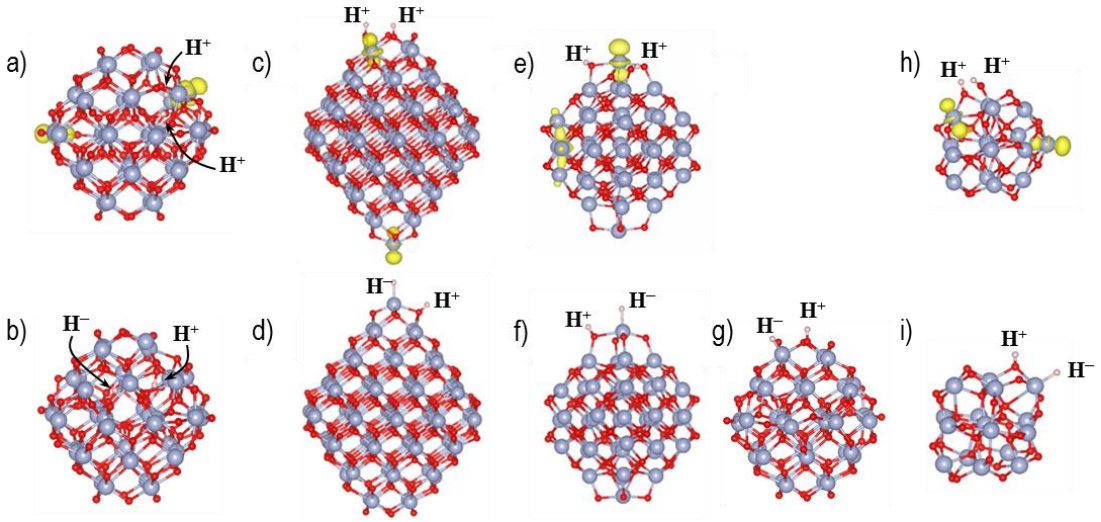

Figure 3.14. Structures of H_2 adsorbed (a,b) on the inner part of $Zr_{40}O_{80}$, and on the corners of (c,d) $Zr_{80}O_{160}$, (e-g) $Zr_{40}O_{80}$, and (h,i) $Zr_{16}O_{32}$, through a (top) homolytic and (bottom) heterolytic mechanisms. Zr is represented by big blue atoms, O by small red atoms, and H by small white atoms. The spin density is shown in yellow (ρ_{iso} = 0.01 $e^-/Å^3$).

Thus, the nanostructuring of the oxide can affect its reactivity in two aspects. The presence of low-lying 4d acceptor gap states, as in the $Zr_{80}O_{160}$ and $Zr_{16}O_{32}$ nanoparticles, can accept the electrons from H_2 and favor the formation of Zr^{3+} sites so the homolytic splitting of the H_2 molecule is favored (electronic effect). Also, the exothermicity is favored by the higher fluxionality displayed by nanoobjects (relaxation effect). In contrast, the exothermicity of the H_2 adsorption on $Zr_{40}O_{80}$ can be only attributed to the relaxation effect.

In short, this shows the importance of the morphology of the nanoparticles rather than the size in affecting the electronic structure, which in turn affects the reactivity. The possibility to localize the extra electrons on undercoordinated Zr sites is the reason for the stabilization of the reductive homolytic splitting in nanoparticles. Then, while bulk ZrO_2 is nonreducible by simply exposure to H_2, nanoparticles with large fraction of undercoordinated sites are, so the importance of the morphology cannot be underestimated in catalytic processes.

3.3 Reduction of Zirconia I. Thermodynamics of Hydrogenation and Dehydration

The first step of the reduction process investigated in this section is hydrogenation. As mentioned above, ZrO_2 bulk and surfaces exhibit a low reactivity toward H_2, with a slightly exothermic binding energy in the (101) surface (-0.06 eV, Table 3.8). However, if we consider the temperature and the entropic terms, it resulted in a positive Gibbs free energy at room conditions –298 K and 1 bar– (+0.34 eV, Table 3.10), as the entropy always hinders the adsorption of gases on surfaces. In contrast, on the nanoparticles, upon inclusion of the entropy and temperature the Gibbs free energy of H_2 dissociation increases (less negative) but still notably exothermic: -1.19, -1.33, and -1.01 eV on $Zr_{80}O_{160}$, $Zr_{40}O_{80}$, and $Zr_{16}O_{32}$, respectively, Table 3.10. Now, we are considering only the most stable dissociations mechanisms for H_2 on the nanoparticles as a starting point for the reduction process, that is, the homolytic solution for $Zr_{80}O_{160}$ and $Zr_{16}O_{32}$, and the heterolytic one for $Zr_{40}O_{80}$. We also report the stretching frequencies of the OH and ZrH bonds needed for the calculation of *G*. It can be seen that the frequencies are significantly blue shifted in the nanoparticles (~3700 cm^{-1}) compared to those on the regular (101) surface (~3000 cm^{-1}). This can be attributed to longer OH and ZrH bonds in the (101) surface due to a larger electrostatic interaction between H^+-H^- ions.

The second step implies the desorption of water from the hydrogenated zirconia surface, with the subsequent formation of an O vacancy (dehydration). This involves the diffusion of a H atom to bind a surface OH group, so the complex O_sH_2 is formed (O_s refers to surface O ion). In the (101) regular surface, this has an energy cost as large as 3.55 eV. In contrast to the previous adsorption process, in the dehydration step the entropic term favors the desorption of the H_2O molecule. The Gibbs free energy, ΔG_{II}, is lowered to +3.28 eV at 298 K and 1 bar, Table 3.10, but still largely endergonic. In the nanoparticles, ΔG_{II} is also endergonic but considerably smaller: +1.55 and +1.56 eV for $Zr_{80}O_{160}$ and $Zr_{16}O_{32}$, respectively, and +2.74 eV for $Zr_{40}O_{80}$. The reduction of the energy costs comes from the stabilization of the O vacancies at the nanoscale. In the (101) surface, the creation of an O vacancy costs around 6 eV with respect to the formation of ½ O_2,[202] while in $Zr_{80}O_{160}$, $Zr_{40}O_{80}$, and $Zr_{16}O_{32}$, the cost is respectively 2.77, 3.82, and 2.96 eV. Note that, again, $Zr_{40}O_{80}$ is the less reactive among the three nanoparticles, but ΔG_{II} is still notably enhanced compared to the extended surface. In general, results show that the creation of an O vacancy in ZrO_2 via desorption of H_2O has a lower cost than via direct desorption of oxygen and formation of ½ O_2. This holds true for both nanoparticles and surfaces.

Table 3.10. Stretching frequencies, $\nu_{X\text{-}H}$ (X = O, Zr), preferred H_2 dissociation mechanism, reaction PBE+U energy, ΔE, and reaction Gibbs free energy at 298 K and 1 bar, ΔG, for steps I and II.

		I – hydrogenation			II – dehydration	
system	$\nu_{X\text{-}H}$ (cm^{-1})	mechanism	ΔE_I (eV)	ΔG_I (eV)	ΔE_{II} (eV)	ΔG_{II} (eV)
(101) surface	OH: 2931, ZrH: 1394	heterolytic	-0.06	+0.34	+3.55	+3.28
$Zr_{80}O_{160}$	OH: 3758, OH: 3755	homolytic	-1.79	-1.19	+2.03	+1.55
$Zr_{40}O_{80}$	OH: 3740, ZrH: 1589	heterolytic	-1.80	-1.33	+3.08	+2.74
$Zr_{16}O_{32}$	OH: 3830, OH: 3785	homolytic	-1.62	-1.01	+2.04	+1.56

Table 3.11. Temperatures in K at which ΔG_I and $\Delta G_{II} < 0$ (spontaneous process) at P = 1 bar (ambient pressure) and = 10^{-12} bar (UHV).

	I – hydrogenation		II – dehydration	
support	$P(H_2)$ = 1 bar	$P(H_2) = 10^{-12}$ bar	$P(H_2O)$ = 1 bar	$P(H_2O) = 10^{-12}$
(101) surface	< 70	< 25	> 1525	> 790
$Zr_{80}O_{160}$	< 930	< 410	> 920	> 450
$Zr_{40}O_{80}$	< 995	< 445	> 1350	> 680
$Zr_{16}O_{32}$	< 840	< 365	> 920	> 450

From the thermodynamic data, we have calculated the reaction conditions at which the Gibbs free energy becomes exergonic, so the process is thermodynamically spontaneous. We have considered the entropy of H_2 and H_2O gases at different temperatures in the range between 50 and 1600 K and for pressures of 1 (ambient) and 10^{-12} bar (ultra-high vacuum, UHV) according to Eqs. 1-5 of this section. Thus, a trend ΔG vs T is constructed for each pressure and reaction step. The temperatures at which $\Delta G = 0$ are reported in Table 3.11. At ambient pressure, the (101) surface can split the H_2 molecule only below 70 K, due to the low reactivity of the extended zirconia toward hydrogen (for higher temperatures H_2 desorption dominates). On the contrary, nanoparticles can be hydrogenated at ambient pressure at temperatures up to 800 – 900 K.

The desorption of H_2O from the hydrogenated zirconia (101) surface at ambient pressure (1 bar) is possible above 1500 K, due to the high endergonic character of the process (ΔG_{II} = +3.28, Table 3.10), or above 800 K if the partial pressure of H_2O is decreased to UHV conditions (10^{-12} bar). Like in the previous hydrogenation step, nanoparticles can undergo dehydration at milder conditions compared to the (101) surface. H_2O can start desorbing from the nanoparticles and creating an O vacancy at already above 450 K, a temperature at which several catalytic processes involving oxides start to occur.[23] In summary, zirconia

nanoparticles can dissociate H_2 and desorb H_2O at milder reaction conditions compared to the extended surface, changing completely the landscape for the chemistry of these oxide.

3.4 Reduction of Zirconia II. Kinetic Aspects

In this section, we investigate the complete energy path including the reaction barriers for the formation of the surface O_sH_2 group. First, on the (101) zirconia surface, the H_2 molecule is physisorbed with an energy of -0.11 eV. It is dissociated into H^+ and H^- species (heterolytic splitting) through a small energy barrier of 0.28 eV, and a small binding energy of -0.06 eV (see above). Experimentally, such barrier has been estimated to be around 0.4 eV.[227] In order to form the O_sH_2 complex, which is equivalent to a H_2O molecule adsorbed on an O vacancy, the H^- ion must diffuse to the OH^+ group. This process forces the system to become reduced. In fact, when the H atoms are bound to the same oxygen, the excess of charge is localized on two Zr^{3+} centers in a triplet state, as seen by the spin density plot in Figure 3.15. This was actually a highly unfavorable state in the (101) surface, so it is non-competitive with respect to H_2 desorption (reverse reaction). However, it is still a necessary step for the final H_2O desorption. In fact, the formation of the O_sH_2 complex is highly endothermic with an energy cost of 2.79 eV, and the energy barrier was calculated to be 2.93 eV. Once the surface O_sH_2 complex is formed, water desorbs to the gas phase with an energy cost of 0.72 eV. Therefore, the highest barrier in the entire process is the diffusion of a H atom to form the O_sH_2 precursor state of the desorbing water molecule. Neglecting prefactors, this is the rate determining state with a very high energy barrier. So, this process is expected to hardly occur on the bare zirconia surface as H_2 desorption is clearly preferred.

On zirconia nanoparticles, lower barriers were expected for the dehydration process. In Figure 3.16, the reaction energy profiles on the nanoparticles are compared to that on the (101) surface. We did not consider the first H_2 dissociation barrier from a physisorbed state since this tends to be small compared to the H_2 adsorption energies on nanoparticles (-1.6 – -1.8 eV), so small changes in H_2 physisorption and dissociation barrier are not expected to play a role in the whole process. On the nanoparticles, one H atom diffuses from the OH or ZrH group to the other OH group. Also in this case, the overall nanoparticle-O_sH_2 complex assumes a triplet ground state with two localized Zr^{3+} sites, Figure 3.15. Interestingly, the energy barrier decreases to 1.77 eV in $Zr_{80}O_{160}$ and 1.83 eV in $Zr_{16}O_{32}$. This is a very significant reduction of more than 1 eV. Consequently, the H diffusion competes with the H_2 desorption, differently from the bare (101) surface. The subsequent desorption of H_2O has a cost of 0.85 eV in

$Zr_{80}O_{16}0$ and 1.11 eV in $Zr_{16}O_{32}$. Thus, also on the nanoparticles the rate determining step is the formation of the O_sH_2 surface complex. However, despite the large decrease in the barrier, this does not reach the low value found for TiO_2, a reducible oxide, where the barrier for a similar process has been estimated around 0.3 eV.[224]

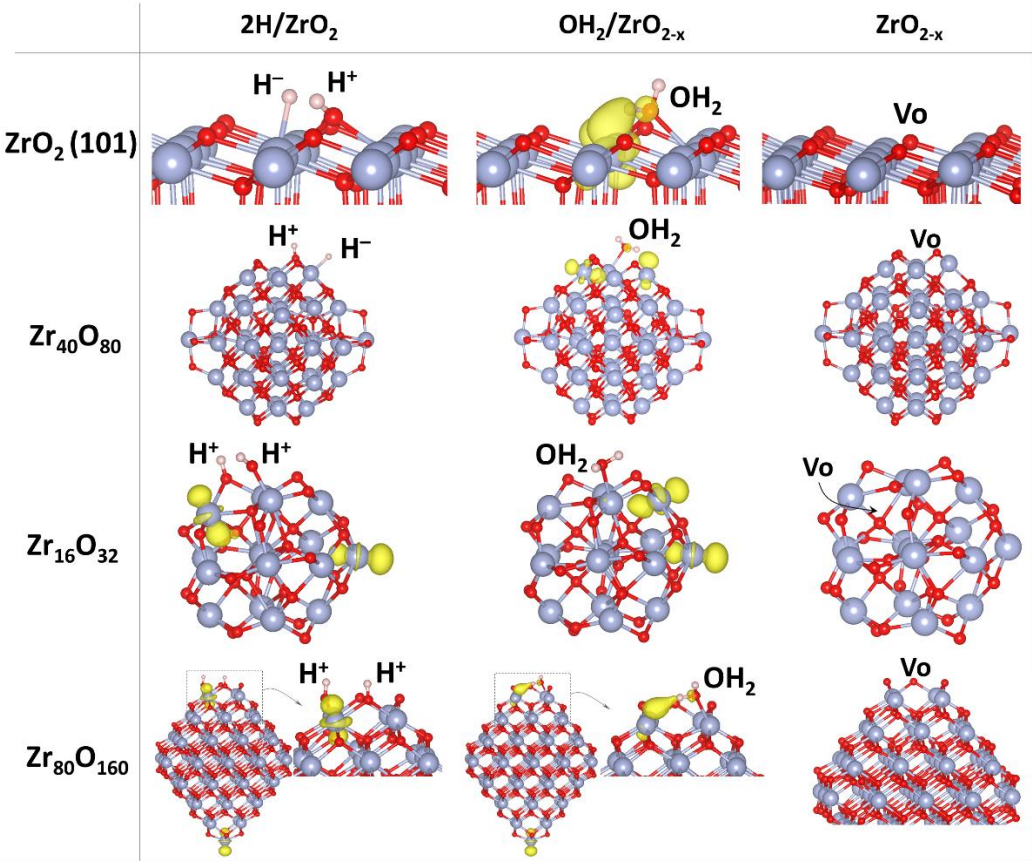

Figure 3.15. Structures for the dehydration process from the heterolytically hydrogenated ZrO_2 (101) surface and $Zr_{40}O_{80}$, and the homolytically hydrogenated $Zr_{16}O_{32}$ and $Zr_{80}O_{160}$ nanoparticles. Zr is represented by big blue atoms, O by small red atoms, and H by small white atoms. The spin density is indicated in yellow (ρ_{iso} = 0.01 $e^-/Å^3$).

For the $Zr_{40}O_{80}$ nanoparticle, thins are slightly different. As it has been seen, the thermodynamics for the reduction reaction is similar to the (101) surface. Accordingly, its reaction energy path has some resemblance with that of the surface. The energy cost to form the O_sH_2 precursor is lower, 2.24 eV, due to a higher structural flexibility, and also the energy barrier, 2.27 eV. From this state, H_2O desorbs with an energy consumption of 0.84 eV. Thus, the barrier is also enhanced with respect to the (101) surface, but still larger than on the other two ZrO_2 nanoparticles.

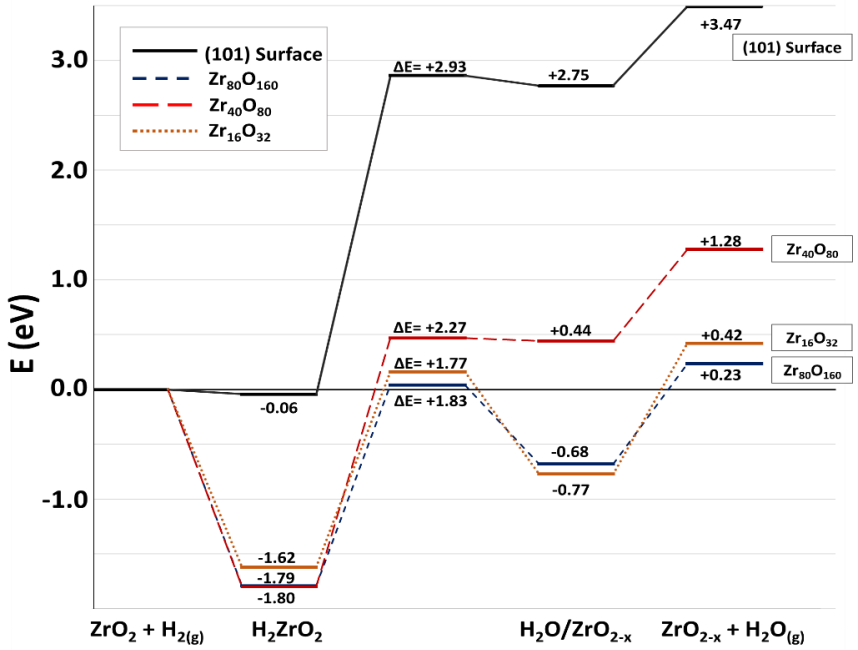

Figure 3.16. Reaction energy profiles for the reduction of the zirconia (solid line) (101) surface and (dashed lines) nanoparticles by hydrogenation and water desorption.

These results show the positive effect of nanostructuring on the reducibility of ZrO_2 by water removal. The special fluxionality of the nanostructures contributes not only at lowering the energy costs but also the energy barriers, favored by a larger structural relaxation around the O vacancy. However, by comparing the three nanoparticles, one can conclude that the key factor is the presence of low lying acceptor states introduced in the gap by low coordinated Zr sites in corners and edges, which strongly depends on the morphology of the nanoparticle.

Table 3.11. Diffusion energy, ΔE_{diff}, and energy barrier, $\Delta E^{\ddagger}$, for the diffusion of a H atom to adsorption sites distant from the OH^+ precursor of the H_2O formation.

support		ΔE_{diff} (eV)	$\Delta E^{\ddagger}$ (eV)
(101) surface	OH^+ to O’	0.64	1.50
	ZrH^- to Zr’	0.73	1.42
$Zr_{80}O_{160}$	$O_{2c}H^+$ to O_{3c}	0.69	1.73
$Zr_{40}O_{80}$	$O_{2c}H^+$ to O_{3c}	0.84	1.58
	ZrH^- to Zr_{facet}	0.24	2.15
$Zr_{16}O_{32}$	$O_{2c}H^+$ to O_{2c}	0.06	1.72
	$O_{2c}H^+$ to O_{3c}	0.50	1.54

Finally, we also considered the diffusion of one H atom along the surfaces to sites far from the other H atom. Then, this supposes diffusion paths that hinder the formation of the O_sH_2

precursor as the H atoms are being separated. On the (101) surface, the displacement of H^+ and H^- ions to more distant O and Zr sites, respectively, has an energy cost of 0.64 eV and 0.73 eV, and it implies to overcome a barrier of 1.50 (H^+) and 1.42 (H^-) eV, Table 3.11. The relatively high cost is due to the separation of opposite charges. The barrier is sufficiently high that, at low H_2 pressure, molecular desorption rather than diffusion is expected. This means that the formation of the O_sH_2 complex is a rather unlikely event on the bare (101) zirconia surface. In $Zr_{80}O_{160}$ and $Zr_{16}O_{32}$, the diffusion of H^+ to facet O sites costs 0.69 and 0.50 eV, respectively. Despite that two positive charges are being separated, the proton goes from a O_{2c} corner site to a less reactive O_{3c} site in the facet, with the concomitant decrease in stability. In fact, the H^+ diffusion between two O_{2c} in $Zr_{16}O_{32}$ costs 0.06 eV only. On $Zr_{40}O_{80}$, the diffusion of H^+ and H^- cost 0.84 and 0.24 eV, respectively, for the same reasons explained. The energy barriers for diffusion on nanoparticles are of the order of 1.5 – 2 eV, which are not very different from those on the extended surface (1.50 and 1.42 eV). However, on the nanoparticles this barrier is comparable to that required to form the surface O_sH_2 precursor, suggesting that here the hydrogen diffusion and formation of water become actually competitive processes.

4 Magnetic Properties of Reduced ZrO_2 Nanoparticles

4.1 Introduction

Long research has been dedicated to the study of ferromagnetism induced by doping semiconductors like ZnO,[231] TiO_2,[232] and ZrO_2[233] with transition metal atoms. These are also called diluted magnetic semiconductors (DMS). Provide semiconductors of ferromagnetism has been applied in spintronics and optoelectronics.[234] However, it is not clear whether ferromagnetism in semiconductors is a property of the metal dopants or it is an intrinsic property of the system, as oxides doped with light 2p elements have also been predicted as ferromagnets at room temperature, like C- and N-ZnO,[235,236] C- and N-TiO_2,[237,238] and N-ZrO_2.[239] Then, the origin of the magnetic behavior is still an open question. In addition, undoped thin films of TiO_2, ZnO, In_2O_3, HfO_2, and ZrO_2 exhibit ferromagnetism at room temperature, which has been suggested to be related to intrinsic defects. In thin films, however, the nature of the interface with the support is a critical issue.

Oxide nanoparticles and nanostructures are then ideal systems to obtain ferromagnets at room temperature, as doping and interface issues are not present. Recently, a ferromagnetic behavior has been reported for zirconia nanoparticles.[240] It has been attributed to the presence of surface oxygen vacancies. However, the excess electrons associated to vacancies in zirconia surfaces are trapped in the cavity in a diamagnetic ground state. Instead, it has been seen that in the nanoparticles the Zr^{3+} centers are easier to form in low-coordinated Zr ions as their d states are stabilized with respect to the CB. The conditions at which Zr^{3+} centers lead to a ferromagnetic ordering, like the size of the nanoparticles and the level of defectivity, are new open questions. Then, we investigated the magnetic states of reduced ZrO_{2-x} nanoparticles with increasing size and level of oxygen deficiency, in order to answer these questions.

In order to exhibit a ferromagnetic behavior at room temperature, the extent of the effective pair exchange interaction, $J = E_{FM} - E_{AFM}$, in reduced nanoparticles is such that the Curie temperature for the transition from the ferromagnetic to the antiferromagnetic states is above room temperature.

Computational Details

For the reduced zirconia models, we have employed the octahedral-type of nanoparticles described in section §3.1.2. We considered the stoichiometries $Zr_{44}O_{80}$, $Zr_{85}O_{160}$, $Zr_{146}O_{280}$, and $Zr_{231}O_{448}$, containing 8, 10, 12, and 14 O vacancies, respectively. The sizes range from 1.4 to 3.0 nm, the same as synthesized octahedral-based zirconia nanoparticles.[204] The energetics of

the singlet and high spin states of $Zr_{44}O_{80}$, $Zr_{85}O_{160}$, $Zr_{146}O_{280}$ nanoparticles has been studied at the PBE+U level of theory. The calculation of the *J* values has been performed with the PBE0 hybrid functional using the CRYSTAL14 code, by Dr. Elisa Albanese from our group. In contrast to VASP, this code uses linear combinations of Blöch functions for the crystalline orbitals, which are built from linear combinations of Gaussian-type orbitals. This basis set permits a better description of localized electrons and their exchange interaction.

The Curie temperature has been calculated using the mean field theory. In this theory, the system of N interacting spins is reduced to one spin *i* interacting with an effective magnetic field, H_{eff}, which is the sum of the external magnetic field (*H*) and the internal field generated by all neighboring spins, s_j

$$H_{eff} = J\sum_{j=1}^{q} s_j + H \tag{6}$$

The sum over *j* is over the *q* nearest neighbors of the spin *i*. The orientation of the neighboring spins depends on the orientation of *i*, so H_{eff} fluctuates around its mean values. Here, we assume orientation independence, and the field at *i* is the mean value, $\bar{H}_{\text{eff}}$

$$\bar{H}_{eff} = J\sum_{j=1}^{q} \bar{s}_j + H = Jqm + H \tag{7}$$

where $\bar{s}_j$ is the magnetization, *m*. The partition function for one spin is

$$Z_1 = \sum_{s_1=\pm 1} e^{s_1 \bar{H}_{eff}/kT} = 2\cosh[(Jqm + H)/kt] \tag{8}$$

and the free energy per spin is

$$F = -kT \ln Z_1 = -kT \ln 2\cosh[(Jqm + H)/kT] \tag{9}$$

The magnetization can then be written as

$$m = -\frac{\partial F}{\partial H} = \tanh[(Jqm + H)/kt] \tag{10}$$

Without external magnetic field, $H = 0$, non-zero solutions exist for m when $Jqm/kT \geq 1$. The Curie temperature, T_c, satisfies that $m \neq 0$ for $T \leq T_c$ and $m = 0$ for $T > T_c$. Thus, the critical temperature is given by

$$kT_C = Jq \tag{11}$$

4.2 Non-Magnetic Vs Magnetic Ground State of ZrO_{2-x} Nanoparticles

The $Zr_{44}O_{80}$ nanoparticle shows a singlet closed shell ground state. In this configuration, from the total of 16 excess electrons from the 8 O vacancies, formally 12 of them are localized on the d_{z2} orbital of the six Zr_{4c} corner atoms, which are reduced to Zr^{2+} ($4d^2$) ions. This is due to the stabilization of the stabilization of the 4d states of the Zr corners with respect to the CB (formed by fully coordinated ions). In particular, they appear around 1 eV below the CB. The remaining excess of charge is distributed inside the nanoparticle, Figure 3.17d. The high spin configuration lies 1.69 eV higher in energy, Table 3.12. Here, the excess electrons are distributed on the low-coordinated Zr ions at corners and edges, which are reduced to Zr^{3+} ($4d^1$). This small number of Zr_{6c} sites along the edges of this nanoparticle, which is only 2 per edge, implies a dense distribution of the unpaired electrons, leading to a higher repulsion and higher cost for the polaronic distortion around the Zr^{3+} center, Figure 3.17a. This causes the low stability of the high spin state.

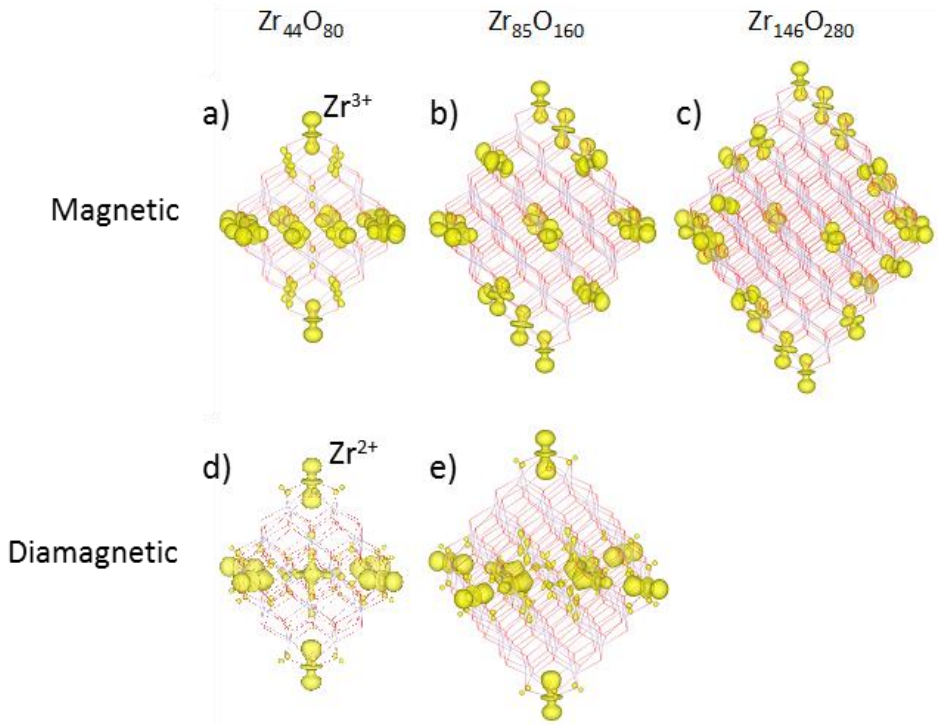

Figure 3.17 a) Spin density plot of the three ZrO_{2-x} nanoparticles in the high-spin configuration. The presence of spin density is indicating an unpaired electron on Zr^{3+} sites ($4d^1$). b) Density plot projected on the defective gap states of the three ZrO_{2-x} nanoparticles in the singlet closed shell configuration. The presence of density is indicating two paired electrons on a Zr^{2+} site ($4d^2$). ρ_{iso} = 0.01 e/Å^3.

Table 3.12 Number of excess electrons, n_e, of Zr_{4c} and Zr_{6c} sites, and relative energies of the singlet, E_S, and high spin, E_{HS}, configurations.

system	n_e	Zr_{4c}	Zr_{6c}	E_S (eV)	E_{HS} (eV)
$Zr_{44}O_{80}$	16	6	24	0	+1.69
$Zr_{85}O_{160}$	20	6	36	+0.86	0
$Zr_{146}O_{280}$	24	6	48	unstable	0

Increasing the size of the nanoparticle, the relative stability of the singlet and high spin states changes. The ground state of the $Zr_{85}O_{160}$ is the high spin configuration, and the singlet closed shell solution lies 0.86 eV higher in energy, Table 3.12. The distribution of the 20 unpaired electrons (from 10 O vacancies) is similar as in $Zr_{44}O_{80}$. However, in this case, the Zr^{3+} sites can be more uniformly distributed along edges and corners as now this nanoparticle contains 3 Zr_{6c} sites per edge or 36 in total, Figure 3.17b. Similarly, the $Zr_{146}O_{280}$ nanoparticle has 4 Zr_{6c} per edge or 48 in total, and in this case only the high spin configuration was found to be stable, Figure 3.17c. Thus, these results suggest that the switch from diamagnetic to magnetic ground state depends on the ratio between the number of excess electrons and the number of low-coordinated sites available. A sufficiently high number of these sites, $Zr_{LC} >> n_e$, favors the single occupancy of the Zr 4d states, as the unpaired electrons of Zr^{3+} sites are better distributed. We can conclude that O-deficient zirconia nanoparticles are magnetic in the ground state, in contrast to bulk zirconia. Thus, the spontaneous magnetization at the nanoscale is an intrinsic property of reduced zirconia.

4.3 Magnetic Ordering in ZrO_{2-x} Nanoparticles

To confirm the existence of ferromagnetism at room temperature in reduced nanoparticles we have computed the exchange coupling J_{ij} of magnetic Zr^{3+} sites. It requires to compare the stabilities of ferromagnetic and antiferromagnetic configurations. To this aim, we have considered two different approaches. (1) We calculated the J_{ij} value for an isolated pair of unpaired electrons in the stoichiometric $Zr_{40}O_{80}$ nanoparticle where one O atom has been removed ($Zr_{40}O_{79}$), and then we used this value to approximate the total J of larger nanoparticles. (2) Then, we calculated it for the $Zr_{146}O_{280}$ and $Zr_{231}O_{448}$ nanoparticles with 12 and 14 O vacancies.

In $Zr_{40}O_{79}$, the two electrons of the vacancy can give a triplet open shell (FM), a singlet open shell (AFM), or a singlet closed shell (S) configurations. In the open shell solutions, one of the electrons is localized in a Zr^{3+} site in the corner and the other in the vacancy, Figure

3.18. The AFM configuration lies 1 meV higher in energy than the FM, so J_{ij} = 1 meV. We also tested other FM and AFM configurations in $Zr_{40}O_{79}$ with different geometries and always a preference for the FM coupling was obtained.

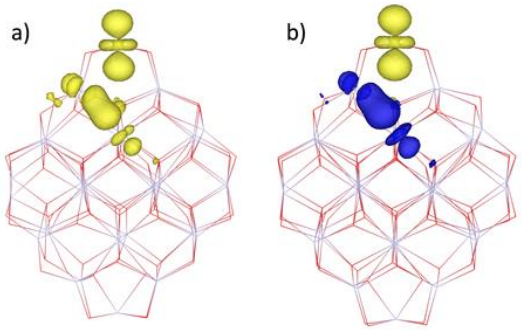

Figure 3.18 Spin density plot of high spin (a) ferromagnetic and (b) antiferromagnetic configurations of $Zr_{40}O_{79}$. Yellow represents spin up electrons, and blue spin down electrons. ρ_{iso} = 0.008 e/Å^3.

Once determined J_{ij} for the isolated electron pair, we then estimated the exchange coupling for larger nanoparticles using this approximated method. The magnetic interaction of several unpaired electrons, *J*, can be written as the sum of interaction pairs, neglecting three-body interaction term and higher

$$J = \frac{1}{2}\sum_{i\neq j}^{n_e} J_{ij} \qquad (12)$$

In this approximation, *J* depends directly on the number of excess electrons, n_e.

Table 3.13 Energy differences between the antiferromagnetic and ferromagnetic configurations, *J*, calculated as the sum of isolated interacting pairs (Eq. 12), and as the direct difference of the optimized AFM and FM solutions.

system	*J* (meV), Eq. 12	$E_{AFM} - E_{FM}$ (meV)
$Zr_{40}O_{79}$	+1.0	+1.0
$Zr_{146}O_{280}$	+11.9	+13.3
$Zr_{231}O_{448}$	+13.9	+30.4

Considering the $Zr_{146}O_{280}$ and $Zr_{231}O_{448}$ nanoparticles that have 12 and 14 pairs of electrons (from 12 and 14 O vacancies), respectively, we obtained exchange couplings of 11.9 and 13.9 meV, respectively. Then, the number of O vacancies and the strength of the FM interaction is correlated, as has been experimentally suggested.[240]

Then, to verify these results, we calculated the AFM configuration for $Zr_{146}O_{280}$ and $Zr_{231}O_{448}$ nanoparticles, starting from the optimal FM geometry and fully relaxing the structure, Figure 3.19. Of course, several possible AFM solutions exist, and we did not

consider all of them. In $Zr_{146}O_{280}$, the cost to flip the spin of 12 electrons, going from 24 up electrons (FM) to 12 up and 12 down electrons (AFM), is 13.3 meV, Table 3.13, confirming again the preference for the FM configuration. In the $Zr_{231}O_{448}$ nanoparticle, the flip costs as large as 30.4 meV. Note that this value is notably larger than that obtained by the simplified model of isolated electron pairs. Therefore, this shows the limit of the simple model to provide a quantitative estimate of the total *J* of the nanoparticle. However, both confirm the trend that higher number of O vacancies leads to a more stable FM interaction.

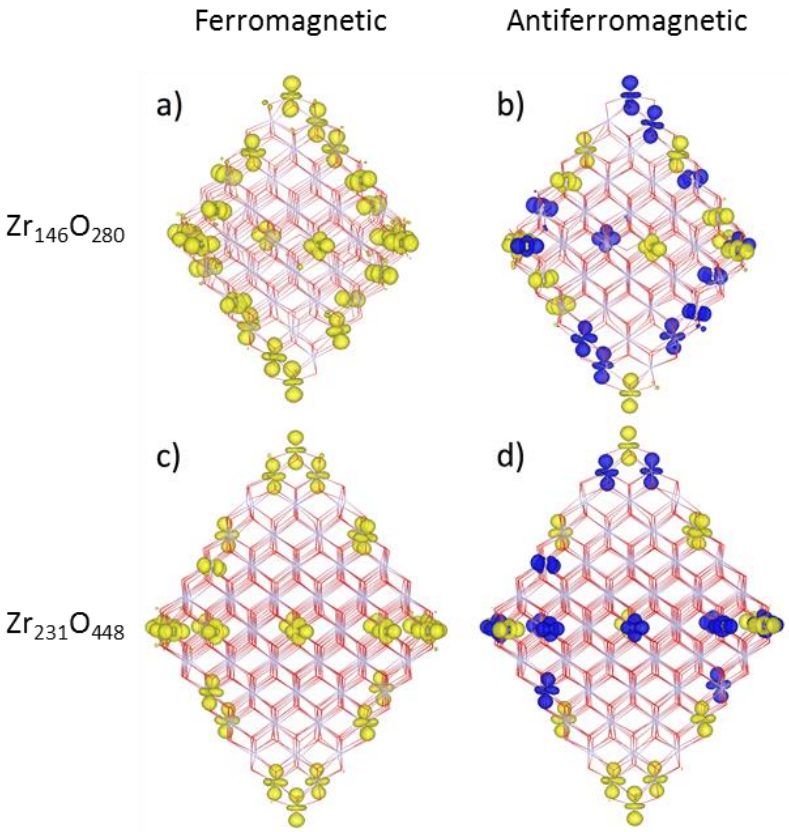

Figure 3.19 Spin density plot of high spin (a,c) ferromagnetic (FM) and (b,d) antiferromagnetic (AFM) configurations of (a,b) $Zr_{146}O_{280}$ and (c,d) $Zr_{231}O_{448}$. Yellow represents spin up electrons, and blue spin down electrons. ρ_{iso} = 0.01 e/Å^3.

The origin of ferromagnetism has been explained via the bound magnetic polaron (BMP) theory. This has been proposed for transition metal dopants, and implies an exchange interaction between shallow states associated to defects with the localized d electrons of dopants. However, it has been reformulated by taking into account only the O vacancies as responsible for ferromagnetism in undoped TiO_2 nanoribbons.[241] Here, once the vacancies

concentration reaches a certain limit, the overlap between bound magnetic polarons favors the FM ordering. On the other hand, this model does not explain the absence of ferromagnetism in O deficient HfO_2 and ZrO_2 thin films. Another model proposed was the charge transfer FM (CTF) model. Defects introduce an impurity band below the CB. Vacancies act as a charge reservoir that facilitates the hopping of electrons between the impurity and conduction bands leading to the splitting of spin states providing a FM behavior.

Here, we propose a model that mixes the BMP and CTF theories. A bound magnetic polaron is formed between two nearby Zr^{3+} sites. The Zr $4d^1$ states form a band just below the CB. At higher concentration of O vacancies, these defect states can merge with the CB leading to a splitting of the up and down spin states, which favors the FM ordering. The charge reservoir is represented by the electrons in Zr^{3+}. Then, the stability of the FM configuration depends on the hybridization degree between the impurity and conduction bands.

Finally, in order to answer whether reduced zirconia nanoparticles are FM at room temperature, we calculated the Curie temperature (T_c) using the mean field approximation described previously. According to Eq. 11 and considering the nanoparticle J value computed as the sum of independent J_{ij} (Eq. 12 with $q = 2$), the T_c estimated is 280 K for $Zr_{146}O_{280}$ and 324 K for $Zr_{231}O_{448}$, Table 3.14. Then, increasing the O deficiency, also the total magnetization and T_c increase.

Considering the J value obtained from the direct difference between AFM and FM energies in $Zr_{146}O_{280}$ and $Zr_{231}O_{448}$, we obtained T_c = 259 K for $Zr_{146}O_{280}$ and 387 K for $Zr_{231}O_{448}$. In this case, we considered $q = 1$ of Eq. 11 as all possible interactions are considered. Then, the two different approaches give not too different T_c values. However, it has to be taken into account that the mean field approximation tends to overestimate the T_c.[242] These results suggest that it is theoretically predicted that reduced ZrO_{2-x} nanoparticles of around 3 nm can exhibit a FM behavior at room temperature, as observed experimentally.

Table 3.14 Curie temperatures, T_c, calculated with the exchange coupling J obtained as the sum of isolated interacting pairs (Eq. 12), or as the direct difference between AFM and FM solutions.

system	T_C (K), J from Eq. 12	T_C (K), J from $E_{AFM} - E_{FM}$
$Zr_{146}O_{280}$	278	259
$Zr_{231}O_{448}$	324	355

Chapter Summary

To investigate the effect of nanostructuring on ZrO_2, we have designed a set of different octahedral-based models of t-ZrO_2 nanoparticles in the 0.9 – 1.9 nm range of size. They have been constructed by cutting the bulk of the tetragonal phase along the {101} and {001} surfaces as these are the two most stable for this phase (Wulff construction). The relative stability of the exposed facets was not large enough to predict the stability of a given morphology. The electronic structure of the current stoichiometry plays a fundamental role. In particular, stoichiometric nanoparticles –$Zr_{16}O_{32}$, $Zr_{40}O_{80}$, and $Zr_{80}O_{160}$– are the most stable, although those oxygen deficient –$Zr_{19}O_{32}$, $Zr_{44}O_{80}$, and $Zr_{85}O_{160}$– exhibit the most stable (101) surface in all facets.

Low coordinated sites in stoichiometric nanoparticles introduce defective gap states in the electronic structure, coming from the destabilization of O 2p states with respect to the VB (possible donors) and the stabilization of Zr 4d states with respect to the CB (possible acceptors). Thus, these sites are expected to be more reactive toward adsorbates, as well as to enhance the photocatalytic activity by modification of the transition energies.

The improved reactivity of nanostructured zirconia compared to bulk has been investigated by means of three different processes: (1) the formation of oxygen vacancies, (2) the adsorption of a Au atom and a AuCO complex, and (3) its reduction by hydrogenation and water desorption.

Oxygen vacancies are found to be notably more stable in the nanoparticles than in bulk ZrO_2. The calculated formation energies decrease from around 6 eV in bulk and surfaces to around 2.5 – 3 eV in the corners and edges of the nanoparticles. Thus, nanostructuring improves the chemical activity of zirconia in reactions where the transfer of oxygen is involved.

While on the ZrO_2 (101) surface Au is adsorbed with an energy of -0.90 eV and remains neutral, on the stoichiometric ZrO_2 nanoparticles it adsorbs with energies around -2.6 – -2.8 eV with the occurrence of a charge transfer. Au^+ or Au^- species are formed depending on the adsorption site (O or Zr sites, respectively). This is due to the undercoordination of sites and the defective gap states that act as electron donors or acceptors. The special electronic structure of nanoparticles was also observed by the changes in the CO stretching frequency when the AuCO complex was adsorbed on the (101) surface and on the nanoparticles. CO destabilizes the Au $6s^1$ electron. In the absence of acceptor gap states like in the (101) surface, the $6s^1$

electron is transferred to the CO 2π* states with the subsequent strong red-shift in the frequency (from 2127 cm-1 to around 1950 cm-1). However, nanoparticles are reduced by the Au $6s^1$ electron instead of the CO group, not resulting in the strong-red shift. This is the same behavior observed in the adsorption of AuCO on a reducible oxide like TiO_2.[221]

Finally, we have investigated the reduction process of ZrO_2 by hydrogenation and water desorption ($ZrO_2 + H_2 \rightarrow ZrO_{2-x} + H_2O$). First, the dissociation of the H_2 molecule is much more exothermic on the nanoparticles (-1.6 – -1.8 eV) than on the (101) surface (-0.06 eV). Moreover, while on the surface H_2 dissociates through a heterolytic mechanism, in which the oxide is not reduced, on the nanoparticles it is expected to occur through a homolytic mechanism due to the presence of the acceptor gap states, in which two H^+ species and two reduced Zr^{3+} sites are formed. Then, the dehydration process is found to be less endothermic in the nanoparticles due to a higher stabilization of the O_sH_2 complex. In general, the endothermicity of the whole process is reduced by around 2 eV. These results show thus that the O vacancy formation via H_2O desorption is more convenient than via direct O_2 desorption.

From the calculated ΔG vs T trend of both the hydrogenation and dehydration steps, we concluded that nanoparticles can be hydrogenated spontaneously at room pressure and up to 800-900 K, while on the surface T must be decreased below 70K. Then, hydrogenated nanoparticles can desorb H_2O in UHV conditions already above 450 K, while the extended surface requires 800 K. Regarding the kinetics of the process, we calculated an energy barrier to form the adsorbed O_sH_2 complex 1 – 1.2 eV lower on the nanoparticles than on the surface.

Bulk ZrO_2 is non-magnetic. However, we have also shown that the sufficient presence of low-coordinated Zr ions in reduced ZrO_{2-x} nanoparticles favors the localization of the excess electrons in Zr^{3+} ($4d^1$) states in a ferromagnetic ordering. The absence of sifficient undercoordinated sites leads to a double occupation of the 4d levels. Zr^{2+} ($4d^2$) sites are formed resulting in a diamagnetic ground state. Increasing the number of O vacancies leads to a stronger exchange coupling and higher Curie temperatures: 259 K for $Zr_{146}O_{280}$ and 387 K for $Zr_{231}O_{448}$, nanoparticles with 12 and 14 O vacancies, respectively, resulting in ferromagnetic materials at room temperature.

In general, this chapter show the importance of nanostructuring for the chemistry and catalytic activity of ZrO_2, as it significantly modifies the oxide reducibility. This phenomenon cannot be underestimated in catalysis since it provides a modified electronic interaction with deposited metals as well as a better activity in reactions where O atoms are transferred.

Chapter 4

Metal-Oxide Interface: Supported Metal Clusters

1 Role of Dispersion Forces on Supported Au_n and Ag_n Clusters[4]

1.1 Introduction

The deposition of transition-metal particles with nano- and subnanometer sizes on various oxides is a topic of enormous interest for the investigation of diffusion mechanisms, nucleation, growth, and stabilization of supported metals.[13,91,143] For instance, oxide supported gold and silver clusters are widely used as active catalysts for a large variety of reactions, like the CO oxidation reaction,[163,243] propylene oxidation,[244] and the water gas shift reaction.[218] The possibility of growing, characterization and application of metal clusters or nanoparticles is at the basis of nanocatalysis.

The bonding properties of a metal cluster on an oxide surface depend on a large number of factors, like the surface termination, the presence of defects, the nature of the deposited metal, and the preparation conditions (see §1.4). Theoretical investigations are then needed to support the experimental data. The characterization of the metal-oxide interaction is central in determining the reaction mechanisms and catalytic properties. However, the theoretical description of the interface is not free from limitations. This is largely based on the use of DFT, an approach that has produced several successful results. However, only in the past years has been recognized that dispersion forces, which have long been considered negligible in these problems, really play an important role. Thus, in this section, we investigate how the van

[4] This content has been published in A. Ruiz Puigdollers, P. Schlexer, G. Pacchioni. Gold and Silver Clusters on TiO_2 and ZrO_2 (101) Surfaces: Role of Dispersion Forces. *J. Phys. Chem. C* 2015, 119, 15381.

der Waals (vdW) forces affects the structure, electronic, and bonding properties of Au and Ag atoms and tetramers deposited on the (101) surface of t-ZrO_2.

Computational details

The role of the vdW forces was investigated by considering different computational approaches to account for them. We used the modified PBE+D2'[199] already described in §2.6, and the standard PBE+D2 implemented by Grimme.[185] Also, a third method proposed by Lundqvist et al. was used, in which the long-range correlation effects responsible for dispersion forces are taken into account already in the calculation of the electron density, named vdW-DF. In particular, we used the optB86b-vdW density functional.[245]

As in this section we aim at determining the structure and bonding properties of neutral Au and Ag clusters supported on ZrO_2, we checked the effect of the dispersion interactions on the cohesive energy and the lattice parameters of these metals, Table 4.1. This test showed that the cohesive energies of the metals were underestimated at the PBE level and that introducing the D2 correction produced a clear improvement. Also, the changes in the lattice structure, measured as cell volume, were less than 1%. In contrast, the vdW-DF functional slightly improved the cohesive energy but also resulted in too large lattice constants.

Table 4.1. Cohesive energies, E_c, and lattice parameters, a, of Au and Ag metals computed with different approaches to account for vdW forces.

	expt[210]		PBE		PBE+D2		vdW-DF	
	E_c (eV)	a (Å)	E_c (eV)	a (Å)	E_c (eV)	a (Å)	E_c (eV)	a (Å)
Au	3.78	4.08	3.04	4.15	3.51	4.10	3.27	4.21
Ag	2.95	4.09	2.51	4.13	3.07	4.11	2.70	4.18

1.2 Au and Ag Atom Adsorption on the ZrO_2 (101) Surface

First, we considered the adsorption of one single Au or Ag atom on the (101) surface of zirconia without the inclusion of the dispersion forces in the calculation. For both Au and Ag atoms, the most stable adsorption site is a bridge position between Zr and O sites, Figure 4.1a, with binding energies of -0.90 and -0.34 eV for Au and Ag atoms, respectively, Table 4.2. The same adsorption site preference was found for Au and Ag atoms in a (111) surface model of cubic ZrO_2,[246] which is equivalent to the (101) surface of the tetragonal phase. A less stable binding site was found in a hollow position between Zr-O-Zr ions, Figure 4.1b. Here, Au was adsorbed with an energy of -0.69 eV, and Ag with an energy of -0.28 eV.

Both Au and Ag retain the $6s^1$ and $5s^1$ atom-like configuration, respectively, which excludes the occurrence of charge transfer at the interface. It can be appreciated in the PDOS, Figure 4.2. Also, the Bader charge localized on Au and Ag atoms are virtually zero, Table 4.2. So, the interaction between metal atoms and ZrO_2 is mainly due to polarization effects and covalent mixing between metal d states and the O 2p states.

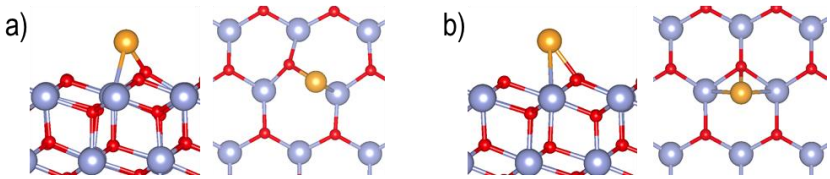

Figure 4.1. Side and top views of the (a) bridge and (b) hollow adsorption sites for the Au single atom on the ZrO_2 (101) surface. The same positions are found for the Ag single atom. Zr is represented by big blue atoms, O by small red atoms, and Au by big golden atom.

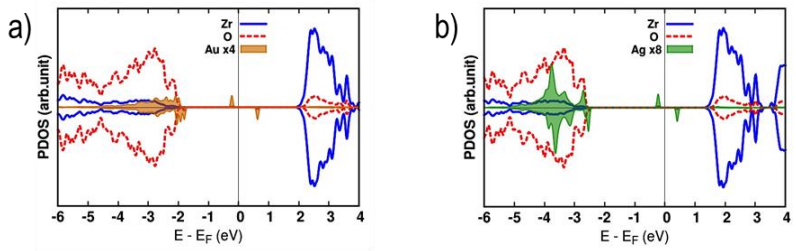

Figure 4.2. Projected Density of States (PDOS) of (a) Au and (b) Ag adsorbed on a Zr-O bridge position on the ZrO_2 (101) surface. The zero of energy corresponds to the Fermi level.

When the D2 correction was applied to account for the dispersion forces, also two competing adsorption sites were found. As expected, the adsorption energies were lowered. For Au, the energy was lowered by about 50%, while for Ag it was practically doubled in absolute value. The geometric structures of the two adsorption sites are unchanged, except for that of the Ag atom on the hollow Zr-O-Zr site, Figure 4.3. With the vdW forces, Ag is coordinated to three O_{3c} sites instead of to two Zr_{7c} and one O_{3c}. Moreover, this site becomes preferred, although by an energy difference of 0.02 eV only with respect the Zr-O bridge site.

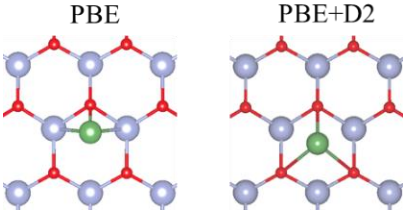

Figure 4.3. Top view of Ag atom adsorbed on the ZrO_2 (101) surface at without (PBE) and with (PBE+D2) vdW correction.

Table 4.2. Adsorption energies, E_{ads}, and Bader charges, q, of Au and Ag single atoms adsorbed on the ZrO_2 (101) surface.

		E_{ads} (eV)		
	site	PBE	PBE+D2	$q_{Au,Ag}$ (|e|)
Au_1/ZrO_2	bridge	-0.90	-1.27	-0.16
	hollow	-0.69	-1.03	-0.16
Ag_1/ZrO_2	bridge	-0.34	-0.70	0.01
	hollow	-0.28	-0.72	0.00

1.3 Au_4 and Ag_4 Cluster Adsorption on the ZrO_2 (101) Surface

In the gas phase, both Au_4 and Ag_4 clusters have preferentially rhombic structures. Thus, we started by placing the two clusters in a rhombic geometry on the ZrO_2 surface and optimize with and without dispersion forces.

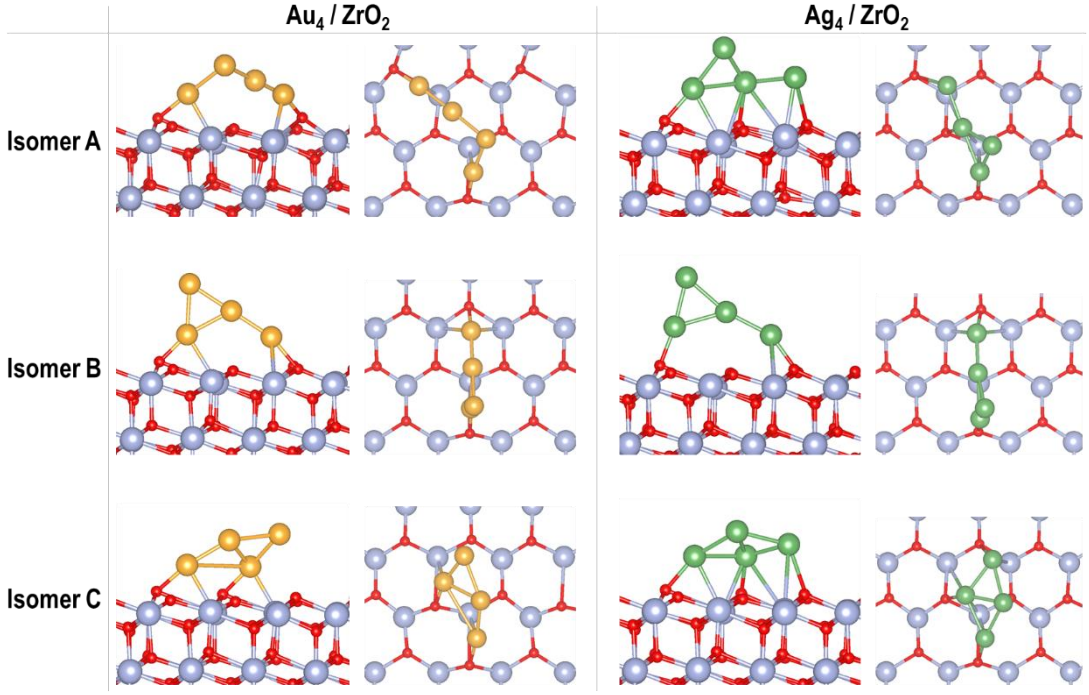

Figure 4.4. Side and top views of Au_4 and Ag_4 clusters adsorbed on the ZrO_2 (101) surface, forming (from top to bottom) isomers A, B, and C. Zr is represented by big blue atoms, O by small red atoms, Au by big golden atom, and Ag by big green atom.

In PBE calculations, without dispersion forces, Au_4 and Ag_4 assume three different two-dimensional structures, Figure 4.4, called isomers A, B and C. Isomers A and B completely lost the initial rhombic structure of the gas phase and formed a Y-shaped structure. In contrast, isomer C was rhombic-shaped. At the PBE level, the three isomers are separated by no more

than 0.3 eV, Table 4.3. The preferred configuration for both metals is the Y-shaped isomer A, with adsorption energies of -2.49 (Au_4) and -1.34 eV (Ag_4). In contrast, the relative stability of isomers B and C is reversed between Au_4 and Ag_4, although with an energy difference of 0.06-0.07 eV only.

Table 4.3. Adsorption energies, E_{ads}, of Au_4 and Ag_4 clusters adsorbed on the ZrO_2 (101) surface.

		E_{ads} (eV)			
	isomer	PBE	PBE+D2	PBE+D2'	vdw-DF
Au_4/ZrO_2	A	-2.49	-3.81	-3.51	-3.14
	B	-2.25	-3.27	-3.03	-2.77
	C	-2.19	-3.31	-3.07	-2.80
Ag_4/ZrO_2	A	-1.34	unstable	-2.17	-1.99
	B	-1.07	-2.09	unstable	unstable
	C	-1.15	-2.43	-2.10	-1.81

With vdW interactions, the Au_4 cluster maintains the preference for the isomer A. The adsorption energy goes from -2.49 eV (PBE) to -3.81 eV (PBE+D2), -3.51 eV (PBE+D2'), and -3.14 eV (vdW-DF). Clearly, looking also at the energies of isomers B and C, there is a tendency of PBE+D2 to provide an upper bound to the strength of dispersion interactions, whereas vdW-DF gives the smallest correction. PBE+D2' lies between the two. Regarding the structures, upon inclusion of the vdW forces, the tilted structure of the isomer C is pushed closer to the surface. This fact results in a more significant contribution of the vdW terms than for the vertical isomer B, which is less affected. This effect leads to an inversion in the stability of isomers B and C at the PBE+D2 and PBE+D2' levels with respect to the PBE calculations, but not to those at vdW-DF level.

The Ag_4 cluster, however, is more affected by the inclusion of the dispersion forces. This is in line with the findings for the single atoms. First, with the PBE+D2' and vdW-DF approaches, isomer B becomes unstable. With PBE+D2, isomer A is also unstable, but it remains the most stable at PBE+D2' and vdW-DF, with adsorption energies of -2.17 and -1.99 eV, respectively. Finally, at the PBE+D2 level, isomer C is the preferred one with a binding energy of -2.43 eV.

So, the inclusion of the vdW does not change the number of local minima, nor the prediction of the most stable structure (isomer A). The relative stability of the isomers B and C, however, changes between the different approaches, although it has to be noted that these two isomers are almost isoenergetic. The adsorption energies are considerably lower, and the

strongest effect is found with the D2 correction (ΔE ~ -1.3 eV). The vdW-DF approach instead provides the smallest corrections (ΔE ~ -0.6 eV), whereas the D2' correction lies between the two (ΔE ~ -0.9 eV).

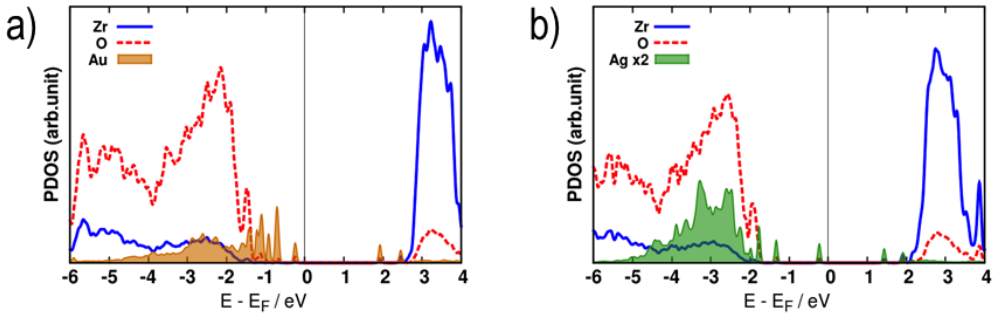

Figure 4.5. Projected density of states (PDOS) of the (a) Au_4 and (b) Ag_4 isomer A adsorbed on the ZrO_2 (101) surface. The zero of energy corresponds to the Fermi level.

The PDOS plots for the most stable isomer (A) of Au_4 and Ag_4 clusters are shown in Figure 4.5. Although the energetics is clearly affected by the inclusion of the vdW forces, the general features of the metal-oxide interaction are the same with and without vdW contribution. The valence states of Au_4 are typically above the top of the VB. However, those of the Ag_4 clusters appear highly mixed with the top O 2p states of the VB. Like in the single atoms case, there are no signs of charge transfer between ZrO_2 and the clusters. The Bader charges are always smaller than 0.3 |e|, a sign of the absence of net charge transfer at the interface. Still, there is an accumulation of density of charge on the Au_4 cluster (Bader charges between -0.25 and -0.32 |e|) from the chemical mixing with the oxide states and a relatively higher electron affinity of this metal. On Ag_4, the Bader charges are instead virtually zero. The neutrality or absence of net charge transfer is due to the closed-shell nature of the two tetramers as they have an even number of valence electrons. This implies a high ionization energy and a small electron affinity. Things could be radically different in the presence of a cluster with an odd number of Au and Ag atoms, like pentamers. This point will be addressed in the next section, where gold and silver pentamers will be also considered. In general, the inclusion of the vdW forces has no significant effects on the Bader charges of the metals, being the largest difference of 0.02 |e| only.

2 Support Effects: Role of Oxide Defects and Dopants on Au_n and Ag_n Clusters[5]

2.1 Introduction

Real catalysts are complex systems whose catalytic activity is determined by numerous different aspects. For instance, size effects and the metal-support interaction are of fundamental importance to determine the catalytic activity of the deposited catalysts. Also, under reaction conditions, the catalyst can undergo structural changes like sintering that decreases its activity (catalyst deactivation). So, it is possible to modify the electronic interaction between the metal and the supporting oxide in order to reinforce the bonding so sintering can be avoided, and/or to stimulate a net charge transfer so the catalytic activity of the metal can be improved. An important strategy to do so is oxide doping. For instance, Au clusters deposited on Mo-doped CaO films are reduced by electron transfer from the Mo dopants, and they transform from neutral and three-dimensional objects to negatively charge and bi-dimensional.[165] In general, the possibility to selectively charge supported clusters represents an interesting way to tune catalytic properties.

As particular catalysts, it has been found that Au, Ag or Cu/ZrO_2 are active catalysts for the WGS reaction,[65] for CO oxidation,[72,73] and for the synthesis of methanol from CO_2 and H_2,[213] and that the charge state of the metal plays an important role. Then, in this section, we have investigated in a systematic way the effect of two extrinsic defects, N- and Nb-substitutional doping, and an intrinsic defect, O vacancies, in ZrO_2 on the charge state of deposited Au and Ag atoms and clusters. N dopants, if it is not compensated by O vacancies, introduce low-lying acceptor states in the band gap of the hosting oxide. In this study, N was mainly used as a dopant with a potential to positively charge the deposited Au and Ag clusters. On the other hand, Nb dopants are used to introduce excess of electrons in the oxide and negatively charge the clusters.

To understand the tendency of the metal clusters to experiment charge transfer it has to be taken into account the closed- or open-shell nature of their electronic configuration. The valence electrons of Au and Ag atoms are the $6s^1$ and $5s^1$ electrons, respectively. So, the atom-like configuration is open-shell with a nonzero magnetic moment. Then, a zero magnetic moment from the electronic configurations ns^0 (M^+) and ns^2 (M^-) will indicate the occurrence

[5] This content has been published in P. Schlexer, A. Ruiz-Puigdollers, G. Pacchioni. Tuning the Charge State of Ag and Au Atoms and Clusters Deposited on Oxide Surfaces by Doping: A DFT Study of the Adsorption Properties of Nitrogen- and Niobium-Doped TiO_2 and ZrO_2. *Phys. Chem. Chem. Phys.* 2015, 17, 22342.

of a charge transfer from or to the metal atom, respectively. The same occurs with pentamers, as these clusters contain an odd number of atoms –odd number of valence electrons– and a nonzero magnetic moment in the neutral configuration like single atoms. On the contrary, tetramers are closed-shell systems in the neutral charge state, so the appearance of magnetic moment on the metals will indicate the occurrence of charge transfer at the interface.

2.2 Defective ZrO_2 (101) surface

First, it is important to describe the electronic structure of the defective ZrO_2 surface, as this will determine the electronic interaction with the deposited Au and Ag atoms and clusters. When an O vacancy is created, the extra electrons are localized in the vacancy coupled in a singlet state and high-lying Zr 4d donor states are introduced in the gap, Figure 4.6b. This does not change when the vacancy is created in a subsurface position. The properties of the O vacancies in zirconia has been explained in a more detailed in the Introduction chapter.

N atoms are pentavalent, so their introduction into the ZrO_2 lattice in O sites as N^{2-} ions results in an electronic configuration $2s^2 2p^5$. Then, substitutional N doping creates low-lying N 2p acceptor states whose distance from the top of the VB changes with the position of the N dopant. At the surface, the defect state was found at around 1 eV above the VB, Figure 4.6c. This position was found to be the most stable. When N is at the subsurface, the defect state lies only around 0.3 eV above the VB, Figure 4.6d.

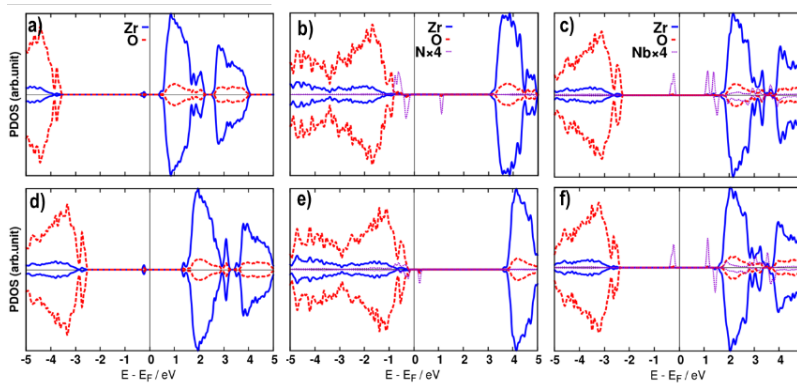

Figure 4.6. Projected density of states (PDOS) of ZrO_2 (a,b) with an O vacancy, (b,e) N-doped, and (c,f) Nb-doped in a (a-c) surface and a (d-f) subsurface position. The zero of energy corresponds to the Fermi level.

Similarly, when Nb, also pentavalent, substitutes Zr as Nb^{4+}, it can act as *n*-type dopant. The fifth valence electron remains localized on a Nb 4d orbital, since ZrO_2 bulk and surfaces are not reducible. For comparison, we mention that Nb doping in TiO_2, a reducible oxide, the

formation of Nb^{5+} and the reduction of Ti^{4+} ions to Ti^{3+} was observed. Then, in ZrO_2, Nb^{4+} introduced a donor state in the center of the gap, Figure 4.6(e,f). Note that the position of the Nb state does not depend on the position of the dopant (surface or subsurface).

2.3 Au_n and Ag_n Clusters (n = 1,4,5) on the ZrO_{2-x} (101) Surface with O vacancies

In this section, we first consider the effect of an intrinsic defect in the oxide: oxygen vacancies. Au and Ag atoms, tetramers, and pentamers were adsorbed on the ZrO_2 (101) surface with an O vacancy created in both a surface and subsurface positions, and on the stoichiometric surface for comparison. As seen previously in section §3.1.2, Au and Ag atoms were adsorbed on the stoichiometric ZrO_2 surface with an energy of -1.20 and -0.62 eV, respectively, and no net charge transfer occurred. This is confirmed with the presence of a nonzero magnetic moment generated by the unpaired $6s^1$ (Au_1^0) and $5s^1$ (Ag_1^0) electrons, and essentially zero Bader charges on the metals, Table 4.4. However, when both atoms were deposited on an O vacancy the bonding character is completely different. The bonding is not only covalent but also characterized by an electrostatic interaction due to a net charge transfer. One of the two extra electrons from the O vacancy was transferred and coupled with the ns^1 electron of the metal atom, as the vacancy states are higher in energy than the empty ns^β state of the metal. This results in a zero-magnetic moment on the metal but nonzero on the ZrO_2 surface due to the unpaired electron remaining in the vacancy. This is confirmed in the PDOS plots in Figures 4.7(a,c), showing the coupled $6s^2$ (Au_1^-) and $5s^2$ (Ag_1^-) states, and the Zr^{3+} state. The electrostatic interaction lowers significantly the binding energies: -4.22 eV for Au_1^- and -2.83 eV for Ag_1^- on top of a surface O vacancy, and Bader charges of -0.89 (Au_1^-) and -0.72 |e| (Ag_1^-), Table 4.4. When the O vacancy is located in a subsurface position, Figures 4.8(b,g), the same electronic interaction was obtained, but quantitatively weaker. The binding energies were -2.43 eV and Bader charge -0.57 |e| for Au_1^-, and -1.13 eV and Bader charge -0.44 |e| for Ag_1^-. Then, due to the open-shell nature of the Au and Ag single atoms, these are always reduced when deposited on the surface with O vacancies and with a binding energy notably higher than on the stoichiometric ZrO_2 surface.

Tetramers, however, are closed-shell clusters due to an even number of valence electrons (4 x ns^1 states). On the stoichiometric surface (see §3.1.3), Au_4 and Ag_4 clusters were adsorbed with an energy of -3.51 and -2.17 eV, respectively, and remained neutral. When a surface O vacancy is created, the two extra electrons are higher in energy than the first empty states of the M_4 clusters. In contrast to the single atoms, α and β states are degenerated in a closed-shell

system (non-spin polarized), so in M_4 there are two empty states that can be filled. Then, the two electrons of the vacancy are transferred to the clusters, and the magnetic moment on it continues to be 0, Table 4.4. This is confirmed with the PDOS plot, in which new occupied α and β states appear at around 1.5 (Au_4^{2-}, Figure 4.7b) and around 2.3 eV (Ag_4^{2-}, Figure 4.7g) above the top of the VB (compare with Figure 4.5). Accordingly, the binding energies are enhanced to -6.18 eV for Au_4^{2-} and to -4.30 eV for Ag_4^{2-}, with Bader charges of -1.22 and -0.95 |e|, respectively, Table 4.4. On the other hand, surprisingly, when the O vacancy was created in the subsurface position, Figures 4.7(d,i), no net charge transfer was observed. Both clusters remain neutral, and the binding energies are practically unchanged with respect to the deposition on the stoichiometric surface.

Table 4.4. Adsorption energies, E_{ads}, magnetic moments, μ_M (M = Au, Ag), and Bader charges, q_M (M = Au, Ag), of Au and Ag atoms, tetramers and pentamers deposited on stoichiometric and O deficient ZrO_{2-x} (101) surface, and number of electrons formally transferred, n_e.

surface	E_{ads} (eV)	μ_M (μ_B)	q_M (|e|)	n_e	E_{ads} (eV)	μ_M (μ_B)	q_M (|e|)	n_e
	Au_1				Ag_1			
ZrO_2	-1.20	0.4	-0.16	0	-0.62	0.2	+0.01	0
Vo, surface	-4.22	0	-0.89	1	-2.83	0	-0.72	1
Vo, subsurface	-2.43	0	-0.57	1	-1.13	0	-0.44	1
	Au_4				Ag_4			
ZrO_2	-3.51	0	-0.32	0	-2.17	0	0	0
Vo, surface	-6.18	0	-1.22	2	-4.30	0	-0.95	2
Vo, subsurface	-3.52	0	-0.35	0	-2.24	0	-0.02	0
	Au_5				Ag_5			
ZrO_2	-2.84	0.4	0	0	-2.05	0.2	0	0
Vo, subsurface	-2.94	0	-0.52	1	-2.00	0.2	0	0

For the pentamers, we only considered the O vacancy created directed in subsurface, since the surface one is known to be very reactive with potentially reductive gap electrons. Surprisingly, in spite of the open-shell nature of both Au_5 and Ag_5 clusters, only gold was reduced when deposited on the subsurface vacancy, according to the zero-magnetic moment, the presence of closed-shell Au states, and only one electron on a Zr^{3+} state, Figure 4.7e. It has been seen in the tetramers that the electrons of a subsurface defect are not high enough in energy to reduce the closed-shell clusters. In pentamers it is only possible for gold due to a higher electronegativity of this metal. However, the binding energy of Au_5^- was only enhanced to -2.94 eV (compared to -2.84 eV on stoichiometric ZrO_2).

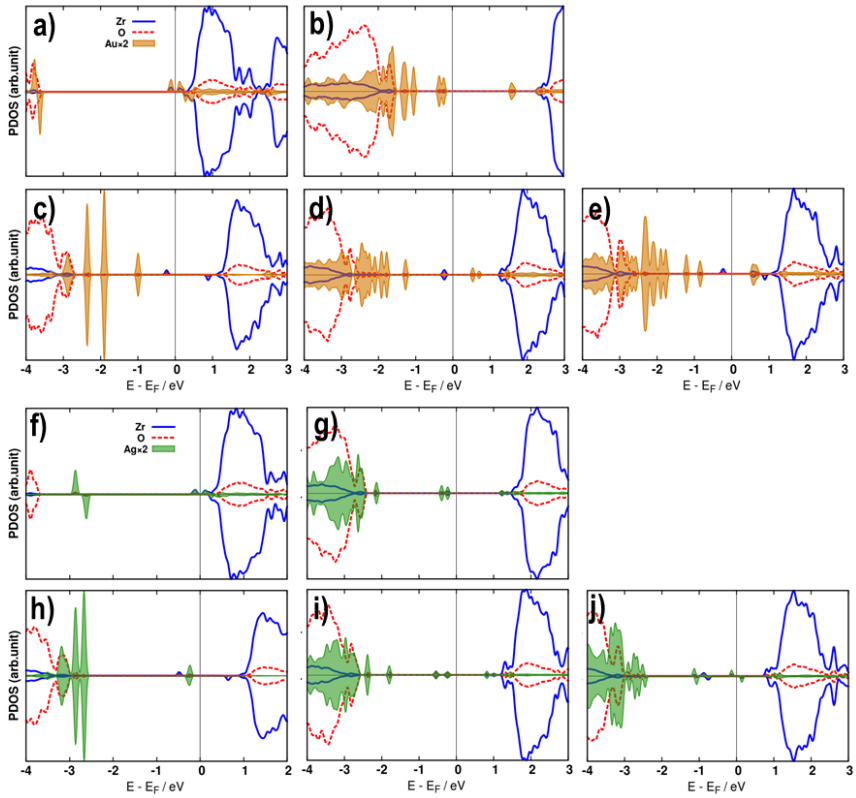

Figure 4.7. Projected density of states (PDOS) of a Au (a,c) atom, (b,d) tetramer, and (e) pentamer on ZrO_2 with a (a,b) surface O vacancy and a (c-e) subsurface O vacancy, and of a Ag (f,h) atom, (g,i) tetramer, and (j) pentamer on top of a (f,g) surface O vacancy and of a (h-j) subsurface O vacancy. The zero of energy corresponds to the Fermi level.

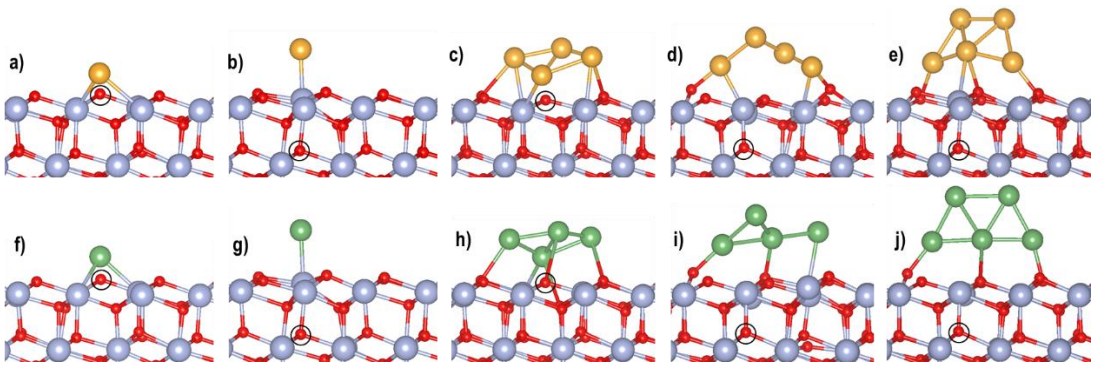

Figure 4.8. Structures of a Au (a,b) atom, (c,d) tetramer, and (e) pentamer on ZrO_2 with a (a,c) surface O vacancy and a (b,d,e) subsurface O vacancy; structures of a Ag (f,g) atom, (h,i) tetramer, and (j) pentamer on top of a (f,h) surface O vacancy and of a (g,i,j) subsurface O vacancy. Zr is represented by big blue atoms, O by small red atoms, Au by big golden atoms, and Ag by big green atoms. The O vacancy is indicated with a black circle.

Regarding the atomic structure, both Au and Ag atoms try to fill the O vacancy when this is at surface, Figures 4.8(a,f). In the subsurface position, the metal is adsorbed on top of the Zr site that is vertically above the O vacancy, Figures 4.8(b,g). These two types of adsorption structures maximize the electrostatic interaction between the vacancy and the metal. Similarly, in deposited Au_4^{2-}, Ag_4^{2-}, and Au_5^- clusters it was always observed that one metal atom tries to fill the surface O vacancy and be as coordinated as possible, so the covalent and electrostatic bonding is maximized. However, as the subsurface vacancy does not provide a new and different bonding due to charge transfer, the atomic structure of the Au_4^0, Ag_4^0, and Ag_5^0 clusters remains unchanged with respect to those on the stoichiometric ZrO_2. This kind of local structural relaxation will have important implications in the stabilization of the vacancies and therefore in the reactivity of surface oxygen atoms, which will be deeply discussed in the section §4.3 about reactivity of Au/ZrO_2 catalysts.

2.4 Au_n and Ag_n Clusters (n = 1,4,5) on the N-Doped $ZrO_{2-x}N_y$ (101) Surface

For N doping, like in the O vacancies case, we considered two different positions: surface and subsurface. In general, the adsorption energies for Au and Ag atoms on the N-doped surface are higher in modulus than the stoichiometric and reduced surfaces (compare Tables 4.4 and 4.5). The magnetic moments on Au_1 and Ag_1 was always zero, and the Bader charges were positive. These features strongly suggest that that both atoms have been oxidized upon deposition on the N-doped surface; the ns^1 electron has been transferred to the low-lying N 2p empty states reducing the dopant to N^{3-}. This is reinforced with the analysis of the PDOS. In each case, the N 2p states appears doubly occupied below the Fermi level, and the metal ns states become doubly empty above the Fermi, Figures 4.9(a,c,f,h). The same oxidative bonding was obtained when the N dopant is located in the subsurface position. In this case, the N 2p states appear in a lower energy, which implies a higher energy gain when receives the ns^1 electron from the metals. In fact, in the Ag case the binding energy is higher in the subsurface than in the surface N doping.

Similarly, the binding energies of Au_4 and Ag_4 clusters on the N-doped surface are higher than those on the stoichiometric and reduced one. Now, nonzero magnetic moments were obtained, indicating that a charge transfer has occurred. Considering also the positive Bader charges, also the tetramers have been oxidized upon deposition on the surface and subsurface N-doped ZrO_2. Also, the N 2p states are doubly occupied in the PDOS plots, Figures 4.9(b,d,g,i). As it has been seen in the description of the clean N-doped ZrO_2 surface (§4.2.2),

the subsurface N-dopant introduced N 2p states that were lower in energy compared to the surface position (closer to the VB). Filling such hole with the cluster electrons releases more energy resulting in a stronger bonding, as seen in Table 4.5.

Table 4.5. Adsorption energies, E_{ads}, magnetic moments, μ_M (M = Au, Ag), and Bader charges, q_M (M = Au, Ag), of Au and Ag atoms, tetramers and pentamers deposited on stoichiometric and N-doped $ZrO_{2-x}N_y$ (101) surface, and number of electrons formally transferred, n_e.

surface	E_{ads} (eV)	μ_M (μ_B)	q_M (|e|)	n_e	E_{ads} (eV)	μ_M (μ_B)	q_M (|e|)	n_e
	Au_1				Ag_1			
ZrO_2	-1.20	0.4	-0.16	0	-0.62	0.2	+0.01	0
N, surface	-3.14	0	+0.14	1	-2.67	0	+0.27	1
N, subsurface	-2.77	0	+0.29	1	-2.97	0	+0.51	1
	Au_4				Ag_4			
ZrO_2	-3.51	0	-0.32	0	-2.17	0	0	0
N, surface	-4.23	0.3	-0.19	1	-3.83	0.2	+0.38	1
N, subsurface	-4.53	0.5	+0.18	1	-4.33	0.2	+0.48	1
	Au_5				Ag_5			
ZrO_2	-2.84	0.4	0	0	-2.05	0.2	0	0
N, subsurface	-5.01	0	+0.20	1	-4.84	0	+0.49	1

The same oxidative bonding can be suggested for pentamers. In this case, we only considered the N doping in a subsurface position. Zero magnetic moments and positive Bader charges are obtained after deposition on the N-doped surface, meaning that the initial unpaired electron has been transferred to the N 2p empty states.

The structures of Au and Ag atoms, tetramers and pentamers on the N-doped ZrO_2 surface are shown in Figure 4.10. If the N atom is at the surface, Au^+ and Ag^+ stay in close contact to it, Figures 4.10(a,f). In the subsurface position, both metals are instead coordinated to 3 O_{3c} sites in a hollow, as metals are positively charged, Figures 4.10(b,g). The structures of the tetramers on the N-doped oxide resemble those on the stoichiometric, in particular the Y-shaped isomer for Au_4^+ and the rhombus for Ag_4^+, Figures 4.10(c,d,h,i). The structure of the pentamers is however notably changed with respect to that on the stoichiometric surface, Figures 4.10(e,j). The cluster tends to maximize the contact with the surface so that the electrostatic energy (that between charged N^{3-} and M_5^+ species) is minimized.

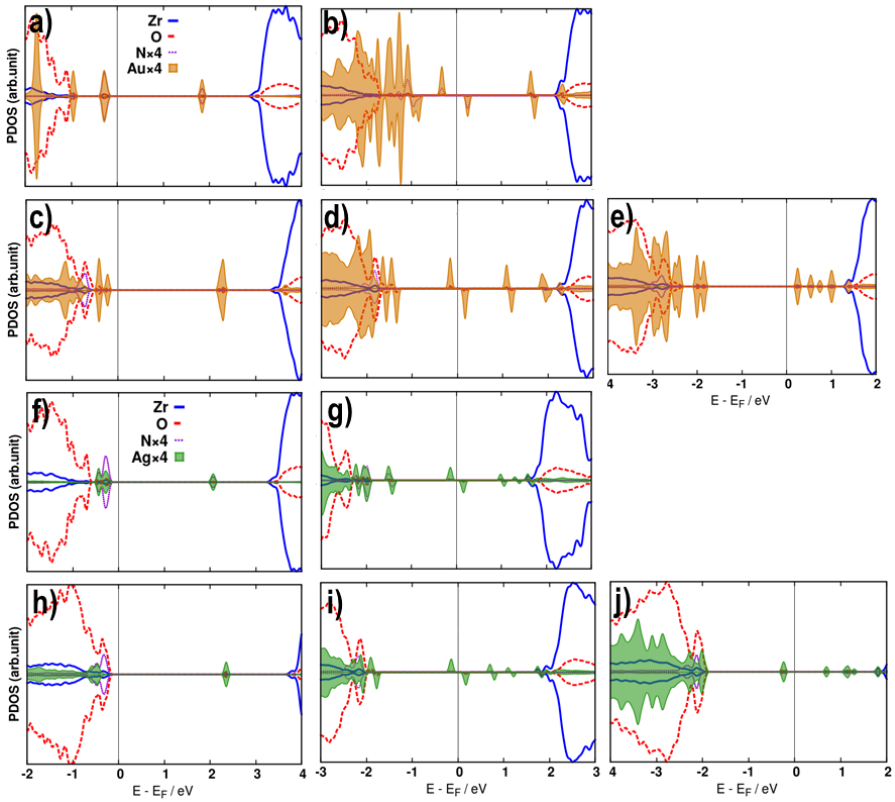

Figure 4.9. Projected density of states (PDOS) of a Au (a,c) atom, (b,d) tetramer, and (e) pentamer on N-doped ZrO_2 with N atom in (a,b) surface and (c-e) subsurface, and of a Ag (f,h) atom, (g,i) tetramer, and (j) pentamer on N-doped ZrO_2 with N atom in (f,g) surface and (h-j) subsurface. The zero of energy corresponds to the Fermi level.

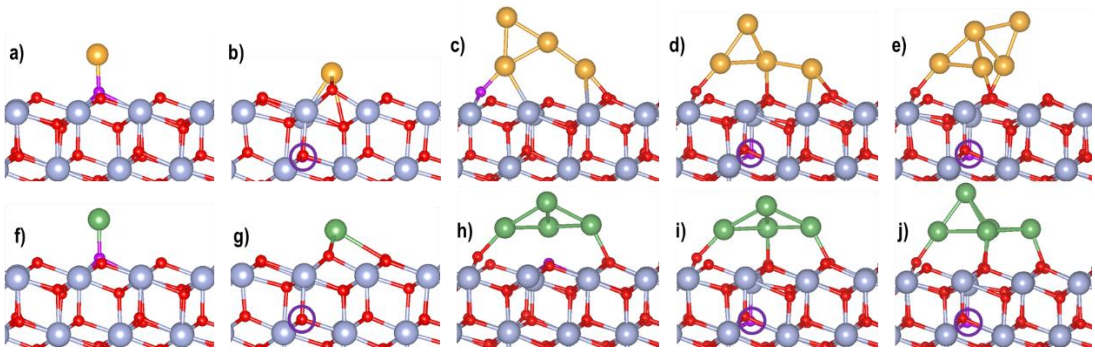

Figure 4.10. Structures of a Au (a,b) atom, (c,d) tetramer, and (e) pentamer on N-doped ZrO_2 with N atom in (a,c) surface and (b,d,e) subsurface; structures of a Ag (f,g) atom, (h,i) tetramer, and (j) pentamer on N-doped ZrO_2 with N atom in (f,h) surface and (g,i,j) subsurface. Zr is represented by big blue atoms, O by small red atoms, N by small purple atoms, Au by big golden atoms, and Ag by big green atoms. Subsurface N atoms are also indicated with a purple circle.

2.5 Au_n and Ag_n Clusters (n = 1,4,5) on the Nb-Doped $Zr_{1-x}O_2Nb_y$ (101) Surface

After deposition of Au and Ag atoms on the Nb-doped surface, the excess electron remained always localized on the Nb atom. The metals remained neutral in the atom-like electronic configuration, Table 4.6. Then, no charge transfer occurred. Interestingly, the binding energies are even lower than those on the non-doped stoichiometric surface, in exception of the Ag_1 on top of the surface Nb site, due to the chemical mixing between Nb and Ag states. The absence of charge transfer can be understood by the PDOS plots, Figures 4.11(a,c,f,h). As said previously (§4.2.2), the Nb atom introduce a donor state in the band gap but at an energy level that is not high enough to be transferred to the empty states of the Au and Ag atoms. It can be seen always around 1 eV below the LUMO state of the metals (ns^{β}).

Table 4.6. Adsorption energies, E_{ads}, magnetic moments, μ_M (M = Au, Ag), and Bader charges, q_M (M = Au, Ag), of Au and Ag atoms, tetramers and pentamers deposited on stoichiometric and Nb-doped $Zr_{1-x}O_2Nb_y$ (101) surface, and number of electrons formally transferred, n_e.

surface	E_{ads} (eV)	μ_M (μ_B)	q_M (|e|)	n_e	E_{ads} (eV)	μ_M (μ_B)	q_M (|e|)	n_e
	Au_1				Ag_1			
ZrO_2	-1.20	0.4	-0.16	0	-0.62	0.2	+0.01	0
Nb, surface	-1.17	0.4	-0.08	0	-0.82	0.2	+0.12	0
Nb, subsurface	-0.88	0.4	-0.13	0	-0.53	0.2	-0.01	0
	Au_4				Ag_4			
ZrO_2	-3.51	0	-0.32	0	-2.17	0	0	0
Nb, surface	-3.34	0	-0.26	0	-2.37	0	+0.04	0
Nb, subsurface	-3.12	0	-0.27	0	-1.94	0	0	0
	Au_5				Ag_5			
ZrO_2	-2.84	0.4	0	0	-2.05	0.2	0	0
Nb, subsurface	-2.63	0.4	-0.32	0	-1.61	0.2	+0.02	0

Neither Au_4 and Ag_4 clusters experimented a charge transfer on the Nb-doped surface, resulting in unchanged zero magnetic moments and similar Bader charges as on the undoped surface, Table 4.6. The reason is the same as in the atoms case: the Nb dopant did not provide reducing electrons with high enough energy, as seen in Figures 4.11(b,d,g,i). Considering the adsorption energies, these are even destabilized compared to the undoped surface. Only silver was bonded stronger on top of the surface Nb site. Due to the same reasons, also the pentamers remained neutral and their binding energies were weakened with respect to those on undoped ZrO_2. Finally, not surprisingly, the structures of all clusters were only slightly modified due to only a chemical mixing between the metal and the Nb states, Figure 4.12.

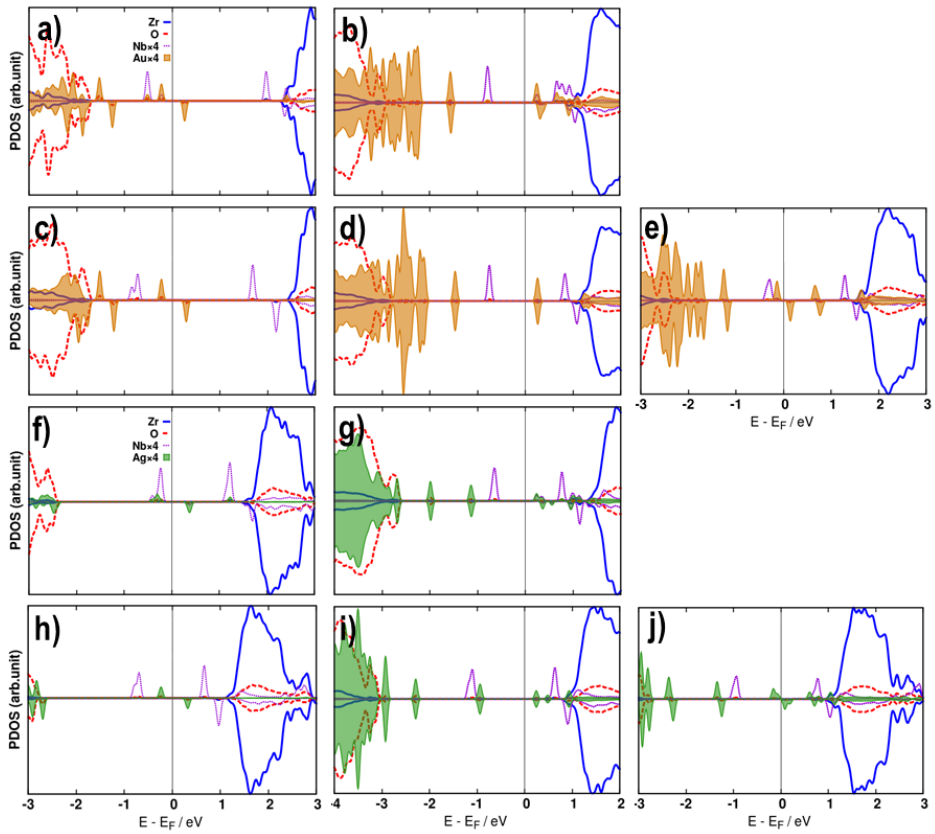

Figure 4.11. Projected density of states (PDOS) of a Au (a,c) atom, (b,d) tetramer, and (e) pentamer on Nb-doped ZrO_2 with Nb atom in (a,b) surface and (c-e) subsurface, and of a Ag (f,h) atom, (g,i) tetramer, and (j) pentamer on Nb-doped ZrO_2 with Nb atom in (f,g) surface and (h-j) subsurface. The zero of energy corresponds to the Fermi level.

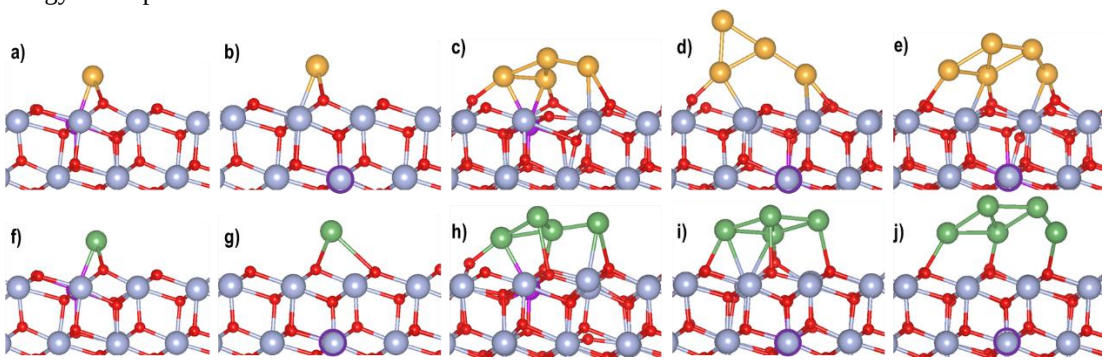

Figure 4.12. Structures of a Au (a,b) atom, (c,d) tetramer, and (e) pentamer on Nb-doped ZrO_2 with Nb atom in (a,c) surface and (b,d,e) subsurface; structures of a Ag (f,g) atom, (h,i) tetramer, and (j) pentamer on Nb-doped ZrO_2 with Nb atom in (f,h) surface and (g,i,j) subsurface. Zr is represented by big blue atoms, O by small red atoms, Nb by big purple atoms, Au by big golden atoms, and Ag by big green atoms. Subsurface Nb atoms are also indicated with a purple circle.

In summary, these intrinsic or extrinsic defects modify in a completely different way the electronic properties of the oxide, modifying also the interaction with the deposited atoms and clusters. This, in turn, may modify their reactivity. For example, O vacancies reduce the metal atoms and clusters, and enhance their binding to the surface. This may be exploited to attract and bind electrophilic species like O_2 and CO_2, as well as for attenuate the sintering of the particles. The same is valid for N doping, but in this case oxidizing the deposited particles. Oxidized particles can attract nucleophilic species like CO. Notice that in this analysis, we considered simplified models where the dopants are isolated and do not concur to the formation of other compensating defects (for instance it is known that N doping favors the formation of O vacancies). However, it has been seen that Nb dopants did not have major effects on the adsorption behavior of the Au and Ag particles.

3 Reactivity of Metal Catalysts: CO Oxidation at the Au/ZrO_2 Interface[6]

3.1 Introduction

Au-based nanosized catalysis receives special attention due to its effectiveness in hydrogenation and cracking reactions,[247] hydrochlorination reactions,[248] the WGS reaction,[249,250] hydrocarbon selective oxidation,[251,252] and especially in reactions involving molecular O_2.[253] However, the simplicity of the CO oxidation reaction and impact in chemistry and industry led it to be of enormous importance in the fields of catalysis and nanocatalysis. This reaction became central in the elucidation of the origin of the high catalytic activity at low temperatures since Haruta et al. reported in 1987 the effectivity of nano-sized Au particles on TiO_2 in oxidation reactions.[151,254]

Haruta, and many other groups, demonstrated that the Au-oxide interaction has also a determinant role on the catalytic activity, even more important than the size effects of the deposited Au catalysts.[255] The oxide can change the size and morphology of the deposited metal particle, and its charge state via electron transfer.[10] It can also induce a strain in the Au particles from a lattice mismatch in the interface, affecting the reactivity by changes in the electronic structure and by a higher trend to structural rearrangement.[156,256]

Schubert et al. differentiated between reducible oxides, that were considered to be the active, and nonreducible oxides that instead were considered inactive for the CO oxidation reaction.[32] Numerous studies demonstrate that the Au/TiO_2 catalyst exhibits without any doubt the highest activity. However, sufficient number of investigations defend that reducibility is not the key factor to classify the supports for the CO oxidation.[253,257,258] For example, Lopez et al showed that Au supported on reducible oxides were at most 2-4 times more active than on nonreducible ones.[259]

The debate about the support-activity correlation is due to the uncertainty present in the reaction mechanism for the CO oxidation. In particular, the source of active oxygen to oxidize the CO molecule is discussed most controversially. Several studies suggest that CO is oxidized by molecular O_2 adsorbed on the Au catalyst,[260,261,262,263] but only possible at very low temperatures as O_2 desorbs from Au at 170 K.[264] Also, computational studies report very low adsorption energies for O_2 on Au/TiO_2,[261] Au/RuO_2,[262] or Au/MgO.[263] In order to bind O_2 and activate it, a charge reservoir is necessary.[263,243] Surface O vacancies, by charge transfer, form

[6] The content of this section is published in A. Ruiz Puigdollers, G. Pacchioni. CO Oxidation on Au Nanoparticles Supported on ZrO_2: Role of Metal/Oxide Interface and Oxide Reducibility. *ChemCatChem* 2017, 9, 1.

peroxides (O_2^{2-}) and superoxides (O_2^-). These species dissociate then into stable O^- species that oxidize the CO molecule. So, in this case, a Langmuir–Hinselwood (LH) mechanism is generally accepted for the CO oxidation, where both O^- and CO species are adsorbed and diffuse to the reactive center.

Behm et al. reported a Au-assisted Mars van-Krevelen (MvK) mechanism for the CO oxidation on Au/TiO_2.[33] Here, the Au-adsorbed CO molecule reacts with a surface lattice oxygen at the interface to form CO_2 and an O vacancy, which is then refilled by O_2 from the gas phase. The steps are independent in a microscopic and local picture, and the surface vacancies reach a steady-state concentration. Clearly, this mechanism is sensitive to the reducibility of the oxide. Meada et al. demonstrated the formation of O vacancies on TiO_2 during the CO oxidation at 473 K.[265]

As a nonreducible oxide, the activity of ZrO_2 on this reaction is lower than other reducible oxides like TiO_2. Behm postulated that on nonreducible oxides like ZrO_2, MgO, SiO_2, and Al_2O_3 the support does not play a fundamental role in the catalytic process. However, as it has been seen in the Nanostructuring section and in other works, the performance of the ZrO_2-based catalyst is enhanced by nanoscaling the ZrO_2 support.[72,102,103] Then, those observations could be in agreement with a Au-assisted MvK mechanism. Since the formation of O vacancies on the ZrO_2 surface is a high temperature process,[253] the MvK mechanism can be plausible for the high temperature CO oxidation. Also, and more importantly, it has been observed that the deposition of metal nanoparticles enhances the reduction of the oxide.[266,267,268] In this section, we demonstrate that Au particles promote the formation of surface O vacancies in such a way the MvK becomes perfectly a possible mechanism for CO oxidation on ZrO_2. We suggest that the activity observed in the Au/ZrO_2 catalyst in the CO oxidation may come from a significant improvement of the surface reducibility of ZrO_2.

Computational Details

The t-ZrO_2 (101) surface was modeled by a 2 × 4 supercell (7.323 x 25.562 Å) with 5 layers ($Zr_{80}O_{160}$). The Au catalyst was modeled by a 0.5 nm diameter nanorod formed by 10 Au atoms/cell and periodic along the short axis (*a*), so the metallic character is described. The lattice parameter for bulk Au(*fcc*) was calculated to be 2.898 Å (experimental 2.884 Å[210]). This means that, oriented along the *a* axis, there is a lattice mismatch of +3.1%. The expansive strain produces longer Au–Au bonds that increase the reactivity of the metal. Moreover, the strain causes the loss of crystallinity after geometry optimization. We note that the lack of

crystallinity is not a computational issue: the characteristic Au(111) fringes of 1.5 – 2 nm Au nanoparticles are not identified by HRTEM analysis.[28]

The binding energies reported in this study do not include the entropic terms. Defining the Gibbs free energy as $\Delta G_{ads} = \Delta H_{ads} - T(S_{ads} - S_g)$, where ΔH_{ads} is the adsorption enthalpy and approximated to the change in DFT energies, and S_{ads} and S_g are the entropy of the adsorbed and gas-phase molecules, respectively. For small molecules like CO, O_2, and CO_2, S_{ads} can be neglected. At 298 K and 1 bar, we calculated a $T \cdot S_g$ correction of 0.61 (CO), 0.63 (O_2), and 0.66 (CO_2) eV for ΔH_{ads}. These values are such that they do not change the general conclusions based on the analysis of the DFT total energies.

3.2 Formation of O Vacancies at the Au/ZrO_2 Interface

One of the most relevant aspects in the Au-assisted MvK mechanism for CO oxidation is the reducibility of the support. On the ZrO_2 (101) surface, the formation of a O vacancy costs +5.79 eV, at the PBE+U level. This means that removing a surface oxygen by CO to form CO_2 is a highly endothermic process, with an energy cost of +2.48 eV, calculated as $\Delta E_{reac} = E(ZrO_{2-x}) + E(CO_{2,(g)}) - [E(ZrO_2) + E(CO_{(g)})]$. Things change substantially when Au metallic particles are deposited on the surface. We calculated the formation energy of a surface O vacancy at four different distances from the supported Au nanorod. Creating a vacancy below (Vo1) and at the perimeter (Vo2) of the nanorod costs, respectively, 3.39 and 3.36 eV less than in the clean ZrO_2 surface (+2.40 and +2.43 eV versus +5.79 eV, respectively, Table 4.7). Creating the vacancy at 6.3 Å from the center of the nanorod (Vo3) costs +4.21 eV, and in the following row of O atoms, at 9.3 Å (Vo4), +5.45 eV. Clearly, the formation energy of a surface O vacancy is considerably reduced at the interface with the Au nanorod, and it increases as the vacancies are formed far from it. Based on these results, it is not surprising that the removal of a surface O_{latt} ions close to the metal (Vo1 and Vo2) from a CO to form CO_2 is thermodynamically favored, with exothermic reaction energies -0.86 and -0.83 eV, respectively, Table 4.7. This is in complete agreement with the fact that the ions in the metal–oxide interface are the active sites and the CO oxidation reaction occurs at the perimeter of the supported metal.[33,269]

The decrease of the formation energy of the surface O vacancies can be rationalized mainly by (1) the transfer of the extra electrons associated to the O vacancy to Au, and (2) the structural change of the Au rod in response to the creation of the surface defect. On clean ZrO_2, the extra charge associated to the O vacancy remains localized in the vacancy (F center), and

introduces a high–lying gap state in the electronic structure, due to the non-reducible character of zirconia. Instead, the deposited Au particle acts as an electron scavenger, accepting the electrons of the vacancy. Upon formation of Vo1, Vo2, or Vo3 vacancies, the two electrons are transferred to Au, resulting in Bader charges -1.4, -1.4, and -1.3 |e|, respectively, Table 4.7. At a longer distance, Vo4, only one electron is transferred to Au while the other remains localized on a Zr^{3+} center, giving a triplet ground state and a Bader charge of -0.8 |e| on Au. Thus, since Au is being reduced and not the zirconia surface, the O vacancy formation is promoted in the presence of Au. Moreover, the charge transfer at the interface enhances the binding energy of the Au nanorod on the surface with respect to the stoichiometric surface.

Table 4.7. Distance from the Au nanorod, $d_{Vo\text{-}Au}$, and formation energy, $E_{f,Vo}$, of surface O vacancies at various positions, and resulting reaction energy for CO oxidation as a function of the O_{latt} position; adsorption energy, $E_{ads,Au}$, total spin, $N_\alpha - N_\beta$, and Bader charges, q, of Au on the stoichiometric and reduced ZrO_2 surface.

system	Vo site	d_{Vo-Au} (Å)[a]	$E_{f,Vo}$ (eV)	ΔE_{reac} (eV)[b]	$E_{ads,Au}$ (eV)	$N_\alpha - N_\beta$	q_{Au} (|e|)
ZrO_{2-x}	-	-	+5.79	+2.48	-2.20	0	-0.2
Au/ZrO_{2-x}	Vo1	0	+2.40	-0.86	-5.53	0	-1.4
	Vo2	3.0	+2.43	-0.83	-5.50	0	-1.4
	Vo3	6.3	+4.21	+0.94	-3.73	0	-1.3
	Vo4	9.3	+5.45	+2.19	-2.92	2	-0.8

[a]The distances are measured from the surface O_{latt} located just under the Au nanorod (Vo1).
[b]$\Delta E_{reac} = E(ZrO_{2-x}) + E(CO_{2,(g)}) - [E(ZrO_2) + E(CO_{(g)})]$.

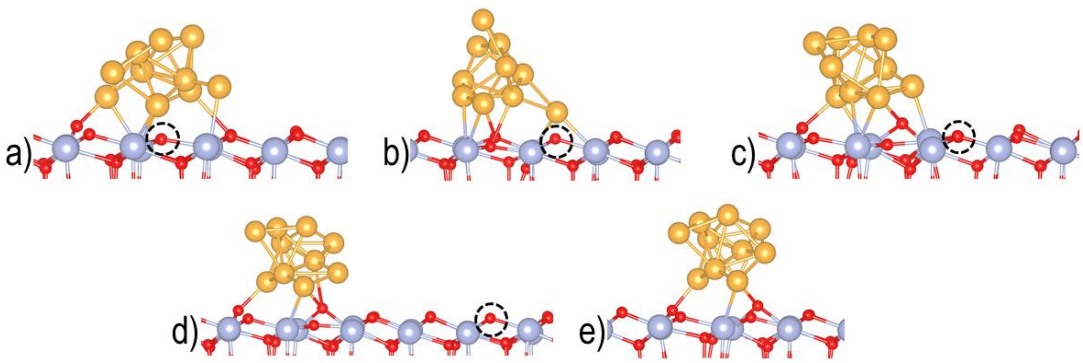

Figure 4.13. Structures of the Au nanorod on the zirconia surface with a surface O vacancy (dotted circle) located at different distances from Au. (a) Vo1, (b) Vo2, (c) Vo3, (d) Vo4, and (e) stoichiometric surface. Zr is represented by blue atoms, O by red atoms and Au by golden atoms.

The second aspect stabilizing the O vacancies at the Au/ZrO_2 interface is the flexibility of the Au rod. As expected, the highest deformations with respect to Au on the stoichiometric surface (Figure 5.13e) are obtained for Vo1 and Vo2, Figures 4.13(a,b). This is due to a shorter

and stronger Vo-Au interaction and to a larger charge transfer. At the largest distance, Vo4, the Au rod remains practically unchanged compared the stoichiometric surface (Figure 4.13d). Note that in the atomic reorganization the Au atoms tend to move towards the vacancy. On the Vo2 vacancy, one Au atom is clearly displaced to fill the vacancy, being practically detached from the rest of the nanorod, Figure 4.13b. As already pointed out by Molina et al. for the Au/TiO_2 catalyst,[263] filling the vacancy with a Au atom implies a decrease in reactivity. However, this behavior is found in amorphous and highly fluxional metal particles, like the Au nanorod of the present study. Instead, Au atoms coordinated in a crystalline environment remain fixed in the cluster rather than moving to the vacancy.[263] In this case, however, the relaxation would not contribute so much in stabilizing the vacancies.

The strain leads the Au structure to distort and rearrange more easily, as a mechanism to release the strain. In order to evaluate whether the significant stabilization of O vacancies is produced by an excessive strain, we calculated an O vacancy under three finite and non–strained Au atom, tetramer and pentamer, Figure 4.14. Here, the vacancy formation energy was +2.90, +2.61, and +2.20 eV for Au_1, Au_4, and Au_5 clusters, respectively, which is notably lower than the value on the clean surface (+5.97 eV). Furthermore, the displacement of a Au atom toward the vacancy can be observed in all cases after geometry optimization. Therefore, we can conclude that the stabilization of the interface O vacancies is mainly due to electronic effects and local atomic rearrangements, while the small strain present (+3.1%) in the supercell should not affect significantly.

Table 4.8. Formation energy, $E_{f,Vo}$, of a surface O vacancy near a finite Au_n cluster, and resulting reaction energy for the CO oxidation reaction.

system	$E_{f,Vo}$ (eV)	ΔE_{reac} (eV)
Au_1/ZrO_{2-x}	+2.90	-0.36
Au_4/ZrO_{2-x}	+2.61	-0.65
Au_5/ZrO_{2-x}	+2.20	-1.06

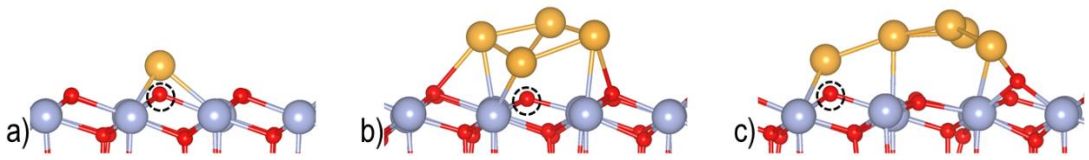

Figure 4.14. Structures of a Au (a) atom, (b) tetramer, and (c) pentamer on top of a surface O vacancy (dotted circle) on zirconia. Zr is represented by big blue atoms, O by small red atoms, and Au by big golden atoms.

In the following section, we consider the O_{latt} at the interface site closest to the nanorod, named Vo2, as the active oxygen for the first step of the CO oxidation reaction, as the reaction energy is highly exothermic at this site (-0.83 eV) and it is accessible by the CO molecule.

3.3 CO Oxidation Reaction Mechanism

We divided the Au-assisted MvK mechanism for the CO oxidation on Au/ZrO_2 in three elementary steps. First, a Au-adsorbed CO molecule extracts a lattice oxygen to form CO_2 and a surface O vacancy (Eq. 1). Second, the vacancy is refilled with an O_2 molecule from the gas-phase generating an oxidized surface (Eq. 2). Finally, a second CO molecule reacts with the O_{ads} left in the reoxidation releasing a second CO_2 to the gas phase and regenerating the initial stoichiometric system (Eq. 3).

$$CO_{ads} + Au/ZrO_2 \rightarrow CO_{2,(g)} + Au/ZrO_{2-x} \quad (1)$$

$$Au/ZrO_{2-x} + O_{2,(g)} \rightarrow O_{ads}/Au/ZrO_2 \quad (2)$$

$$O_{ads}/Au/ZrO_2 + CO_{ads} \rightarrow Au/ZrO_2 + CO_{2,(g)} \quad (3)$$

3.3.1 Step 1 – CO Oxidation by Lattice Oxygen.

The reaction energy profile for the first step is shown in Figure 4.15. The CO molecule is adsorbed on the Au nanorod with a binding energy of -1.44 eV, and a Au-C bond of 1.93 Å is formed. Considering the entropy contribution, ΔG_{ads} = -0.83 eV, which is still negative. The preference for the adsorption on the Au particle rather than on the oxide has been demonstrated computationally and experimentally.[33,269] It is worth mentioning that the most stable CO adsorption site is not close to the Au/ZrO_2 interface but at around 4 Å from the surface. Molina et al. observed the same behavior on the Au/MgO catalyst.[263]

From a distance of 4.34 Å, the CO molecule approaches the O_{latt} and reaches the transition state (TS) at a OC-O_{latt} distance of 1.93 Å. A CO_2 molecule is then formed on top of a surface O vacancy with two C-O distances of 1.28 Å, and an OCO angle of 119.8º. It is an exothermic process, with -0.36 eV of energy gain. Kinetically, it is an activated process, with an energy barrier of 0.79 eV. As expected, this barrier is higher than that found on highly active TiO_2-supported Au catalysts, where it has been calculated to be 0.5 eV[258] and experimentally estimated between 0.1 – 0.4 eV.[27,32,270] On the other hand, the barrier 0.79 eV is smaller than that found for MgO-supported Au particles (1.1 – 1.7 eV, from DFT calculations[263]).

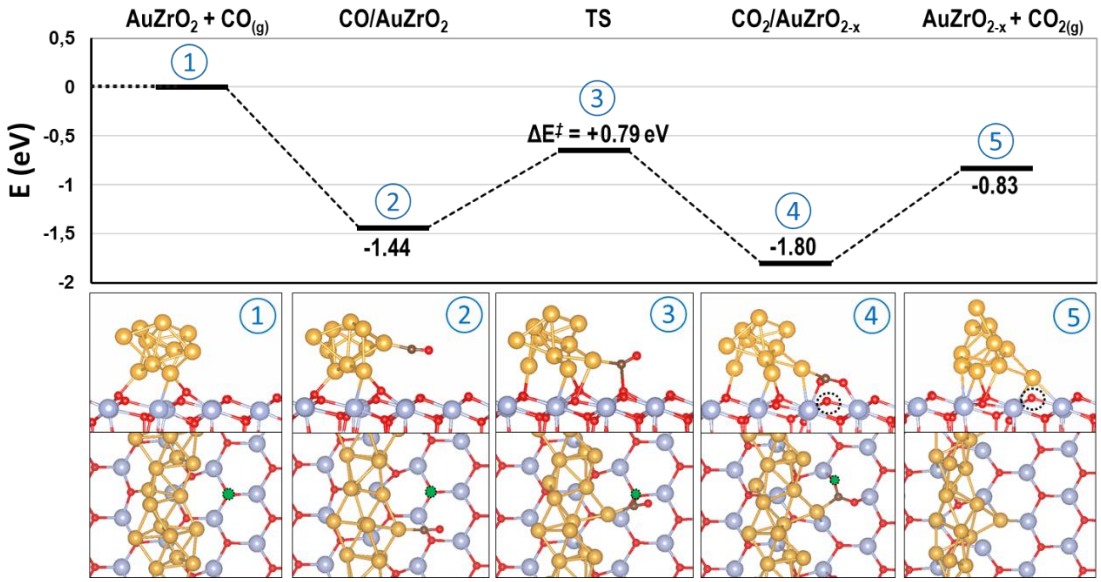

Figure 4.15. (top) Reaction energy profile and (bottom) side and top view of the structures of the CO oxidation reaction with a surface O_{latt}. The O_{latt} abstracted is indicated by a green filled circle, and the O vacancy by a dotted circle. Zr is represented by big blue atoms, O by small red atoms, Au by big golden atoms, and C by small brown atoms.

One electron of the vacancy is transferred to the π* orbital of CO_2, as shown by a Bader charge of -1.05 |e| on CO_2; the other electron of the vacancy is transferred to Au (Bader charge of -0.52 |e|). Oxide surfaces with electron rich defects such as O vacancies are chemically more reactive in activating the CO_2 molecule.[271] Indeed, this results in the formation of the adsorbed bent CO_2^- molecule, which explains the exothermicity of the process. In the next step CO_2^- transfers the electron to Au and CO_2 is desorbed to the gas phase with an energy cost of 0.97 eV, which is still below the total energy gained in the process (-1.80 eV). In this case, the entropy promotes the desorption of the CO_2, resulting in ΔG_{des} = +0.31 eV only.

3.3.2 Step 2 – Surface Re-oxidation.

The capture and incorporation of oxygen into the zirconia surface considering a single O vacancy follows the process:[272]

dissociation	$O_{2,(g)} + 2e^- \rightarrow O_2^{2-}{}_{ads} \rightarrow 2\ O^-_{ads}$
incorporation	$2\ O^-_{ads} + Vo \rightarrow O^{2-}_{latt} + O_{ads}$

First, the O_2 molecule forms a surface peroxide (O_2^{2-}) by capturing the excess electrons from Au deriving from the presence of the O vacancy. The charge transfer to O_2 has not been detected by EPR analysis on reduced and clean zirconia (without deposited Au particles) at

room temperature.[273] This suggests that it is the Au particle which promotes the activation and dissociation of the O_2 molecule by charge transfer. The formation of O_2^{2-} is also identified computationally when atomic oxygen is adsorbed on top of a lattice oxygen on a clean MgO surface,[274] or equivalently, the adsorption of an O_2 molecule on a surface O vacancy, as also shown for O_2 on reduced TiO_{2-x}.[275,276] Catlow et al. reported instead the preferred formation of the superoxide (O_2^-) on the O vacancies of Y-stabilized ZrO_2, from DFT calculations.[272] However, in our system the O_2^{2-} species were more stable than O_2^- by 1.59 eV, in agreement with the observations on TiO_2.[275]

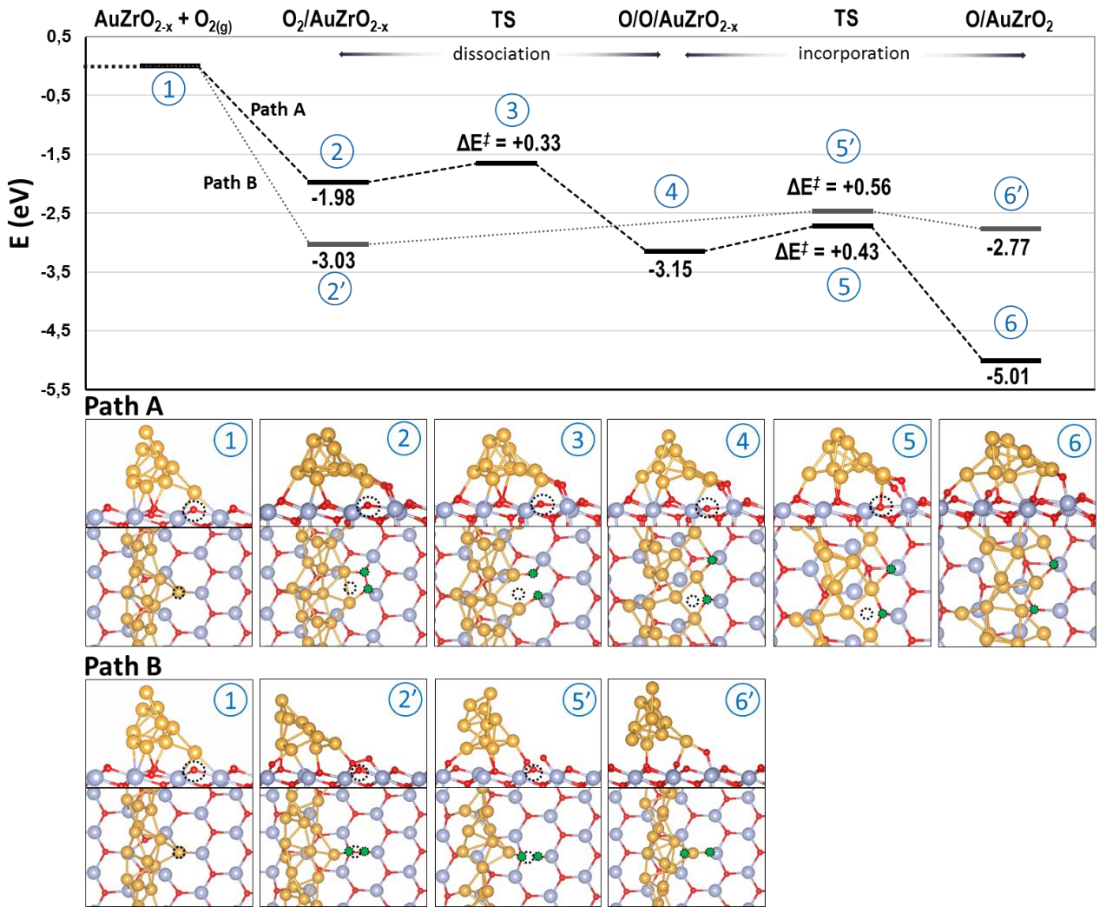

Figure 4.16. (top) Reaction energy profile and (bottom) side and top views of the structures of the surface reoxidation process with O_2 from the gas phase. The adsorbed O_2 molecule is indicated with green filled circles, and the O vacancy with a dotted circle. Zr is represented by big blue atoms, O by small red atoms, and Au by big golden atoms.

The reaction profile for this process and the optimized structures are shown in Figure 4.16. The O_2 molecule was first adsorbed at the Au/ZrO_2 interface (structure 2 of path A), with Bader charges -1.20 |e| on the peroxide and -0.32 |e| on Au. The O-O bond is enlarged to 1.50 Å (from 1.23 Å in O_2 gas). Increasing the charge transfer to oxygen, the bond was weakened until it dissociated into two O^- ions separated by 3.30 Å (structure 4 of path A). The Bader charges were -0.99 |e| on both O^- species, and +0.39 |e| on Au. Molina et al. reported qualitatively the same charge transfer process for Au supported on MgO and TiO_2 to activate and dissociate O_2 at the interface.[263] Next, one O^- moves toward the vacancy and refills it as a O_{latt} site (O^{2-} incorporation), while the other remains adsorbed at the interface (structure 6 of path A,). The Bader charge on the adsorbed oxygen was -1.04 |e| and +0.55 |e| on Au, meaning that, on the stoichiometric surface, the atomic oxygen at the interface is reduced by Au.

The reoxidation of the surface is a very exothermic process. The O_2^{2-} species is adsorbed with a binding energy of -1.98 eV (ΔG_{ads} = -1.35 eV), and dissociates into two O^- ions with an energy gain of 1.17 eV. The calculated energy barrier for this dissociation step is 0.33 eV. The following incorporation step implies an energy gain of 1.86 eV, involving a small barrier (+0.43 eV). While Behm et al. also observed experimentally an activated process for the CO oxidation step, they found the reoxidation of the TiO_{2-x} surface to be temperature independent, i.e. a non-activated process.[33] Most likely, under working conditions the catalysts contain a significant concentration of surface O vacancies such that the O_2 gas can directly adsorb and dissociate on two neighboring vacancies with a barrierless process. Here, we have considered only a single O vacancy in the reoxidation process. We expect that in the presence of a higher concentration of vacancies, and in particular on a pair of adjacent vacancies, the O_2 molecule can dissociate barrierless and regenerate the catalyst, closing the cycle.

For the adsorption of O_2 (and formation of O_2^{2-}) at the Au/ZrO_2 interface (dissociation step), we found a more stable isomer, with a binding energy of -3.03 eV. In this isomer, the O_2 molecule is oriented perpendicular to the Au nanorod and with an activated O–O bond length of 1.49 Å (structure 2' of path B). However, the calculated path B for the refilling of the vacancy does not completely dissociate the O_2 molecule. Once the vacancy is refilled, the O-O bond length is still 2.80 Å (structure 6' of path B). The calculated energy barrier is 0.56 eV, higher than that of path A, and the overall process is endothermic, with an energy cost of 0.38 eV. Therefore, this reaction path was not considered as a starting point for the second CO oxidation step.

3.3.3 Step 3 – Second CO Oxidation by Adsorbed Oxygen.

In order to close the catalytic cycle, the O^- species that remained adsorbed near the Au/ZrO_2 perimeter becomes the active oxygen for the oxidation of a second CO molecule. The new CO molecule was adsorbed on top of a Zr site adjacent to the O^- ion, and bridging two Au atoms (structure 2 of Figure 4.17). It was adsorbed with a binding energy of -1.37 eV (ΔG_{ads} = -0.76 eV), similar to the first CO oxidation step (-1.44 eV). The C-O bond is only slightly activated, with 1.18 Å of bond length (1.14 Å in the gas phase), and a Bader charge of -0.17 |e|. Next, the CO molecule approached the active oxygen to form a new CO_2 molecule, which was adsorbed and activated with a C-O bond distance of 1.29 Å, an OCO angle of 129.9º, and a Bader charge of -0.67 |e| (structure 4). The formation of CO_2 is slightly endothermic (ΔE = +0.02 eV). This can be attributed to the high stability of the O^- ion at the Au/ZrO_2 interface (where it was calculated to bind by -1.59 eV). In addition, Au nanoparticles on stoichiometric ZrO_2 are not activating the CO_2 molecule.[271] This is in contrast with the exothermic formation of CO_2 in the first step (ΔE = -0.36 eV), in which the final CO_2 molecule was adsorbed instead on top of an O vacancy. The product is finally desorbed with an energy cost of 0.69 eV (ΔG_{des} = +0.03 eV), leaving the Au/ZrO_2 catalyst in the initial structure (structure 5).

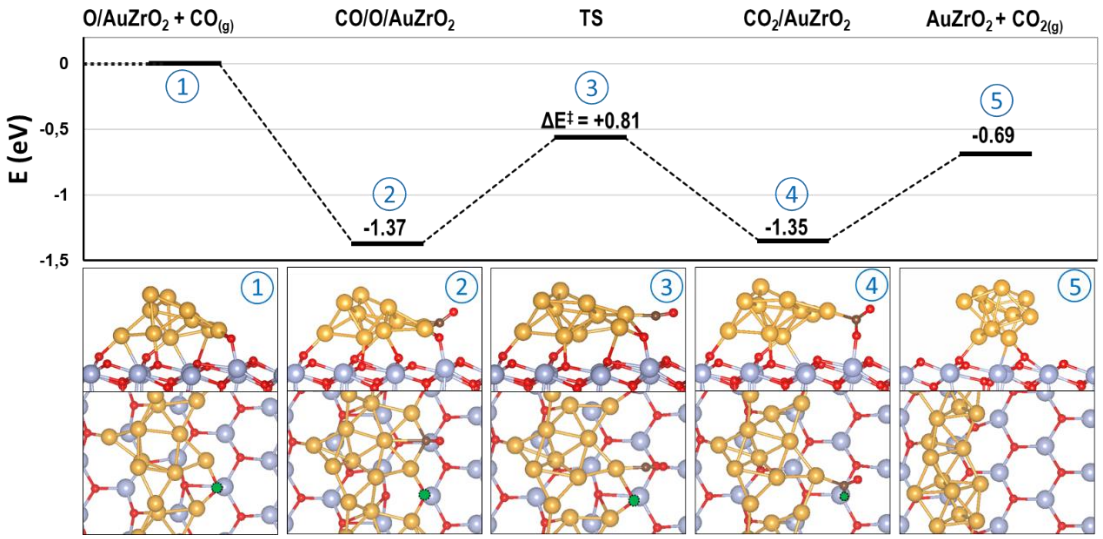

Figure 4.17. (top) Reaction energy profile and (bottom) side and top views of the structures of the second CO oxidation reaction with an adsorbed O^- ion. The O^- ion is indicated with a green filled circle. Zr is represented by blue atoms, O by red atoms, Au by golden atoms, and C by brown atoms.

Surprisingly, the calculated energy barrier for this process, +0.81 eV, is practically the same as for CO oxidation by a lattice oxygen (+0.79 eV). This suggests that LH, in which CO is

oxidized by an oxygen rich Au/ZrO_2 interface, and Au-assisted MvK mechanisms may exhibit similar thermodynamics and kinetics for the CO oxidation reaction.

Thus, the Au-assisted MvK is then a plausible mechanism for the CO oxidation reaction on the Au/ZrO_2 catalyst, and the key aspect resides in the higher surface reducibility (formation of O vacancies) at the metal-oxide interface sites. These results show that the catalytic activity of ZrO_2-supported Au in the CO oxidation reaction cannot be directly correlated to the bulk reducibility of the oxide. The lower catalytic activity in this reaction experimentally observed in Au/ZrO_2 compared to other reducible oxides can be attributed to higher reaction barriers (~0.8 eV), but also to factors like the high tendency of ZrO_2 to form carbonates on the surface by reaction with the generated CO_2, which limits the reoxidation (catalyst deactivation). Also, it is important to mention that the similar thermodynamics and energy barriers in the reaction of CO either with a lattice oxygen or with an adsorbed one indicate that probably both LH and MvK mechanisms can occur at room temperature and above.

Chapter Summary

In this chapter, we have investigated the effect of the metal-oxide interface on the chemistry of metal particles deposited on a zirconia surface. This study has been divided in three topics: (1) the study of the bonding properties of Au and Ag clusters on the t-ZrO_2 (101) stoichiometric surface, (2) on the O-deficient, N- and Nb-doped (101) surface, and (3) the study of the catalytic cycle of the CO oxidation reaction on a t-ZrO_2-supported Au particle.

We deposited Au and Ag single atoms and tetramers on a the stoichiometric (101) surface of t-ZrO_2. In the calculations, different approaches to account for the long-range dispersion forces were considered: PBE+D2, PBE+D2', and the optB86b-vdW density functional. We found that upon inclusion of dispersion forces, the relative stability of the various Au_4 and Ag_4 isomers changes. Also, the binding energies of the atoms and tetramers are significantly increased. This suggests that the bonding nature of neutral Au and Ag clusters on t-ZrO_2 is characterized by a significant contribution of vdW interactions. The highest correction was obtained with the PBE+D2 approach, and the smallest was obtained with the optB86b-vdW density functional. Thus, this problem has to be considered when the global minimum of supported clusters is searched, as the most stable isomer might be a function not only of the exchange-correlation functional but also of the approach to account for vdW forces.

Then, we have investigated the effect of a neutral O vacancy, N and Nb dopants in the (101) surface of t-ZrO_2 on the adsorption properties of Au_n and Ag_n clusters (n = 1,4,5). We found that surface O vacancies reduce both Au and Ag single atoms and Both Au_4 and Ag_4 clusters. Subsurface O vacancies reduce only Au and Ag atoms and the Au_5 cluster. The different reactivities can be rationalized by the open or closed shell nature of the atoms and clusters, and the higher reactivity of surface vacancies compared to those subsurface. Also, the charge transfer process enhances their binding energies. This effect may be exploited to reduce sintering, and charging negatively can be used to bind electrophilic species like O_2 and CO_2.

Substitutional N-doping in t-ZrO_2 is always found to induce a charge transfer from the Au and Ag particles to the oxide. N-doping results in low-lying and empty N 2p gap states that act as electron acceptors, so metal clusters are oxidized by simply deposition on the surface, reducing N^{2-} ions to N^{3-}. As expected, the binding energies are also increased with respect to the stoichiometric and non-defective ZrO_2 surface. On the other hand, substitutional Nb-doping results in high-lying and occupied Nb 4d gap states. However, these states are so high in energy that are never transferred to the deposited particles. The binding energies are even

weakened due probably to an electronic repulsion between the unpaired electron in Nb^{5+} and the clusters.

These results show the potential effect that defects and dopants can have on the adsorption properties of metal atoms and clusters. However, the occurrence and direction of the charge transfer is not easy to predict. It depends on several factors, like the number of atoms of the clusters leading to open or closed shell electronic configurations (recall that these clusters are in a nonscalable regime), and on the position of the defects in the lattice (surface or subsurface). In general, the control of defects and dopants offers a wide range of possibilities to modify the properties of the deposited particles.

Finally, we have investigated the activity of a Au/ZrO_2 catalyst in the CO oxidation reaction. We have calculated the complete reaction energy path of a Mars van-Krevelen mechanism. First, the CO molecule, adsorbed on Au, reacts with a lattice oxygen at the interface to form CO_2. It is exothermic by -0.83 eV and goes through an energy barrier of 0.79 eV. Then, gas O_2 refills the O vacancy generated, leaving an extra O atom adsorbed at the interface. This process passes through a barrier of 0.43 eV. Finally, the adsorbed O atom oxidizes a second CO molecule, with a barrier of 0.81 eV and a reaction energy of -0.69 eV. Thus, we can suggest that the MvK is a plausible mechanism on the Au/ZrO_2 catalyst. The key aspect resides in the higher reducibility of ZrO_2 at the $Au\text{-}ZrO_2$ interface sites. In particular, the formation energy of the vacancies is reduced from around +6 eV in the clean surface to +2.43 eV in the perimeter sites of Au. The great reduction of the formation energies at these sites can be rationalized by two aspects: (1) there is a structural rearrangement of the Au particle in which a Au atom moves to refill the vacancy. (2) The Au particle acts as an electron scavenger, as the extra charge associated to the O vacancy is totally transferred to Au rather than to the ZrO_2 surface.

With these results, we demonstrate the positive effect of a metal-oxide interface in the catalytic activity of the entire catalyst, as it can change the chemistry of both the deposited metal particles, for instance by charge transfer processes, and the supporting oxide, for instance by the activation of the oxide sites at the metal perimeter.

Chapter 5

Metal-Oxide Interface on Nanostructured Zirconia

1 Metal-Supported ZrO_2 Thin Films[7]

1.1 Introduction

It has been shown that ZrO_2 nanoparticles, a form of 0D nanostructuring, exhibit a completely different behavior compared to the bulk counterpart in both the formation of O vacancies and the dissociation of the H_2 molecule (Chapter 3). In this section, we consider another form of nanostructured oxide: zirconia ultrathin films. Ultrathin films are 2D materials that, once grown on a substrate, may exhibit properties completely different from their bulk (3D) and discrete (0D) counterparts.

A 2D phase of zirconia does not exist in nature. However, Pt_3Zr- and Pt-supported ZrO_2 2D films have been prepared and characterized experimentally. Pt_3Zr shows a strong chemical ordering and stability (superalloy),[277,278] where the reactive Zr atoms are in a lower concentration. This permits to oxidize them slowly and form well-ordered ZrO_2 monolayer films.[279,280,281] After oxidation of the surface Zr atoms, the first layer of the Pt_3Zr substrate is composed by only Pt atoms; the second one is already an ordered alloy. To prepare the ZrO_2/Pt film, metallic Zr is evaporated onto Pt under O_2. This method, however, results in an inhomogeneous coverage of the Pt surface with the zirconia film.[282,283,284,285] Nonetheless, we mention that preparing ZrO_2 films on Pt_3Zr and Pt surfaces is a clean alternative to the direct oxidation of metallic Zr, as the problems of sulfur and chlorine contaminants present in Zr surfaces[286] and the production of ZrO_x suboxides ($x < 2$)[287,288] is avoided.

[7] The content of this section is published in A. Ruiz-Puigdollers, G. Pacchioni. Reducibility of ZrO_2/Pt_3Zr and ZrO_2/Pt 2D Films Compared to Bulk Zirconia: A DFT+U Study of Oxygen Removal and H_2 Adsorption. *Nanoscale* 2017, 9, 6866.

Here, we studied how the reducibility of zirconia, in terms of O vacancy creation and H_2 dissociation, changes when it is nanoscaled down to a free-standing and to a supported monolayer on the (0001) surface of the Pt_3Zr alloy, and on the (111) surface of pure Pt. Our free-standing ZrO_2 thin films are models to study the role of the 2D nanostructuring in the reducibility of zirconia without the interaction of a metal substrate.

Computational Methods

The (101) zirconia surface was modeled by a 5-layer slab (5 ML) of a 3 × 2 supercell ($Zr_{60}O_{120}$). The free-standing ZrO_2 thin film was modeled by a monolayer of a (4x4) supercell with (101) orientation (denoted here as ZrO_2 1 ML). The lattice parameter was optimized with a 2 × 2 × 1 *k*-point grid (a_0 = 3.352 Å).

Bulk Pt_3Zr was optimized in a (1x1) unit cell of the $D0_{24}$ spatial group (see structure details in Ref. 279), with a 11 × 11 × 11 *k*-point grid. The optimized parameters a_0 = 5.667 Å and c_0 = 9.258 Å are in good agreement with the experimental ones (a_0 = 5.624 Å and c_0 = 9.213 Å).[289] The ZrO_2 thin film (1 ML) was deposited on a 5-layer (3x3) supercell of the Pt-terminated (0001) Pt_3Zr surface, and optimized with a 2 × 2 × 1 grid.

Bulk Pt was optimized in a (1x1) unit cell of a face-centered cubic structure, with a 11 × 11 × 11 *k*-point grid. The optimized parameter a_0 = 2.778 Å is in perfect agreement with experiment, 2.775 Å.[210] In order to study the effect of strain in the ZrO_2/Pt interface, the ZrO_2 1 ML was deposited on a 5-layer (5x5) and (√19x√19)*R*23.4º supercells of the Pt (111) surface. On the (5x5) supercell the *k*-point sampling was performed on a 2 × 2 × 1 grid, while *Γ*-point was used on the bigger (√19x√19)*R*23.4º supercell. The oxide cell parameter was adapted to that of the metal substrate.

The stability of the deposited ZrO_2 thin films was quantified by calculating the adhesion energy defined according to (1)[283]

$$E_{adh} = [E(ZrO_2/M) - E(M) - n_{ZrO_2}E(ZrO_{2,bulk})] \,/\, A \qquad (1)$$

where $E(ZrO_2/M)$ is the total energy of the supported ZrO_2 thin film, $E(M)$ the total energy of the metal slab, n_{ZrO2} the number of ZrO_2 units in the film, $E(ZrO_{2,bulk})$ the total energy of bulk zirconia per ZrO_2 unit, and A the area of the ZrO_2/M cell.

The energy values reported do not include the entropic terms. These can be neglected in solid surfaces. The stretching frequencies of the OH and ZrH bonds, ~3600 cm^{-1} and ~1300 cm^{-1}, respectively, yield entropic terms for the H_2ZrO_2/M systems lower than 10^{-5} eV, and

zero-point energies of 0.2 eV (OH bonds) and 0.1 eV (ZrH bonds). These values do not change the general conclusions based on the analysis of the DFT total energies.

1.2 Stoichiometric ZrO_2 Thin Films

1.2.1 Free-Standing Thin Films

The relaxation of the cell parameter in the ZrO_2 (101) 5 ML slab, representative of the zirconia extended surface, is negligible with respect to that of bulk ZrO_2. The strain introduced is almost zero. The Zr-O bonds in the first monolayer are 2.300 Å and 2.222 Å, while in bulk ZrO_2 are 2.346 Å and 2.150 Å. A different situation is observed when we consider 1 ML of zirconia. The free-standing zirconia film contracts to a cell parameter of 3.352 Å, Table 5.1, due to the undercoordination (the coordination of Zr and O ions decreases from 8 and 4 in bulk to 4 and 3 in the monolayer, respectively). All Zr-O bond distances contract to 2.158 Å. Fixing the cell parameter of the film to that of bulk (3.652 Å) results in a tensile strain of 8.2%, which lowers the stability and increases the reactivity, as it will be shown below.

Table 5.1 Cell parameter, a_0, tensile strain, top of the valence band, VB, bottom of the conduction band, CB, and band gap, E_{gap}, of bulk ZrO_2, ZrO_2 (101) surface, and ZrO_2 thin films. VB and CB edges are calculated with respect to the vacuum level.

system	a_0 (Å)	strain (%)	VB (eV)	CB (eV)	E_{gap} (eV)
Bulk ZrO_2	3.652	0	–	–	4.6
ZrO_2 (101) surface (5 ML)	3.652	~0[a]	-6.8	-2.6	4.2
ZrO_2 (101) thin film (1 ML)	3.652	+8.2	-5.0	-1.7	3.7
	3.352	0	-7.7	-2.8	4.9

[a]The relaxation of the parameters from those of the bulk is negligible in a 5 ML slab.

The calculated band gap, VB and CB edges for the stoichiometric (101) surface and 1ML zirconia are reported in Table 5.1. These values have been obtained from the Kohn-Sham eigenvalues and referred to the vacuum level. The band gap of bulk ZrO_2 is 4.6 eV, while that of the (101) 5 ML surface decreases to 4.2 eV due to the presence of surface. The zirconia 1 ML with fixed bulk cell parameter (+8.2% strain) shows an even smaller band gap (3.7 eV), originating from an important destabilization of the O 2p states that shifts the top of the VB to higher energies. When the 1 ML film is free to relax, the top of the VB decreases to -7.7 eV, and the bottom of the CB remains close to the value observed in the 5 ML slab model (-2.8 eV), increasing the band gap to 4.9 eV. This indicates that the free-standing ZrO_2 film, when relaxed, is expected to be even less reactive compared to the (101) extended surface.

1.2.2 Pt_3Zr- and Pt-Supported ZrO_2 Thin Films

Oxide-metal interfaces are strongly affected by the lattice mismatch between the oxide and the metal, resulting in a strain in one of the two components. Considering a calculated lattice parameter of 5.667 Å for the Pt_3Zr substrate and 3.352 Å for the relaxed ZrO_2 thin film, the non-rotated (5x5)/(3x3) supercell structure for the $ZrO_2/Pt_3Zr(0001)$ system implies a +1.4% lattice mismatch with a moderate tensile strain on the oxide, Table 5.2. Similarly, considering the calculated lattice parameter of pure Pt 2.778 Å, the non-rotated (4x4)/(5x5) supercell, named here supercell A, for the $ZrO_2/Pt_3(111)$ system introduced a tensile strain of +3.5% on the oxide. Other combinations of larger supercells may lead to a smaller lattice mismatch but can be treated only at very high, unaffordable computational effort.

Table 5.2 Cell parameters, a_0, metal-oxide interface distance, h, tensile strain on ZrO_2, adhesion energy, E_{adh}, work function, Φ, and charge transfer at the metal-oxide interface, Δq, of metal substrates and supported ZrO_2 thin films.

system	supercell	a_0 (Å)	h (Å)	strain	E_{adh}	Φ	Δq[a]
Pt_3Zr (0001)	(1x1)	5.667	–	–	–	5.31	–
$ZrO_2/Pt_3Zr(0001)$	(5x5)/(3x3)	17.000	3.619	+1.4	0.79	4.73	$+7.0\cdot10^{-4}$
Pt (111)	(1x1)	2.778	–	–	–	5.77	–
ZrO_2/Pt(111)-(**A**)	(4x4)/(5x5)	13.888	3.158	+3.5	0.78	4.92	$+3.4\cdot10^{-3}$
ZrO_2/Pt(111)-(**B**)	$(2\sqrt{3}x2\sqrt{3})$/ $(\sqrt{19}x\sqrt{19})R23.4^o$	12.107	3.027	+4.1	0.75	5.04	$+4.0\cdot10^{-3}$

[a] $\Delta q > 0$: Charge transfer from the oxide to the support.

For ZrO_2/Pt(111), Meinel et al. found by DFT calculations that the (4x4)/(5x5) interface is in fact the most stable one.[283] However, they observed by STM imaging and LEED techniques that this interface is stable only between 900 and 1000 K. Instead, the $(2\sqrt{3}x2\sqrt{3})/(\sqrt{19}x\sqrt{19})R23.4^o$ superstructure is preferred for growing zirconia on Pt.[283-285] Therefore, we also considered the $(\sqrt{19}x\sqrt{19})R23.4^o$ supercell for the Pt (111) substrate, in the following referred to as supercell B. Here, a +4.1% of tensile strain exists on the $(2\sqrt{3}x2\sqrt{3})$ oxide supercell.

For the ZrO_2/Pt_3Zr interface, the $(\sqrt{19}x\sqrt{19})R23.4^o$ supercell was also found experimentally by Antlanger et al.[279] In our $ZrO_2/Pt_3Zr(0001)$ model, this supercell resulted instead in an expansive strain of +6% on the oxide. The difference between our model and the experiment is due to the fact that in the experiment there is a contraction of the first Pt layer,[283] which attenuates the expansion in the ZrO_2 thin film. Furthermore, the formation of ZrO_2 2D islands

also helps in releasing the strain.[279] These effects cannot be included in a simple way in our periodic slab models. The 6% strain on our ZrO_2 film led to a large, unphysical, structural rearrangement such that the film loses the atomic ordering of the (101) zirconia surface. For this reason, this model was no investigated.

The structures of the ZrO_2 thin film deposited on Pt-terminated Pt_3Zr (0001) and Pt (111) surfaces are shown in Figure 5.1. On the Pt_3Zr support, with the lowest strain (+1.4%), the ZrO_2 film keeps the (101) structure almost unchanged, Figure 5.1a. On the Pt (111) surface, the strain leads to structural distortions in the direction normal to the surface rather than in the surface plane, as it can be seen comparing the top and side views of their structures, Figures 5.1(b,c). The oxide Zr atoms in a hollow site over three Pt atoms, move down to a Pt-Zr_{oxide} distance of 3.01 Å in supercell A, and to 2.98 Å in supercell B. The Zr atoms on top of the Pt atoms stay instead at a distance of around 3.7 Å. Thus, due to the periodicity of the Pt-Zr bonds, the Zr layer undergoes a wave-like distortion, which can be appreciated in Figures 5.1(b,c). The out-of-plane buckling of the Zr layer and the in-plane atomic ordering of the (101) ZrO_2 surface were observed experimentally in ZrO_2/Pt(111) films.[283] A vertical distortion was also seen in $ZrO_2/Pt_3Zr(0001)$[279] in contrast to our findings, probably due to an experimental strain larger than our +1.4%.

The film oxide binds closer the metal substrate when the strain is larger, Table 5.2. The metal-oxide separation, calculated as an average Pt-Zr_{oxide} distance, is 3.619 Å on Pt_3Zr (+1.4% strain), 3.158 Å on Pt with supercell A (+3.5% strain), and 3.027 Å on Pt with supercell B (+4.1% strain). The trend is due to the tensile nature of the strain: longer Zr-O bond distances in the film reduce the effective coordination of the oxide atoms, which is compensated by a shorter bonding to the underlying substrate.

According to the calculated Bader charges, in ZrO_2/Pt_3Zr, the oxide transfers 0.20 |e| to the substrate, or equivalently, $7.0 \cdot 10^{-4}$ |e|/Å^2. The charge is delocalized on the Pt_3Zr substrate such that the Pt atoms have a charge of -0.6|e| and +1.8|e| the Zr atoms, in average. In the supercell A of ZrO_2/Pt, the oxide transfers 0.66 |e|, or $3.4 \cdot 10^{-3}$ |e|/Å^2; in supercell B, it transfers 0.58 |e|, or $4.0 \cdot 10^{-3}$ |e|/Å^2, Table 5.2. Not surprisingly, shorter metal-oxide distances result in a higher charge transfer.

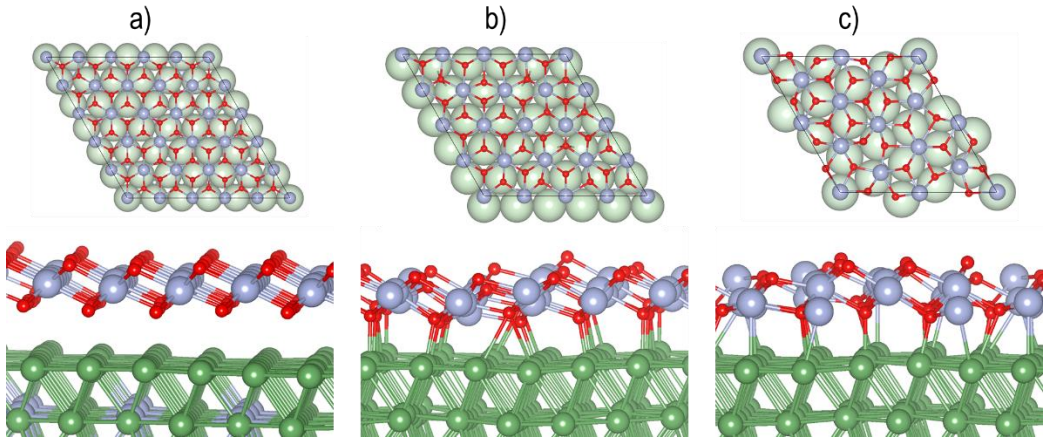

Figure 5.2 (bottom) Side and (top) top views of a ZrO_2 ultrathin film supported on (a) $Pt_3Zr(0001)$ (3x3) supercell, (b) Pt(111) (5x5) supercell (A), and (c) Pt(111) ($\sqrt{19}$x$\sqrt{19}$)*R*23.4º supercell (B). Zr is represented by big blue atoms, O by small red atoms, and Pt by big green atoms.

The ZrO_2 film binds with an adhesion energy of 0.79 J/m^2 (49.3 meV/Å^2) on the Pt-terminated Pt_3Zr (0001) surface, 0.78 J/m^2 (48.7 meV/Å^2) on the Pt (111) surface in the supercell A, and 0.75 J/m^2 (46.8 meV/Å^2) in the supercell B, Table 5.2. The definition of the adhesion energy takes into account the change in surface energy of the metal, the cost to create an interface, and the strain supported by the oxide. The first term can be considered the same in the three systems since the substrate is, in each case, a monolayer of Pt (111) bound to ZrO_2. Then, the interface energy is mainly due to the charge transfer that enhances the bonding of the film. In turn, this correlates with larger strains on the oxide, which instead destabilizes the formation of a metal-oxide interface, opposing the favorable charge transfer interaction. The final result is a similar adhesion energy in the three cases.

The charge transfer at the metal-oxide interface can be understood on the basis of the positions of the metal Fermi level and the top of the oxide VB. As reported in Table 5.1, the top of the VB of the free-standing ZrO_2 film is at -7.7 eV. The Fermi level of Pt_3Zr and Pt falls at -5.31 and -5.77 eV, respectively, equivalent to -Φ in Table 5.2. In the interacting metal-oxide system, the lattice mismatch destabilizes the oxide states so that are pushed above the metal Fermi level resulting in an oxide-to-metal charge transfer. The final work function decreases with respect to the bare metal due to the charge separation that creates a surface dipole pointing towards the oxide. On Pt_3Zr, Φ decreases to 4.73 eV ($\Delta\Phi$ = -0.58 eV), in the supercell A of Pt Φ decreases to 4.92 eV ($\Delta\Phi$ = -0.85 eV), and in supercell B to 5.04 eV ($\Delta\Phi$ = -0.73 eV), Table 5.2. For comparison, Qi et al. found experimentally a work function of 5.05

eV for ultrathin films of ZrO_2 on a ($\sqrt{19}$x$\sqrt{19}$)*R*23.4º supercell of Pt(111),[290] which fits with our result.

In Figure 5.2 we report the Projected Density of States (PDOS) of the three 2D films studied. Their electronic structure is mainly affected by the metal-oxide distance, i.e. by the chemical hybridization between the metal surface density and the oxide film states. The supercell B of the ZrO_2/Pt system, with the shortest metal-oxide distance (stronger chemical bond), shows more pronounced MIGS in the oxide band gap. Also, wider ZrO_2 valence and conduction bands can be appreciated. In turn, the widening of the oxide bands decreases the band gap, from ~4 eV in ZrO_2/Pt_3Zr, Figure 5.2a, to ~3 eV in ZrO_2/Pt, Figure 5.2c.

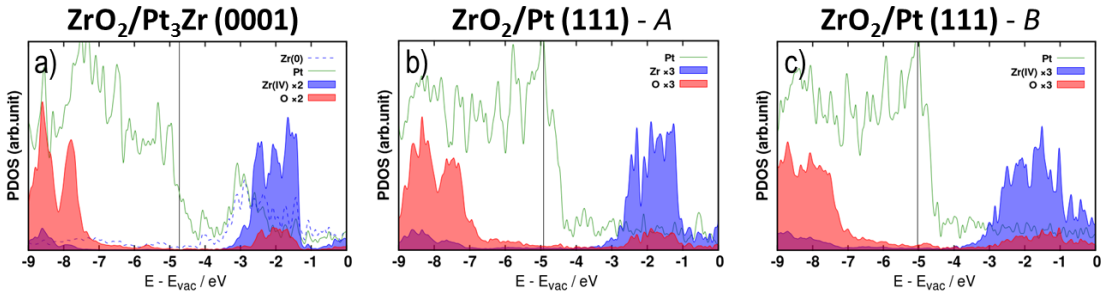

Figure 5.2 Projected Density of States (PDOS) of a ZrO_2 2D film supported on (a) Pt_3Zr (0001) (3x3) supercell, (b) Pt(111) (5x5) supercell A, and (c) Pt (111) ($\sqrt{19}$x$\sqrt{19}$)*R*23.4º supercell B. The zero of energy corresponds to the vacuum level.

1.3 Oxygen Deficient ZrO_{2-x} Thin Films

1.3.1 Free-Standing ZrO_{2-x} Thin Films.

The formation of a neutral O vacancy in bulk zirconia has a calculated energy cost of 6.16 eV, Table 5.3. The cost is slightly lowered to 6.03 eV when the vacancy is created on the (101) surface. However, this increases to 6.71 eV on the relaxed ZrO_2 1ML film because of the lattice contraction, which gives shorter and stronger Zr-O bonds. In fact, an O vacancy in the strained film, with the lattice expanded by 8.2%, has a formation energy of 3.50 eV only. This confirms the important role of the lattice strain in the removal of O ions from the thin film.

The extra electrons associated to the defect are localized in the vacancy site in a singlet state rather than in reduced Zr^{3+} centers, typical of nonreducible oxides. This holds true for all systems, despite the lower coordination of the Zr ions on the surface and in the film. The gap state associated to the defect appears in the same energy range in the two models, surface (5 ML) and thin film (1 ML), at 3.3 and 3.2 eV, respectively, from the top of the VB.

Table 5.3 Formation energy, $E_{f,Vo}$, and position of the gap state with respect to the top of the valence band, E_{GS}, of a neutral O vacancy in ZrO_2 bulk, (101) surface, and thin films.

system	$E_{f,Vo}$ (eV)	E_{GS} (eV)
ZrO_{2-x} bulk	6.16	2.7
ZrO_{2-x} (101) surface (5 ML)	6.03	3.3
ZrO_{2-x} (101) thin film (1 ML) relaxed	6.71	3.2
ZrO_{2-x} (101) thin film (1 ML) 8.2% strained	3.50	1.9

1.3.2 Pt_3Zr- and Pt-Supported ZrO_{2-x} Thin Films

In the supported ZrO_2 thin films, we observed a local deformation of the lattice around the O vacancy created. The nearest Zr and O ions move down, creating a depression in the oxide surface, Figure 5.3. A O_{3c} vacancy in the Pt_3Zr-supported ZrO_2 film costs 3.28 eV in the top layer, and 2.92 eV at the interface layer, Table 5.4. This is about half the cost of creating a vacancy in the bulk or on the (101) surface of zirconia, clearly indicating the role of the underlying metal support. In the Pt-supported film (supercell A), top O_{3c} and interface O_{4c} vacancies cost 0.95 and 1.17 eV, respectively. In the supercell B, the initially created top and interface O vacancies evolve to the same unique structure after the geometry optimization, due to a large strain-induced structural deformation, Figure 5.3e. The formation energy of the vacancy in this case is +2.23 eV. Note that there are several possible non-equivalent O atoms to remove from the film due to the partial loss of crystallinity, Figure 5.1c, so that we cannot exclude that there are other O atoms easier to remove.

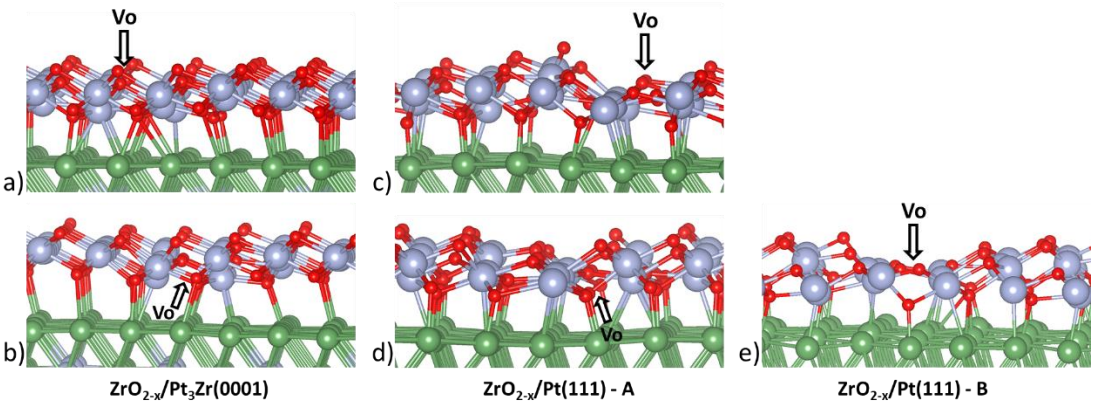

Figure 5.3 Structures of a ZrO_{2-x} ultrathin film supported on (a,b) $Pt_3Zr(0001)$ (3x3) supercell, (c,d) Pt(111) (5x5) supercell (A), and (e) Pt(111) ($\sqrt{19}$x$\sqrt{19}$)*R*23.4º supercell (B). Pt: green; Zr: blue ; O: red. The vacancy is indicated with an arrow.

Table 5.4 Formation energy, $E_{f,Vo}$, change in work function, $\Delta\Phi$, and charge transfer at the metal-oxide interface, Δq, of a neutral O vacancy in Pt_3Zr- and Pt-supported ZrO_{2-x} thin film.

system		$E_{f,Vo}$ (eV)	$\Delta\Phi$ (eV)	Δq (|e|/Å^2)
$ZrO_{2-x}/Pt_3Zr(0001)$	$V_{O,top}$	+3.28	-0.05	$+4.5\cdot10^{-3}$
	$V_{O,interface}$	+2.92	-0.13	$+4.5\cdot10^{-3}$
ZrO_{2-x}/Pt(111)-(**A**)	$V_{O,top}$	+0.95	+0.05	$+9.3\cdot10^{-3}$
	$V_{O,interface}$	+1.17	-0.23	$+8.8\cdot10^{-3}$
ZrO_{2-x}/Pt(111)-(**B**)		+2.23	-0.05	$+1.2\cdot10^{-2}$

In all cases considered, the extra charge associated to the O vacancy is transferred to the Fermi level of the metal substrate. According to the Bader charges, the ZrO_2 thin film transfers 1.3 |e| to Pt_3Zr, equivalent to $4.5\cdot10^{-3}$ |e|/Å^2, 1.7-1.8 |e| to the Pt support in supercell A ($8.8\text{-}9.3\cdot10^{-3}$ |e|/Å^2), and 1.7 |e| ($1.2\cdot10^{-2}$ |e|/Å^2) in supercell B. Shorter interface distances result in a larger charge transfer. Despite the charge transfer, Φ does not change substantially, with a moderate decrease with respect to the stoichiometric film.

The enhanced stability of the O vacancies in the supported thin film compared to zirconia bulk and surfaces is thus the result of two contributions: the electron transfer from the cavity to the metal Fermi level (dominant) and the local structural relaxation around the vacancy. The metal substrate acts as an electron scavenger, accepting the extra charge from the O vacancies. So, the presence of the ZrO_2/Pt_3Zr or ZrO_2/Pt interface promotes the formation of this defect. Note that the same conclusion was found en the previous section §4.3, where the formation of a Au/ZrO_2 interface via deposition of Au nanoparticles enhanced the creation of O vacancies at the interface, thus favoring the direct oxidation of CO by lattice oxygen.

1.4 H_2 Adsorption on Stoichiometric ZrO_2 Thin Films

1.4.1 Free-Standing ZrO_2 Thin Films

On the ZrO_2 (101) surface, H_2 was adsorbed and dissociated through a (nonreductive) heterolytic mechanism with an adsorption energy of -0.06 eV. The (reductive) homolytic splitting was instead found to be very endothermic, with an energy of +2.18 eV (see section §3.4). If we consider the unsupported oxide thin film (exhibiting O_{3c} and Zr_{6c} sites), it is suprisingly even less reactive toward hydrogen than the (101) surface, Table 5.5. H_2 dissociates heterolytically with an energy of +1.55 eV, and homolytically with an energy of +3.40 eV, Figures 5.4(c,d). This is a consequence of the lattice contraction. In fact, if H_2 is adsorbed on the 8.2% strained ZrO_2 thin film (with bulk lattice parameter), exothermic adsorption energies of -1.38 and -0.11 eV are found for the heterolytic and homolytic

dissociation, respectively. In any case, the heterolytic dissociation remains the preferred mechanism. This is different from what we obtained for 1 – 2 nm zirconia nanoparticles, which were instead reduced by H_2 (see sections §3.2 and §3.4). Thus, zirconia becomes a reducible oxide when nanostructured to a 0D form (nanoparticles), while 2D nanostructures like the unsupported thin film considered here, still maintains the low reducible character observed in the bulk regime. The reason is the following: the coordination of the Zr ions remains the same in 2D films and on the (101) surface, while a high ratio of low-coordinated Zr ions is present on the nanoparticles. The low-coordinated sites introduce new acceptor states in the band gap of the material that facilitate the stabilization of the excess of charge associated to the homolytic hydrogen splitting.

Table 5.5 Adsorption energy, E_{ads}, of a H_2 molecule on the ZrO_2 (101) surface and on the free-standing thin film.

System	Mechanism	E_{ads} (eV)
ZrO_2 (101) surface (5 ML)	Homolytic 2 HO_{3c}	+2.18
	Heterolytic HO_{3c} + HZr_{7c}	–0.04
ZrO_2 (101) thin film (1 ML) relaxed	Homolytic 2 HO_{3c}	+3.40
	Heterolytic HO_{3c} + HZr_{6c}	+1.55
ZrO_2 (101) thin film (1 ML) 8.2% strained	Homolytic 2 HO_{3c}	–1.38
	Heterolytic HO_{3c} + HZr_{6c}	–0.11

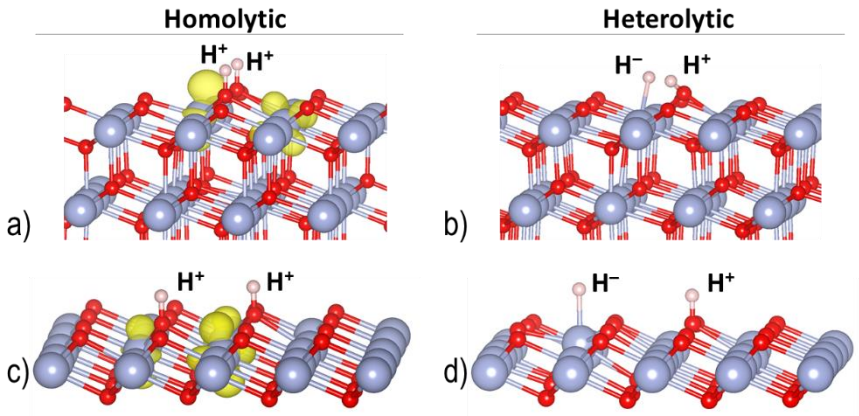

Figure 5.4 Structures of H_2 dissociated on the (a,b) ZrO_2 (101) surface (5ML slab), and on the (c,d) ZrO_2 ultrathin film (1ML), through (left) a homolytic and (right) a heterolytic mechanisms. Zr is represented by bug blue atoms, O by small red atoms, and H by small white atoms. The spin density, localized in Zr^{3+} sites, is shown in yellow (ρ_{iso} = 0.01 $e^-/Å^3$).

1.4.2 Pt_3Zr- and Pt-Supported ZrO_2 Thin Films

A completely different picture for H_2 dissociation emerges when the ZrO_2 film is supported on the Pt_3Zr and Pt metals. In all cases the homolytic dissociation becomes preferred, Table 5.6. On the $ZrO_2/Pt_3Zr(0001)$ surface, the H_2 molecule dissociates homolytically with an energy of -1.80 eV, and heterolytically with an energy of +0.88 eV. In the supercell A of $ZrO_2/Pt(111)$, also the homolytic H_2 dissociation is preferred with an energy of -1.34 eV, but the heterolytic is also exothermic (-0.30 eV). In the supercell B, H_2 is homolytically dissociated with an energy of -1.49 eV, and heterolytically with an energy of +0.15 eV. In short, we always observe a more favorable H_2 dissociation and a homolytic mechanism. The order of stability is reversed compared to the free-standing oxide film and to the extended bare surface.

Table 5.6 Adsorption energy, E_{ads}, change in work function, $\Delta\Phi$, and charges on oxide and support, q, for a H_2 molecule adsorbed Pt_3Zr- and Pt-supported ZrO_2 thin films.

system	mechanism	E_{ads} (eV)	$\Delta\Phi$(eV)	q_{ox} (|e|)	q_{sup} (|e|)
$ZrO_2/Pt_3Zr(0001)$	Homolytic 2 HO_{3c}	-1.80	-0.31	-0.8	-1.2
	Heterolytic HO_{3c} + HZr_{6c}	+0.88	+0.12	-0.3	-0.2
$ZrO_2/Pt(111)$-**(A)**	Homolytic 2 HO_{3c}	-1.34	-0.49	-0.4	-1.6
	Heterolytic HO_{3c} + HZr_{6c}	-0.30	+0.26	+0.3	-0.8
$ZrO_2/Pt(111)$-**(B)**	Homolytic 2 HO_{3c}	-1.49	-0.36	-0.5	-1.5
	Heterolytic HO_{3c} + HZr_{6c}	+0.15	+0.01	+0.1	-0.6

The enhanced reactivity of the supported thin ZrO_2 film has two origins: (a) the strained lattice, and (b) the possibility to stabilize charge via electron transfer to the metal support. The Bader charges are between -0.4 and -0.8 |e| on the hydroxylated oxide 2D film (homolytic dissociation), and between -1.2 and -1.6 |e| on the metal substrate, Table 5.6. This indicates that in the homolytic dissociation the charge transferred from hydrogen is delocalized partly on the metal support and partly on the oxide film, which becomes then reduced. The homolytic dissociation of H_2 decreases the work function by 0.3-0.5 eV due to a shift of the Fermi level and to the presence of positively charged adsorbates (H^+ ions). ZrO_2 thin films supported on Pt_3Zr and Pt are then systems that become reducible by simple exposure to hydrogen. This is due to the presence of a metal-oxide interface, rather than to only nanostructuring, as the non-supported thin film was not reduced by H_2. The interface enhances the reactivity of the thin film by the presence of metal acceptor states, as found for the O vacancies, and by the decay

of the oxide CB into the band gap (Zr 4d states that form the MIGS). Beside the electronic effects, the strain generated in the oxide by the lattice mismatch also enhances the reactivity, although this factor is much less important.

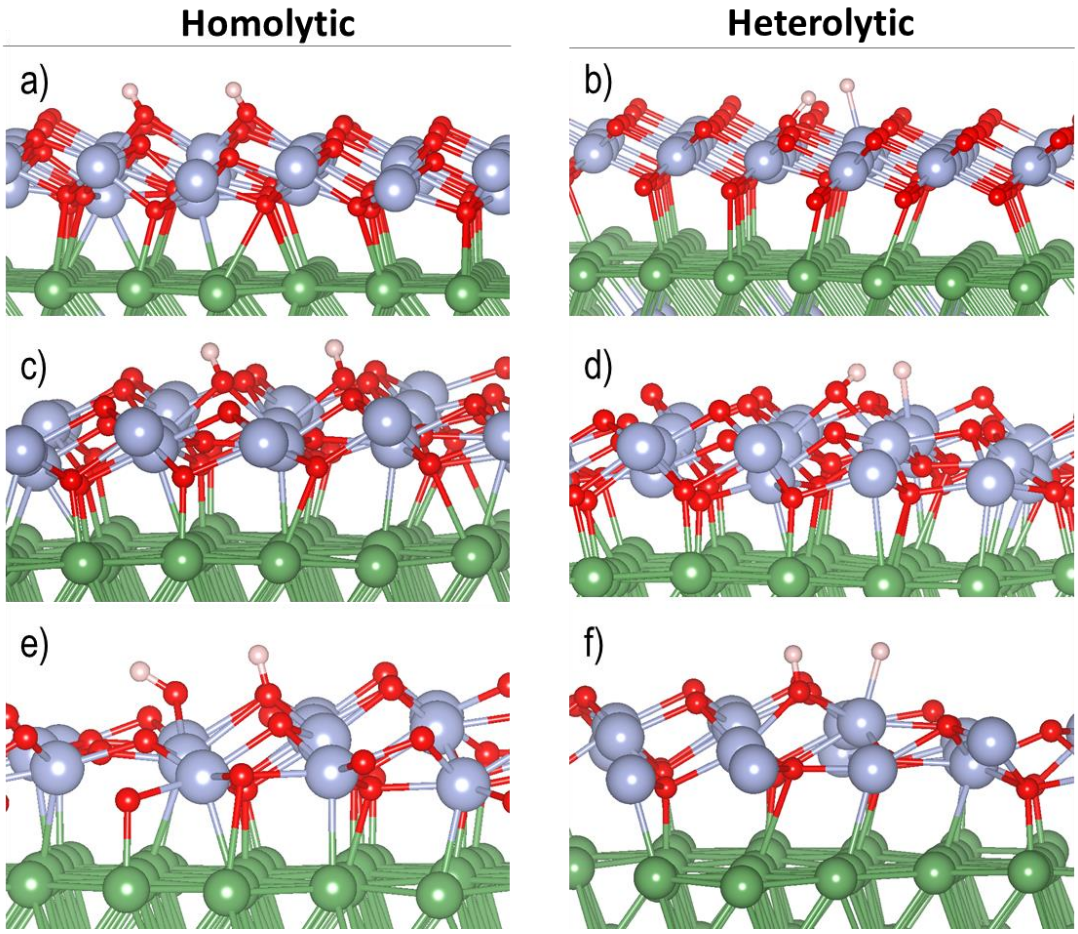

Figure 5.5 Structures of H_2 dissociated on the ZrO_2 ultrathin films supported on (a,b) the $Pt_3Zr(0001)$ (3x3) supercell, (c,d) the Pt(111) (5x5) supercell (A), and (e,f) the Pt(111) ($\sqrt{19}$x$\sqrt{19}$)*R*23.4º supercell (B), through a (left) homolytic and (right) heterolytic mechanisms. Zr is represented by big blue atoms, O by small red atoms, Pt by big green atoms, and H by small white atoms.

Finally, we considered the possible dissolution of hydrogen into the bulk of the metal support via diffusion of a single H atom across the ZrO_2 2D film. To this end, we have considered a single H atom adsorption on top of the oxide layer and at the metal/oxide interface. On top of a surface O site, H adsorbs preferentially an O site, Figure 5.6a, forming an OH group with an energy of -3.50 eV, Table 5.7 (computed with respect to ½ H_2). The charge provided by the H atom is partly localized on the metal substrate (-0.7 |e|) and on the

oxide film (-0.3 |e|); notice that 0.2 |e| were already transferred from ZrO_2 to Pt_3Zr, Table 5.2. On top of a Zr site, Figure 5.6b, a H^- ion is formed via charge transfer from the metal substrate (the charge on this becomes positive). However, this bonding mode is highly unfavorable (+1.48 eV). At the interface site, the H atom is adsorbed above a Pt_3 hollow site and near a subsurface Zr atom, Figure 5.6c, with an adsorption energy of -3.35 eV. In this case no charge transfer occurs, and the H maintains its atomic character and a magnetic moment equal to 1 (H^0). We also considered an interstitial site inside the oxide film. This structure was however unstable and it evolved to a H adsorbed on top of a surface O ion. This indicates the presence of an energy barrier to pass through the oxide film which, however, has not been investigated. The binding of H on top of the film is thus slightly more favorable than at the interface. Hydrogen diffusion to the metal-oxide interface is an activated process that depends on the H_2 partial pressure.

Table 5.7 Adsorption energy (with respect to ½ H_2), E_{ads}, change in work function, $\Delta\Phi$, and charge on H, oxide and metal support, q, of an adsorbed H atom on the Pt_3Zr supported ZrO_2 thin film.

site	E_{ads} (eV)	$\Delta\Phi$(eV)	q_H(|e|)	q_{ox}(|e|)	q_{sup}(|e|)
O top	-3.50	-0.15	+1.0	-0.3	-0.7
Zr top	+1.48	+0.41	-0.5	+0.2	+0.3
Interface	-3.35	0	0	+0.2	-0.2

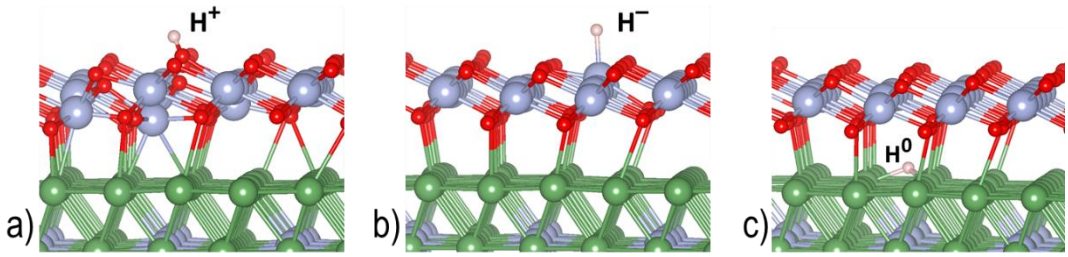

Figure 5.6 Structures of a H atom adsorbed on a $Pt_3Zr(0001)$ supported ZrO_2 ultrathin film. (a) On top of an O atom; (b) on top of a Zr atom; (c) at the metal-oxide interface. Zr is represented by big blue atoms, O by small red atoms, Pt by big green atoms, and H by small white atoms.

Chapter Summary

In summary, in this chapter we have considered both the nanostructuring of zirconia and the interface with an extended metal (inverse catalyst). We have investigated the formation of O vacancies and the dissociation of H_2 on a free-standing and Pt_3Zr- or Pt-supported ZrO_2 2D film.

The unsupported ZrO_2 film undergoes a strong lattice contraction with respect to the bulk lattice. This leads to an increase of the formation energies of O vacancies, from 6.16 eV in bulk to 6.71 in the film, and to a lower reactivity toward the dissociation of H_2, from an adsorption energy of -0.04 eV on the (101) surface to +1.55 eV on the film. So, the zirconia free-standing 2D film exhibits a non-reducible character like bulk zirconia (3D).

However, the thin films supported on the Pt_3Zr(0001) and Pt(111) metal surfaces become reducible. The formation energies of an O vacancy decrease to around +3 eV on ZrO_2/Pt_3Zr and to around +1 eV on ZrO_2/Pt. Also, the adsorption energy of H_2 is found to be -1.80 eV on ZrO_2/Pt_3Zr and -1.34 eV on ZrO_2/Pt, and always through a homolytic dissociation mechanism, which implies the reduction of the surface. The enhanced reducibility is attributed to the presence of the underlying metal that, as in the deposition of metal clusters on the oxide surface (§4.3), acts as electron scavenger capturing the extra charge from the O vacancies and the H_2 molecule.

Comparing the results between the free-standing thin film and that supported on the extended metals, it can be concluded that the key aspect to change the reducibility of the oxide has been the presence of the metal-oxide interface rather than the nanostructuring to a 2D film. Of course, by growing thicker oxide layers on the metal support, the usual surface properties of the oxide will be recovered.

Chapter 6

Conclusions

This thesis has investigated how the physical and chemical properties of zirconium dioxide can be affected by two different aspects: (1) by the nanostructuring to a zero-dimensional (nanoparticle) or to a two-dimensional (thin film) material, and (2) by the presence of a metal-oxide interface, either by depositing metal clusters on a zirconia surface or by depositing a zirconia thin film on a metal substrate. We specially focused on the changes of the oxide reducibility, a key property related to its catalytic activity.

When zirconia is nanostructured in the form of 1 – 2 nm nanoparticles, its chemical properties were drastically changed. (1) While bulk zirconia is a nonreducible oxide, it becomes reducible at the nanoscale. We observed this change by two mechanisms: by the easier dissociation of the H_2 molecule through a homolytic mechanism (which implies the formation of reduced Zr^{3+} centers), while on bulk it dissociates heterolytically, and by the easier formation of oxygen vacancies via both the direct removal of O atoms and the desorption of H_2O from the hydrogenated nanoparticle. (2) Also, the bonding properties of a Au single atom were notably improved in the nanoparticles. Au was oxidized or reduced by simply deposition on different sites, which in turn increased the binding energies. In contrast, bulk zirconia adsorbs a Au atom weakly and with no charge transfer at the interface.

The improved reducibility of nanostructured zirconia and its higher reactivity toward a Au atom are rationalized by the special physical properties that were observed only at the nanoscale. First, the undercoordination of the atoms in edges and corners of the nanoparticles gives rise to low-lying and occupied O 2p states (possible donors) and to high-lying and empty Zr 4d states (possible acceptors). In particular, the new Zr 4d gap states are responsible for a

higher reducibility of the oxide, as these can capture the extra charge associated to oxygen vacancies or the electrons of the H_2 molecule in a homolytic splitting. Similarly, the presence of O 2p and Zr 4d gap states resulted in charge transfer processes when Au was deposited on undercoordinated O and Zr sites. Second, nanoparticles are more flexible objects that, with a higher structural relaxation than bulk, can stabilize better adsorbates and vacancies in the lattice.

In addition, we have demonstrated that at the nanoscale, O deficient zirconia can exhibit a ferromagnetic behavior at room temperature. This is attributed to a sufficient number of low-coordinated Zr ions that are able to accommodate the excess charge in Zr^{3+} sites in a ferromagnetic ordering.

In general, nanostructuring oxides can provide very useful applications in heterogeneous catalysis. This thesis shows that, at the nanoscale, zirconia exhibits new and unique properties that can notably improve its magnetic properties and its catalytic activity in reactions where the interaction with H_2, metal atoms, or the transfer of oxygen are involved.

It is well known that the supporting oxide has a non-negligible effect on the catalytic properties of metal particles deposited on it (conventional catalysis). Moreover, we have also demonstrated that the creation of a metal-oxide interface affects the properties of the oxide at the perimeter sites. In particular, it plays a key role in the reducibility of zirconia. Thus, we have first investigated the effects of the metal-oxide interaction in the bonding properties of Au and Ag clusters, and secondly, the catalytic activity of a Au/ZrO_2 catalyst in the CO oxidation reaction, in which the oxide reducibility at the metal-oxide interface was found to be determinant.

The deposition of neutral Au and Ag atoms and clusters on a stoichiometric zirconia surface was found to be characterized by a significant contribution of vdW interactions, in which no charge transfer occurred. In particular, we tested several approaches to account for the vdW contribution in the DFT calculations, resulting in different binding energies and even in different relative stability of the several Au_n and Ag_n isomers. This suggests that, when the global minimum of a supported cluster is reached, the most stable isomer might depend also on the approach used to account for vdW interactions. However, the presence of O vacancies and N dopants in the supporting zirconia surface gives rise to modifications in the charge state, binding energies, and structure of the deposited Au and Ag clusters, which will in turn modify their catalytic activity. In general, the extra charge associated to the O vacancy was transferred

to the metals (reduction), and the low-lying empty states introduced by substitutional N dopants captured electrons from them (oxidation). We also tested Nb-doping but no new effects were obtained with respect to the stoichiometric zirconia surface. We can conclude that defects and dopants have a potential effect in modifying the chemical properties of deposited clusters, offering a wide range of possibilities to tune their catalytic activity.

Regarding the chemistry of the support, we observed that the zirconia sites at the perimeter of a deposited Au particle shows a modified reactivity compared to those at the clean terraces (perimeter activation). In particular, the formation energies of O vacancies were decreased by 3.5 eV at the interface, attributed to a structural relaxation around the vacancy and the reduction of Au by the defect electrons. This supposes a key factor in the CO oxidation reaction on a Au/ZrO_2 catalyst through a Mars van-Krevelen mechanism. We demonstrated that this reaction can be performed at the $Au\text{-}ZrO_2$ interface exothermically and with a maximum energy barrier of 0.8 eV only.

Thus, the creation of a metal-oxide interface is also a fundamental aspect to take into account in catalysis, as this modifies not only the chemical properties of the deposited metal particles but also the reactivity of the oxide sites at the perimeter of the particles.

Finally, we also considered the study of a system in which both nanostructuring and a metal-oxide interface are present. We investigated the reducibility of a ZrO_2 2D film supported on a Pt_3Zr and a Pt surface, in terms of the dissociation of the H_2 molecule and the formation of O vacancies.

In this case, by only nanostructuring to a model free-standing 2D film, zirconia still behaves as a nonreducible oxide like bulk zirconia (3D material). However, the deposition of the thin film on the Pt_3Zr and Pt supports changed the picture: the dissociation of a H_2 molecule was highly exothermic and occurred through a homolytic mechanism. The O vacancies were stabilized by 3 – 5 eV with respect to those in bulk zirconia. As in the deposition of clusters on extended zirconia (conventional catalysis), the main role of the metal is the capture of the extra electrons from vacancies or H_2. These results suggest that the combination of nanostructured oxide interfaced with a metal has notably changed the properties of the oxide, but it has only been promoted by the interface with the metal.

Outlook

This thesis has demonstrated important conclusions in the field of oxides for heterogeneous catalysis purely based on DFT calculations. However, new questions can be risen from this work, whose answers may lead to interesting conclusions that complete the picture. For example, 3D and 2D nanostructuring of zirconia (bulk and thin films) do not change its low reducible character, while 0D nanostructuring (nanoparticles) does. This opens the question whether 1D zirconia (nanowires and nanorods) still behaves as a nonreducible oxide, indicating that the periodicity in at least one dimension may be responsible for a nonreducible character. In addition, as the oxide reducibility is affected by nanostructuring, the potential of metal-oxide interfaces at the nanoscale, for example the deposition of metal clusters on oxide nanoparticles, opens up a vast and interesting field for heterogeneous catalysis.

On the other hand, it has to be noted that even highly efficient implementations of the DFT methodology on supercomputers are insufficient to treat big and realistic systems and their interaction with supports, adsorbates, or solvents. Usually, experimental conditions like protective ligands, co-adsorption, pressure and temperature, etc. are not considered in DFT calculations. However, fundamental studies are always necessary to understand catalytic processes at the atomic level or to provide first insights to guide and interpret experiments.

Finally, I hope that the research presented in this thesis is of interest to the scientific community and that it will contribute to the advance of heterogeneous catalysis.

References

[1] A. J. B. Robertson. The Early Story of Catalysis. *Platinum Metals Rev*. 1975, 19, 64 – 69.

[2] V. Smith. Enriching the Earth: Fritz Haber, Carl Bosch, and the Transformation of World Food Production. MIT Press, 2004.

[3] J. W. Erisman, M. A. Sutton, J. Galloway, Z. Klimont, W. Winiwarter. How a Century of Ammonia Synthesis Changed the World. *Nature Geoscience*, 2008, 1, 636 – 639.

[4] R. Masel. Principles of Adsorption and Reaction on Solid Surfaces. Wiley, New York, 1996, 444 – 448.

[5] P. Forzatti, L. Lietti. Catalyst Deactivation. *Catal. Today* 1999, 52, 165.

[6] C. Morterra, L. Orio. Surface Characterization of Zirconium Dioxide. II. The Interaction with Carbon Dioxide at Ambient Temperature. *Mater. Chem. Phys*. 1990, 24, 247.

[7] B. Bachiller-Baeza, I. Rodriguez-Ramos, A. Guerrero-Ruiz. Interaction of Carbon Dioxide with the Surface of Zirconia Polymorphs. *Langmuir* 1998, 14, 3556.

[8] K. Pokrovski, K. T. Jung, A. T. Bell. Investigation of CO and CO_2 Adsorption of Tetragonal and Monoclinic Zirconia. *Langmuir* 2001, 17, 4297.

[9] H.-Y. Tiffany Chen, S. Tosoni, G. Pacchioni. A DFT Study of the Acid-Base Properties of Anatase TiO_2 and Tetragonal ZrO_2 by Adsorption of CO and CO_2 Probe Molecules. *Surf. Sci*. 2016, 652, 163.

[10] M. Ahmadi, H. Mistry, B. Roldan Cuenya. Tailoring the Catalytic Properties of Metal Nanoparticles via Support Interactions. *J. Phys. Chem. Lett*. 2016, 7, 3519 – 3533.

[11] R. J. D. Miller, G. L. McLendon, A. J. Nozik, W. Schmikler, F. Willing. Surface Electron Transfer Processes. VCH: Weinheim, Germany, 1995.

[12] J. Libuda, H. J. Freund. Molecular Beam Experiments on Model Catalysts. *Surf. Sci. Rep.* 2005, 57, 157 – 298.

[13] A. T. Bell. The Impact of Nanoscience on Heterogeneous Catalysis. *Science* 2003, 299, 1688.

[14] F. Zhou, X. Zhao, H. Xu, C. Yuan. CeO_2 Spherical Crystallites: Synthesis, Formation Mechanism, Size Control, and Electrochemical Property Study. *J. Phys. Chem. C* 2007, 111, 1651 – 1657.

[15] S. Y. Bromley, I. P. R. Moreira, K. M. Neyman, F. Illas. Approaching Nanoscale Oxides: Models and Theoretical Methods. *Chem. Soc. Rev.* 2009, 38, 2657 – 2670.

[16] F. Baletto, R. Ferrando. Structural Properties of Nanoclusters: Energetic, Thermodynamic, and Kinetic Effects. *Rev. Mod. Phys.* 2005, 77, 371 – 423.

[17] A. M. Ferrari, G. Pacchioni. Electronic Structure of F and V centers on the MgO Surface. *J. Phys. Chem.* 1995, 99, 17010 – 17018.

[18] G. Pacchioni, H. J. Freund. Electron Transfer at Oxide Surfaces. The MgO Paradigm: From Defects to Ultrathin Films. *J. Chem. Rev.* 2013, 113, 4035 – 4072.

[19] G. Pacchioni. First Principles Calculations on Oxide-Based Heterogeneous Catalysts and Photocatalysts: Problems and Advances. *Catal. Lett.* 2015, 145, 80 – 94.

[20] A. Sawa. Resistive Switching in Transition Metal Oxides. *Mater. Today* 2008, 11, 28 – 36.

[21] G. Korotcenkov. Metal Oxides for Solid-State Gas Sensors: What Determines Our Choice? *Mater. Sci. Eng. B* 2007, 139, 1 – 23.

[22] G. Pacchioni. Ketonization of Carboxylic Acids in Biomass Conversion over TiO_2 and ZrO_2 Surfaces: A DFT Perspective. *ACS Catal.* 2014, 4, 2874 – 2888.

[23] T. N. Pham, T. Sooknoi, S. P. Crossley, D. E. Resasco. Ketonization of Carboxylic Acids: Mechanisms, Catalysis, and Implications for Biomass Conversion. *ACS Catal.* 2013, 3, 2456 – 2473.

[24] M. A. Barteau. Organic Reactions at Well-Defined Oxide Surfaces. *Chem. Rev.* 1996, 96, 1413 – 1430.

[25] T. N. Pham, D. C. Shi, D. E. Resasco. Kinetics and Mechanism of Ketonization of Acetic Acid on Ru/TiO_2 Catalyst. *Top. Catal*. 2014, 57, 706 – 714.

[26] T. N. Pham, D. C. Shi, D. E. Resasco. Reaction Kinetics and Mechanism of Ketonization of Aliphatic Carboxylic Acids with Different Carbon Chain Lengths over Ru/TiO_2 Catalyst. *J. Catal*. 2014, 314, 149 – 158.

[27] M. Haruta, S. Tsubota, T. Kobayashi, H. Kageyama, M. J. Genet, B. Delmon. Low-Temperature Oxidation of CO over Gold Supported on TiO_2, α-Fe_2O_3, and Co_3O_4. *J. Catal*. 1993, 144, 175.

[28] J. D. Grunwaldt, C. Kiener, C. Woegerbauer, A. Beiker. Preparation of Supported Gold Catalysts for Low-Temperature CO Oxidation via “Size-Controlled” Gold Colloids. *J. Catal*. 1999, 181, 223.

[29] Y. Z. Yuan, A. P. Kozlova, K. Asakura, H. Wan, K. Tsai, Y. Iwasawa. Supported Au Catalysts Prepared from Au Phosphine Complexes and As-Precipitated Metal Hydroxides: Characterization and Low-Temperature CO Oxidation. *J. Catal*. 1997, 170, 191.

[30] M. Haruta, N. Yamada, T. Kobayasi, S. Iijima. Gold Catalysts Prepared by Coprecipitation for Low-Temperature Oxidation of Hydrogen and of Carbon Monoxide. *J. Catal*. 1989, 115, 301.

[31] M. A. Centeno, T. R. Reina, S. Ivanova, O. H. Laguna, J. A. Odriozola. Au/CeO_2 Catalysts: Structure and CO Oxidation Activity. *Catalysts* 2016, 6, 158.

[32] M. M. Schubert, S. S. Hackenberg, A. C. van Veen, M. Muhler, V. Plzak, R. J. Behm. CO Oxidation over Supported Gold Catalysts—"Inert" and "Active" Support Materials and their Role for the Oxygen Supply During Reaction. *J. Catal.* 2001, 197, 113.

[33] D. Widmann, R. J. Behm. Activation of Molecular Oxygen and the Nature of the Active Oxygen Species for CO Oxidation on Oxide Supported Au Catalysts. *Acc. Chem. Res.* 2014, 47, 740 – 749.

[34] R. Srinivasan, B. H Davis. Influence of Zirconium Salt Precursors on The Crystal Structures of Zirconia. *Catal. Lett.* 1992, 14, 165.

[35] S. C. Su, A . T. Bell. A Study of ohe Structure of Vanadium Oxide Dispersed on Zirconia. *J. Phys. Chem. B* 1998, 102, 7000.

[36] Z. Dang, B. G. Anderson, Y. Amenomiya, B. A. Morrow. Silica-Supported Zirconia. 1. Characterization by Infrared Spectroscopy, Temperature-Programmed Desorption, and X-Ray Diffraction. *J. Phys. Chem.* 1995, 99, 14437.

[37] J. M. Miller, L. J. Lakshmi. Spectroscopic Characterization of Sol-Gel-Derived Mixed Oxides. *J. Phys. Chem. B* 1995, 102, 6465.

[38] K. Tanabe. Surface and Catalytic Properties of ZrO_2. *Mater. Chem. Phys*. 1985, 13, 347.

[39] R. Srinivasan, D. Taulbee, B. H. Davis. The Effect of Sulfate on The Crystal Structure of Zirconia. *Catal. Lett.* 1991, 9, 1.

[40] K. Tanabe, M. Misono, Y. Ono, H. Hattori. New Solid Acids and Bases: Their Catalytic Properties. *Stud. Surf. Sci. Catal.* 1989, 51, 1.

[41] A. Dwivedi, A. N. Cormack. A Computer Simulation Study of the Defect Structure of Calcia-Stabilized Zirconia. *Philos. Mag. A* 1990, 61, 1 – 22.

[42] V. V. Kharton, F. M. B. Marqués, A. Atkinson. Transport Properties of Solid Oxide Electrolyte Ceramics: A Brief Review. *Solid State Ionics* 2004, 174, 135 – 149.

[43] G. Štefanić, S. Musić. Factors Influencing the Stability of Low Temperature Tetragonal ZrO_2. *Croat. Chem. Acta* 2002, 75, 727 – 767.

[44] R. C. Garvie, R. H. J. Hannink, R. J. Pascoe. Ceramic Steel? *Nature* 1975, 258, 703 – 704.

[45] R. C. Garvie. The Occurrence of Metastable Tetragonal Zirconia as a Crystallite Size Effect. *J. Phys. Chem.* 1965, 69, 1238 – 1243.

[46] S, Shukla, S. Seal. Thermodynamic Tetragonal Phase Stability in Sol-Gel Derived Nanodomains of Pure Zirconia. *J. Phys. Chem. B* 2004, 108, 3395 – 3399.

[47] R. C. Garvie. Stabilization of the Tetragonal Structure in Zirconia Microcrystals. *J. Phys. Chem.* 1978, 82, 218 – 224.

[48] R. H. French, S. J. Glass, F. S. Ohuchi, Y. N. Xu, E. Y. Ching. Experimental and Theoretical Determination of the Electronic Structure and Optical Properties of Three Phases of ZrO_2. *Phys. Rev. B: Condens. Matter Mater. Phys.* 1994, 49, 5133 – 5142.

[49] S. Sayan, R. A. Bartynski, X. Zhao, E. P. Gusev, C. Vanderbilt, M. Croft, M. Banaszak-Holl, E. Garfunkel. Valence and Conduction Band Offsets of a $ZrO_2/SiO_xN_{y/n}$-Si CMOS Gate Stack: A

Combined Photoemission and Inverse Photoemission Study. *Phys. Status Solidi B* 2004, 241, 2246 – 2252.

[50] C. Århammar, C. Moysés-Araújo, R. Ahuja. Energetics of Al Doping and Intrinsic Defects in Monoclinic and Cubic Zirconia: First-Principles Calculations. *Phys. Rev. B* 2009, 80, 115208.

[51] A. Foster, V. Sulimov, F. López-Gejo, A. Shluger, R. Nieminen. Structure and Electrical Levels of Point Defects in Monoclinic Zirconia. *Phys. Rev. B* 2001, 64, 224108.

[52] B. M. Klein, W. E. Pickett, L. L. Boyer, R. Zeller. Theory of F Centers in the Alkaline-Earth Oxides MgO and CaO. *Phys. Rev. B* 1987, 35, 5802.

[53] M. A. Rahman, S. Rout, J. P. Thomas, D. McGillivray, K. T. Leung. Defect-Rich Dopant-Free ZrO_2 Nanostructures with Superior Dilute Ferromagnetic Semiconductor Properties. *J. Am. Chem. Soc.* 2016, 138, 11896 – 11906.

[54] A. Sinhamahapatra. J. P. Jeon, J. Kang, B. Han, J. S. Yu. Oxygen-Deficient Zirconia (ZrO_{2-x}): A New Material for Solar Light Adsorption. *Sci. Rep.* 2016, 6, 27218.

[55] S. Ning, P. Zhan, Q. Xie, Z. Li, Z. Zhang. Room-Temperature Ferromagnetism in Undoped ZrO_2 Thin Films. *J. Phys. D: Appl. Phys.* 2013, 46, 445004 – 445008.

[56] S. Ning, Z. Zhang. Phase-Dependent and Defect-Driven d^0 Ferromagnetism in Undoped ZrO_2 Thin Films. *RSC Adv.* 2015, 5, 3636 – 3641.

[57] M. Boujnah, H. Labrim, K. Allam, A. Belhaj, A. Benyoussef, A. El Kenz, B. Belhorma, A. El Bouari. Magnetic and Electronic Properties of Point Defects in ZrO_2. *J. Supercond. Nov. Magn.* 2013, 26, 2429 – 2434.

[58] G. D. Wilk, R. M. Wallace, J. M. Anthony. High-κ Gate Dielectrics: Current Status and Materials Properties Considerations. *J. Appl. Phys.* 2001, 89, 5243 – 5375.

[59] R. P. Reade, P. Berdahl, R. E. Russo, S. M. Garrison. Laser Deposition of Biaxially Textured Yttria-Stabilized Zirconia Buffer Layers on Polycrystalline Metallic Alloys for High Critical Current Y-Ba-Cu-O Thin Films. *Appl. Phys. Lett*. 1992, 61, 2231.

[60] E. V. Pechen, R. Schoenberger, B. Brunner, S. Ritzinger, K. F. Renk, M. V. Sidorov, S. R. Oktyabrsky. Epitaxial Growth of $YBa_2Cu_3O_{7-\delta}$ Films on Oxidized Silicon with Yttria- and Zirconia-Based Buffer Layers. *J. Appl. Phys.* 1993, 74, 3614.

[61] D. R. Clarke, C. G. Levi. Materials Design for the Next Generation Thermal Barrier Coatings. *Annu. Rev. Mater. Res.* 2003, 33, 383.

[62] J. Nawrocki, C. Dunlap, J. Li, J. Zhao, C. V. McNeff, A. McCormick, P. W. Carr. Chromatography Using Ultra-Stable Metal Oxide-Based Stationary Phases for HPLC. *J. Chromatogr. A* 2004, 1028, 31 – 62.

[63] N. Rajabbeiji, B. Elyassi, A. Khodadadi, S. S. Mohajerzadeh, M. Sahimi. A Novel Miniaturized Oxygen Sensor with Solid-State Ceria-Zirconia Reference. *Sensors and Actuators B* 2004, 100, 139 – 142.

[64] W. J. Fleming. Physical Principles Governing Non-ideal Behavior of the Zirconia Oxygen Sensor. *J. Electrochem. Soc.* 1977, 124, 21 – 28.

[65] V. Idakiev, T. Tabakova, A. Naydenov, Z. Y. Yuan, B. L. Su. Gold Catalysis Supported on Mesoporous Zirconia for Low-Temperature Water Gas Shift Reaction. *Appl. Catal. B* 2006, 63, 178 – 186.

[66] N. Iwasa, S. Kudo, H. Takahashi, S. Masuda, N. Takezawa. Highly Selective Supported Pd Catalysts for Steam Reforming of Methanol. *Catal. Lett.* 1993, 19, 211 – 216.

[67] N. Laosiripojana, S. Assabumrungrat. Catalytic Steam Reforming of Methane, Methanol, and Ethanol Over Ni/YSZ: The Possible Use of These Fuels in Internal Reforming SOFC. *J. Power Sources* 2007, 163, 943 – 951.

[68] J. Wang, Z. You, Q. Zhang, W. Deng, Y. Wang. Synthesis of Lower Olefins by Hydrogenation of Carbon Dioxide over Supported Iron Catalysts. *Catal. Today* 2013, 215, 186 – 193.

[69] M. D. Rhodes, A. T. Bell. The Effects of Zirconia Morphology on Methanol Synthesis from CO and H_2 over Cu/ZrO_2 Catalysts: Part I. Steady-State Studies. *J. Catal*. 2005, 233, 198 – 209.

[70] Y. Nakano. T. Yamaguchi, K. Tanabe. Hydrogenation of Conjugated Dienes over ZrO_2 by H_2 and Cyclohexadiene. *J. Catal.* 1983, 80, 307 – 314.

[71] A. Knell, P. Barnikel, A. Baiker, A. Wokaun. CO Oxidation over Au/ZrO_2 Catalyst: Activity, Deactivation Behavior, and Reaction Mechanism. *J. Catal.* 1992, 137, 306 – 321.

[72] X. Zhang, H. Wang, B. Q. Xu. Remarkable Nanosize Effect in Au/ZrO_2 Catalyst for CO Oxidation. *J. Phys. Chem. B* 2005, 109, 9678 – 9683.

[73] M. Comotti, W. C. Li, B. Spliethoff, F. Schuth. Support Effect in High Activity Gold Catalysts for CO Oxidation. *J. Am. Chem. Soc*. 2006, 128, 917 – 924.

[74] K. Sayama, H. Arakawa. Photocatalytic Decomposition of Water and Photocatalytic Reduction of Carbon Dioxide over Zirconia Catalyst. *J. Phys. Chem.* 1993, 97, 531 – 533.

[75] Y. Kohno, T. Tanaka, T. Funabiki, S. Yoshida. Photoreduction of Carbon Dioxide with Hydrogen over ZrO_2. *Chem. Commun.* 1997, 841 – 842.

[76] C. Sun, U. Stimming. Recent Anode Advances in Solid Oxide Fuel Cells. *J. Power Sources* 2007, 171, 247 – 260.

[77] F. He, D. Song, R. R. Peng, G. Y. Meng, S. F. Yang. Electrode Performance and Analysis of Reversible Solid Oxide Fuel Cells with Proton Conducting Electrolyte of $BaCe_{0.5}Zr_{0.3}Y_{0.2}O_{3-\delta}$. *J. Power Sources* 2010, 195, 3359 – 3364.

[78] M. Shishkin, T. Ziegler. The Oxidation of H_2 and CH_4 on an Oxygen-Enriched Yttria-Stabilized Zirconia Surface: A Theoretical Study Based on Density Functional Theory. *J. Phys. Chem. C* 2008, 112, 19662 – 19669.

[79] T. Horita, K. Yamaji, N. Sakai, Y. Xiong, T. Kato, H. Yokokawa, T. Kawada. Imaging of Oxygen Transport at SOFC Cathode/Electrolyte Interfaces by a Novel Technique. *J. Power Sources* 2002, 106, 224 – 230.

[80] A. P. Alivisatos. Semiconductor clusters, nanocrystals, and quantum dots. *Science* 1996, 271, 933 – 937.

[81] T. Hyeon. Chemical Synthesis of Magnetic Nanoparticles. *Chem. Commun*. 2003, 927 – 934.

[82] S. A. Majetich, Y. Jin. Magnetization Directions of Individual Nanoparticles. *Science* 1999, 284, 470 – 473.

[83] C. Di Valentin, R. Ferullo, R. Binda, G. Pacchioni. Oxygen Vacancies and Peroxo Groups on Regular and Low-Coordinated Sites of MgO, CaO, SrO and BaO Surfaces. *Surf. Sci*. 2006, 600, 1147 – 1154.

[84] Pacchioni, G.; Percarmona, P. Structure and Stability of Oxygen Vacancies on Sub-Surface, Terraces, and Low-Coordinated Surface Sites on MgO: An Ab-Initio Study. *Surf. Sci*. 1998, 412 − 413, 657 − 671.

[85] Pacchioni, G. Physisorbed and Chemisorbed CO_2 at the Surface and Step Sites of the MgO (100) Surface. *Surf. Sci.* 1993, 281, 207 − 219.

[86] L. Giordano, C. Di Valentin, J. Goniakowski, G. Pacchioni. Nucleation of Pd Dimers at Defect Sites on the MgO (100) Surface. *Phys. Rev. Lett.* 2004, 92, 096105 − 096109.

[87] X. Gong, A. Selloni, O. Dulub, P. Jacobson, U. Diebold. Small Au and Pt Clusters at the Anatase TiO_2 (101) Surface: Behavior at Terraces, Steps, and Surface Oxygen Vacancies. *J. Am. Chem. Soc.* 2008, 130, 370−381.

[88] M. Bruchez, M. Moronne, P. Gin, S. Weiss, A. P. Alivisatos. Semiconductor Nanocrystals as Fluorescent Biological Labels. *Science* 1998, 281, 2013 – 2016.

[89] C. T. Black, C. B. Murray, R. L. Sandstrom, S. Sun. Spin-dependent Tunneling in Self-Assembled Cobalt-Nanocrystal Superlattices. *Science* 2000, 290, 1131−1134.

[90] S. Sun, C. B. Murray, D. Weller, L. Folks, A. Moser. Monodisperse FePt Nanoparticles and Ferromagnetic FePt Nanocrystal Superlattices. *Science* 2000, 287, 1989−1992

[91] G. A. Somorjai, A. M. Contreras, M. Montano, R. M. Rioux. Clusters, Surfaces and Catalysis. *Proc. Natl. Acad. Sci. U. S. A.* 2006, 103, 10577 – 10583.

[92] A. Trovarelli. Catalytic Properties of Ceria and CeO_2-Containing Materials. *Catal. Rev.: Sci. Eng*. 1996, 38, 439 – 520.

[93] C. Loschen, A. Migani, S. T. Bromley, F. Illas, K. M. Neyman. Density Functional Studies of Model Cerium Oxide Nanoparticles. *Phys. Chem. Chem. Phys*. 2008, 10, 5730 – 5738.

[94] A. Migani, G. N. Vayssilov, S. T. Bromley, F. Illas, K. M. Neyman. Greatly Facilitated Oxygen Vacancy Formation in Ceria Nanocrystallites. *Chem. Commun*. 2010, 46, 5936 – 5938.

[95] J. Colon, N. Hsieha, A. Fergusona, P. Kupelian, S. Seal, D. W. Jenkins, C. H. Baker. Cerium Oxide Nanoparticles Protect Gastrointestinal Epithelium from Radiation-Induced Damage by Reduction of Reactive Oxygen Species and Upregulation of Superoxide Dismutase 2. *Nanomedicine: NBM* 2010, 6, 698 – 705.

[96] H. Zhang, Z. Ji, T. Xia, H. Meng, C. Low-Kam, R. Liu, S. Pokhrel, S. Lin, X. Wang, Y.-P. Liao, et al. Use of Metal Oxide Nanoparticle Band Gap to Develop a Predictive Paradigm for Oxidative Stress and Acute Pulmonary Inflammation. *ACS Nano* 2012, 6, 4349 – 4368.

[97] A. Asati, S. Santra, C. Kaittanis, S. Nath, J. M. Perez. Oxidase-Like Activity of Polymer-Coated Cerium Oxide Nanoparticles. *Angew. Chem*. 2009, 121, 2344 – 2348.

[98] Y. K. Kho, A. Iwase, W. Y. Teoh, L. Mädler, A. Kudo, R. Amal. Photocatalytic H_2 Evolution over TiO_2 Nanoparticles. The Synergistic Effect of Anatase and Rutile. *J. Phys. Chem. C* 2010, 114, 2821 – 2829.

[99] J. Zhang, Q. Xu, Z. Feng, M. Li, C. Li. Importance of the Relationship between Surface Phases and Photocatalytic Activity of TiO_2. *Angew. Chem. Int. Ed*. 2008, 47, 1766 – 1769.

[100] E. Quagliarinia, F. Bondiolib, G. B. Goffredoa, C. Cordonia, P. Munafòa. Self-cleaning and de-polluting stone surfaces: TiO_2 nanoparticles for limestone. *Contr. Build. Mater*. 2012, 37, 51 – 57.

[101] T. Z. Jin, D. Z. Wan, S. Y. Han, Y. X. Sui, X. N. Zhao. Investigation of Nanocrystalline SnO_2 by Electron Spin Resonance. *Chin. Phys. Lett. (Engl)* 1992, 9, 549.

[102] P. Clau, A. Brücker, C. Mohr, H. Hofmeister. Supported Gold Nanoparticles from Quantum Dot to Mesoscopic Size Scale: Effect of Electronic and Structural Properties on Catalytic Hydrogenation of Conjugated Functional Groups. *J. Am. Chem. Soc*. 2000, 122, 11430.

[103] H. Liu, L. Feng, X. Zhang, Q. Xue. ESR Characterization of ZrO_2 Nanopowder. *J. Phys. Chem.* 1995, 99, 332.

[104] J. J. Pietron, R. M. Stroud, D. R. Rolison. Using Three Dimensions in Catalytic Mesoporous Nanoarchitectures. *Nano Lett.* 2002, 2, 545.

[105] D. R. Rolison. Catalytic Nanoarchitectures--The Importance of Nothing and the Unimportance of Periodicity. *Science* 2003, 299, 1698.

[106] H. J. Freund, H. Kuhlenbeck, V. Staemmler. Oxide Surfaces. *Rep. Prog. Phys*. 1996, 59, 283.

[107] I. Sebastian, T. Bertrams, K. Meinel, H. Neddermeyer. Scanning Tunnelling Microscopy on the Growth and Structure of Nio (100) and CoO (100) Thin Films. *Faraday Discuss*. 1999, 114, 20.

[108] C. O. A. Olsson, D. Landolt. Passive Films on Stainless Steels—Chemistry, Structure and Growth. *Electrochim. Acta* 2003, 48, 1093.

[109] S. S. P. Parkin, C. Kaiser, A. Panchula, P. M. Rice, B. Hughes, M. Samant, S. H. Yang. Giant Tunnelling Magnetoresistance at Room Temperature with MgO (100) Tunnel Barriers. *Nat. Mater.* 2004, 3, 862.

[110] G. Pacchioni. Two-Dimensional Oxides: Multifunctional Materials for Advanced Technologies. *Chem. – Eur. J.* 2012, 18, 10144.

[111] J. Schoiswohl, S. Surnev, F. P. Netzer. Reactions on Inverse Model Catalyst Surfaces: Atomic Views by STM. *Top. Catal.* 2005, 36, 91 – 105.

[112] J. A. Rodriguez, J. Hrbek. Inverse Oxide/Metal Catalysts: A Versatile Approach for Activity Tests and Mechanistic Studies. *Surf. Sci*. 2010, 604, 241 – 244.

[113] S. M. Kozlov, I. Demiroglu, K. M. Neyman, S. T. Bromley. Reduced Ceria Nanofilms from Structure Prediction. *Nanoscale* 2005, 7, 4361.

[114] Y. Zhang, L. Giordano, G. Pacchioni, A. Vittadini, F. Sedona, P. Finetti, G. Granozzi. The Structure of A Stoichiometric TiO_2 Nanophase on Pt (111). *Surf. Sci*. 2007, 601, 3488.

[115] H. J. Freund. Adsorption of Gases on Complex Solid Surfaces. *Angew. Chem., Int. Ed.* 1997, 109, 452 – 475.

[116] H. J. Freund, G. Pacchioni. Oxide Ultra-Thin Films on Metals: New Materials for the Design of Supported Metal Catalysts. *Chem. Soc. Rev*. 2008, 37, 2224.

[117] J. Goniakowsky, C. Noguera. Electronic States and Schottky Barrier Height at Metal/Mgo (100) Interfaces. *Interface Sci.* 2004, 12, 93.

[118] V. Heine. Theory of Surface States. *Phys. Rev.* 1965, 138, A1689.

[119] L. Giordano, G. Pacchioni. Charge Transfers at Metal/Oxide Interfaces: A DFT Study of Formation of $K^{\delta+}$ and $Au^{\delta-}$ Species on MgO/Ag (100) Ultra-Thin Films From Deposition of Neutral Atoms. *Phys. Chem. Chem. Phys.* 2006, 8, 3335.

[120] R. W. Gurney. Theory of Electrical Double Layers In Adsorbed Films. *Phys. Rev.* 1935, 47, 479.

[121] K. H. Kingdom, J. Langmuir. Thermionic Phenomena Due to Alkali Vapors. *Phys. Rev.* 1923, 21, 380.

[122] A. Zangwill. Physics at surfaces, Cambridge University Press, Cambridge, 1988.

[123] L. Giordano, F. Cinquini, G. Pacchioni. Tuning the Surface Metal Work Function by Deposition of Ultrathin Oxide Films: Density Functional Calculations. *Phys. Rev. B* 2006, 73, 045414.

[124] L. Giordano, J. Goniakowsky, G. Pacchioni. Properties of MgO (100) Ultrathin Layers on Pd (100): Influence of The Metal Support. *Phys. Rev. B* 2003, 67, 045410.

[125] S. Prada, U. Martinez, G. Pacchioni. Work Function Changes Induced by Deposition of Ultrathin Dielectric Films on Metals: A Theoretical Analysis. *Phys. Rev. B 2008*, 78, 235423.

[126] L. Giordano, M. Baistrocchi, G. Pacchioni. Bonding of Pd, Ag, and Au Atoms on MgO (100) Surfaces and MgO/Mo (100) Ultra-Thin Films: A Comparative DFT Study. *Phys. Rev. B* 2005, 72, 115403.

[127] M. Sterrer, T. Risse, U. Martinez Pozzoni, L. Giordano, M. Heyde, H.-P. Rust, G. Pacchioni, H.-J. Freund. Control of the Charge State of Metal Atoms on Thin MgO Films. *Phys. Rev. Lett.* 2007, 98, 096107.

[128] D. Ricci, A. Bongiorno, G. Pacchioni, U. Landman. Bonding Trends and Dimensionality Crossover of Gold Nanoclusters on Metal-Supported MgO Thin Films. *Phys. Rev. Lett*. 2006, 97, 036106.

[129] A. Hellman, S. Klacar, H. Grönbeck. Low Temperature CO Oxidation over Supported Ultrathin MgO Films. *J. Am. Chem. Soc*. 2009, 131, 16636.

[130] A. Gonchar, T. Risse, H.-J. Freund, L. Giordano, C. Di Valentin, G. Pacchioni. Activation of Oxygen on MgO: O^{2-} Radical Ion Formation on Thin, Metal-Supported MgO (001) Films. *Angew. Chem., Int. Ed.* 2011, 50, 2635.

[131] P. Frondelius, A. Hellman, K. Honkala, H. Hakkinen, H. Grönbeck. Charging of Atoms, Clusters, and Molecules on Metal-Supported Oxides: A General and Long-Ranged Phenomenon. *Phys. Rev. B* 2008, 78, 085426.

[132] E. Emmez, B. Yang, S. Shaikhutdinov, H. J. Freund. Permeation of a Single-Layer SiO_2 Membrane and Chemistry in Confined Space. *J. Phys. Chem. C* 2014, 118, 29034 – 29042.

[133] R. Mu, Q. Fu, L. Jin, L. Yu, G. Fang, D. Tan, X. Bao. Visualizing Chemical Reactions Confined Under Graphene. *Angew. Chem., Int. Ed.* 2012, 51, 4856 – 4859.

[134] M. Valden, X. Lai, D. W. Goodman. Onset of Catalytic Activity of Gold Clusters on Titania with the Appearance of Nonmetallic Properties. *Science* 1998, 281, 1647.

[135] H. Hakkinen, W. Abbet, A. Sánchez, U. Heiz, U. Landman. Structural, Electronic, and Impurity-Doping Effects in Nanoscale Chemistry: Supported Gold Nanoclusters. *Angew. Chem., Int. Ed*. 2003, 42, 1297.

[136] H. G. Boyen. G. Kastle, F. Weigl, B. Koslowski, C. Dietrich, P. Ziemann, J. P. Spatz, S. Riethmuller, C. Hartmann, M. Moller, et al. Oxidation-Resistant Gold-55 Clusters. *Science* 2002, 297, 1533.

[137] C. Leung, C. Xirouchaki, N. Berovic, R. E. Palmer. Immobilization of Protein Molecules by Size-Selected Metal Clusters on Surfaces. *Adv. Mater*. 2004, 16, 223.

[138] K. Settler. *Festkor-Adv Solid St*. 1983, 23, 11.

[139] O. Lamiel-Garcia, K. C. Ko, J. Y. Lee, S. T. Bromley, F. Illas. When Anatase Nanoparticles Become Bulklike: Properties of Realistic TiO_2 Nanoparticles in the 1-6 nm Size Range from All Electron Relativistic Density Functional Theory Based Calculations. *J. Chem. Theory Comput*. 2017, 13, 1785 – 1793.

[140] E. C. Tyo, S. Vajda. Catalysis by Clusters with Precise Number of Atoms. *Nature Nanotech*. 2015, 10, 577 – 588.

[141] V. V. Kresin, W. Knight. Ordered States in Disordered Particles: Electronic Shells and Structural Effects in Metal Clusters. *Z. Phys. Chem*. 1998, 203, 57.

[142] V. Paillard, P. Melinon, V. Dupuis, J. P. Perez, A. Perez, B. Champagnon. Diamondlike Carbon Films Obtained by Low Energy Cluster Beam Deposition: Evidence of a Memory Effect of the Properties of Free Carbon Clusters. *Phys. Rev. Lett.* 1993, 71, 4170.

[143] M. Salmeron, R. Schlogl. Ambient Pressure Photoelectron Spectroscopy: A New Tool for Surface Science and Nanotechnology. *Surf. Sci. Rep*. 2008, 63, 169 – 199.

[144] F. Zaera. Nanostructured Materials for Applications in Heterogeneous Catalysis. *Chem. Soc. Rev.* 2013, 42, 2746 – 2762.

[145] B. R. Cuenya, F. Behafarid. Nanocatalysts: Size- and Shape-Dependent Chemisorption and Catalytic Reactivity. *Surf. Sci. Rep*. 2015, 70, 135 – 187.

[146] B. Gilbert, F. Huang, H. Zhang, G. A. Wayhunas, J. F. Banfield. Nanoparticles: Strained and Stiff. *Science* 2004, 305, 651 – 654.

[147] U. Heiz, U. Landman, eds. Nanocatalysis. Springer-Verlag, 2007, Berlin Heidelberg.

[148] A. M. Boies, J. T. Roberts, S. L. Girshick, B. Zhang, T. Nakamura, A. Mochizuki. SiO_2 Coating of Silver Nanoparticles by Photoinduced Chemical Vapor Deposition. *Nanotech*. 2009, 20, 295604.

[149] R. Narayanan, M. A. El-Sayed. Effect of Nanocatalysis in Colloidal Solution on the Tetrahedral and Cubic Nanoparticle Shape: Electron Transfer Reaction Catalyzed by Platinum Nanoparticles. *J. Phys. Chem. B* 2004, 108, 5726 – 5733.

[150] Z. C. Zhang, B. Xu, X. Wang. Engineering Nanointerfaces for Nanocatalysis. *Chem. Soc. Rev*. 2014, 43, 7870 – 7886.

[151] M. Haruta. Size- and Support-Dependency in the Catalysis of Gold. *Catal. Today* 1997, 36, 153 – 166.

[152] V. R. Cooper, A. M. Kolpak, Y. Yourdshahyan, A. M. Rappe. Supported Metal Electronic Structure: Implications for Molecular Adsorption. *Phys. Rev. B: Condens. Matter Mater. Phys*. 2005, 72, 081409.

[153] B. Olthof, A. Khodakov, A. T. Bell, E. Iglesia. Effects of Support Composition and Pretreatment Conditions on the Structure of Vanadia Dispersed on SiO_2, Al_2O_3, TiO_2, ZrO_2, and HfO_2. *J. Phys. Chem. B* 2000, 104, 1516 – 1528.

[154] Y. Z. Li, Y. N. Fan, H. P. Yang, B. L. Xu, L. Y. Feng, M. F. Yang, Y. Chen. Strong Metal-Support Interaction and Catalytic Properties of Anatase and Rutile Supported Palladium Catalyst Pd/TiO_2. *Chem. Phys. Lett*. 2003, 372, 160 – 165.

[155] J.-D. Grunwaldt, M. Maciejewski, O. S. Becker, P. Fabrizioli, A. I. Baiker. Comparative Study of Au/TiO_2 and Au/ZrO_2 Catalysts for Low-Temperature CO Oxidation. *J. Catal. 1999*, 186, 458 – 469.

[156] H. Brune, K. Bromann, H. Roder, K. Kern, J. Jacobsen, P. Stoltze, K. Jacobsen, J. K. Norskov. Effect of Strain on Surface-Diffusion and Nucleation. *Phys. Rev. B: Condens. Matter Mater. Phys.* 1995, 52, 14380 – 14383.

[157] I. V. Yudanov, A. Genest, S. Schauermann, H.-J. Freund, N. Rösch. Size Dependence of the Adsorption Energy of CO on Metal Nanoparticles: A DFT Search for the Minimum Value. *Nano Lett.* 2012, 12, 2134 – 2139.

[158] J. Greeley, J. K. Norskov, M. Mavrikakis. Electronic Structure and Catalysis on Metal Surfaces. *Annu. Rev. Phys. Chem*. 2002, 53, 319 – 348.

[159] G. N. Vayssilov, Y. Lykhach, A. Migani, T. Staudt, G. P. Petrova, N. Tsud, T. Skála, A. Bruix, F. Illas, K. C. Prince, et al. Support Nanostructure Boosts Oxygen Transfer to Catalytically Active Platinum Nanoparticles. *Nat. Mater*. 2011, 10, 310 – 315.

[160] R. Prins. Hydrogen Spillover. Facts and Fiction. *Chem. Rev.* 2012, 112, 2714 – 2738.

[161] A. J. Ramirez-Cuesta, R. A. Bennett, P. Stone, P. C. H. Mitchell, M. Bowker. STM Investigation and Monte-Carlo Modelling of Spillover in a Supported Metal Catalyst. *J. Mol. Catal. A: Chem.* 2001, 167, 171 – 179.

[162] G. Pacchioni. Electronic Interactions and Charge Transfers of Metal Atoms and Clusters on Oxide Surfaces. *Phys. Chem. Chem. Phys*. 2013, 15, 1737 – 1757.

[163] A. Sánchez, S. Abbet, U. Heiz, W. D. Schneider, H. Häkkinen, R. N. Barnett, U. Landman. When Gold is not Noble: Nanoscale Gold Catalysts. *J. Phys. Chem. A* 1999, 103, 9573 – 9578.

[164] C. Harding, V. Habibpour, S. Kunz, A. N.-S. Farnbacher, U. Heiz, B. Yoon, U. Landman. Control and Manipulation of Gold Nanocatalysis: Effects of Metal Oxide Support Thickness and Composition. *J. Am. Chem. Soc.* 2009, 131, 538 – 548.

[165] X. Shao, S. Prada, L. Giordano, G. Pacchioni, N. Nilius, H.-J. Freund. Tailoring the Shape of Metal Ad-Particles by Doping the Oxide Support. *Angew. Chem., Int. Ed*. 2011, 50, 11525 – 11527.

[166] B. Qiao, A. Wang, X. Yang, L. F. Allard, Z. Jiang, Y. Cui, J. Liu, J. Li, T. Zhang. Single-Atom Catalysis of CO Oxidation Using Pt_1/FeO_x. *Nat. Chem*. 2011, 3, 634 – 641.

[167] L. K. Ono, F. Behafarid, B. R. Cuenya. Nano-Gold Diggers: Au Assisted SiO_2 Decomposition and Desorption in Supported Nano-Catalysts. *ACS Nano* 2013, 7, 10327 – 10334.

[168] Y. Lykhach, T. Staudt, M. P. A. Lorenz, R. Streber, A. Bayer, H. P. Steinrück, J. Libuda. Microscopic Insights into Methane Activation and Related Processes on Pt/Ceria Model Catalysts. *ChemPhysChem* 2010, 11, 1496 – 1504.

[169] E. Schrödinger. An Undulatory Theory of the Mechanics of Atoms and Molecules. *Phys. Rev*. 1926, 28, 1049 – 1070.

[170] M. Born, J. Oppenheimer. Zur Quantentheorie der Molekeln. *Ann. Phys*. 1927, 84, 457 – 484.

[171] C. Møller, M. S. Plesset. Note on an Approximation Treatment for Many-Electron Systems. *Phys. Rev*. 1934, 46, 618 – 622.

[172] S. C. David; Schaefer III, F. Henry. Löwdin, Per-Olov, ed. The Configuration Interaction Method: Advances in Highly Correlated Approaches. Advances in Quantum Chemistry, 34. San Diego: Academic Press 1999, 143 – 269.

[173] P. Hohenberg, W. Kohn. Inhomogeneous Electron Gas. *Phys. Rev.* 1964, 136, B864 – 871.

[174] W. Kohn, L. J. Sham. Self-consistent Equations Including Exchange and Correlation Effects. *Phys. Rev.* 1965, 140, A1133 – 1138.

[175] S. H. Vosko, L. Wilk, M. Nusair. Accurate Spin-Dependent Electron Liquid Correlation Energies for Local Spin Density Calculations: A Critical Analysis. *Can. J. Phys.* 1980, 58, 1200 – 1211.

[176] J. P. Perdew, K. Burke, M. Ernzerhof. Generalized Gradient Approximation Made Simple. *Phys. Rev. Lett.* 1996, 77, 3865.

[177] J. P. Perdew, Y. Wang. Accurate and Simple Analytic Representation of the Electron-gas Correlation Energy. *Phys. Rev. B* 1992, 45, 13244 – 13249.

[178] I. de P. R. Moreira, F. Illas, R. L. Martin. Effect of Fock Exchange on the Electronic Structure and Magnetic Coupling in NiO. *Phys. Rev. B* 2002, 65, 155102.

[179] M. Gerosa, C. E. Bottani, L. Caramella, G. Onida, C. Di Valentin, G. Pacchioni. Defect Calculations in Semiconductors Through a Dielectric-Dependent Hybrid DFT Functional: The Case of Oxygen Vacancies in Metal Oxides. *J. Chem. Phys.* 2015, 143, 134702 – 134710.

[180] M. Gerosa, C. E. Bottani, L. Caramella, G. Onida, C. Di Valentin, G. Pacchioni. Electronic Structure and Phase Stability of Oxide Semiconductors: Performance of Dielectric-Dependent Hybrid Functional DFT, Benchmarked against GW Band Structure Calculations and Experiments. *Phys. Rev. B: Condens. Matter Mater. Phys*. 2015, 91, 155201 – 155216.

[181] A. D. Becke. A New Mixing of Hartree-Fock and Local Density Functionals Theories. *J. Chem. Phys.* 1993, 98, 1372 – 1377.

[182] A. D. Becke. Density Functinoal Thermochemistry III. The Role of Exact Exchange. *J. Chem. Phys.* 1993, 98, 5648 – 5652.

[183] J. Hubbard. Electron Correlations in Narrow Energy Bands IV the Atomic Representation. *Proc. Roy. Soc. London* 1965, series A, 285 – 542.

[184] V. I. Anisimov, F. Aryasetiawan, A. I. Lichtenstein. First Principles Calculations of the Electronic Structure and Spectra of Strongly Correlated Systems: the LDA+U Method. *J. Phys.: Condensed Matter* 1997, 9, 767 – 808.

[185] S. Grimme. Semiempirical GGA-type Density Functional Constructed with a Long-Range Dispersion Correction. *J. Comput. Chem.* 2006, 27, 1787 – 1799.

[186] N. W. Ashcroft, N. D. Mermin. Solid State Physics. Holt Saunders, Philadelphia 1976.

[187] H. Jónsson, G. Mills, K. W. Jacobsen. Nudged Elastic Band Method for Finding Minimum Energy Paths of Transitions. J. Berne, G. Ciccoti, D. F. Coker, Eds. Classical and Quantum Dynamics in Condensed Phase Simulations. World Scientific, Singapore, 1998, 385.

[188] G. Mills, H. Jónsson. *Phys. Rev. Lett*. 1994, 72, 1124.

[189] G. Mills, H. Jónsson, G. K. Schenter. *Surf. Sci.* 1995, 324, 305.

[190] G. Kresse, J. Furthmüller. Efficient of Ab-Initio Total Energy Calculations for Metals and Semiconductors Using a Plane-Wave Basis Set. *J. Comput. Mater. Sci*. 1996, 6, 15 – 50.

[191] G. Kresse, J. Furthmüller. Efficient Iterative Scheme for Ab-Initio Total Energy Calculations Using a Plane-Wave Basis Set. *Phys. Rev. B* 1996, 54, 11169.

[192] X. Ren, P. Rinke, V. Blum, J. Wieferink, A. Tkatchenko, A. Sanfilippo, K. Reuter, M. Scheffler. Resolution-of-Identity Approach to Hartree−Fock, Hybrid Density Functionals, RPA, MP2 and GW with Numeric Atom-Centered Orbital Basis Functions. *New J. Phys.* 2012, 14, 053020 – 053075.

[193] P. E. Blöchl. Projector Augmented-Wave Method. *Phys. Rev. B* 1994, 50, 17953 – 17979.

[194] G. Kresse, J. Joubert. From Ultrasoft Pseudopotentials to the Projector Augmented-Wave Method. *Phys. Rev. B* 1999, 59, 1758 – 1775.

[195] V. I. Anisimov, J. Zaanen, O. K. Andersen. Band Theory and Mott Insulators: Hubbard U Instead of Stoner I. *Phys. Rev. B* 1991, 44, 943 – 954.

[196] S. L. Dudarev, G. A. Botton, S. Y. Savrasov, C. J. Humphreys, A. P. Sutton. Electron-Energy-Loss Spectra and the Structural Stability of Nickel Oxide: An LSDA+U Study. *Phys. Rev. B* 1998, 57, 1505 – 1509.

[197] O. A. Syzgantseva, M. Calatayud, C. Minot. Revealing the Surface Reactivity of Zirconia by Periodic DFT Calculations. *J. Phys. Chem. C* 2012, 116, 6636 – 6644.

[198] G. Teufer. The Crystal Structure of Tetragonal ZrO_2. *Acta Crystallogr*. 1962, 15, 1187.

[199] S. Tosoni, J. Sauer. Accurate Quantum Chemical Energies for the Interaction of Hydrocarbons with Oxide Surfaces: CH_4/MgO(001). *Phys. Chem. Chem. Phys*. 2010, 12, 14330 – 14340.

[200] R. F. W. Bader. A Quantum Theory of Molecular Structure and Its Applications. *Chem. Rev*. 1991, 91, 893 – 928.

[201] A. Christensen, E. A. Carter. First-Principles Study of the Surfaces of Zirconia. *Phys. Rev. B: Condens. Matter Mater. Phys.* 1998, 58, 8050 – 8064.

[202] M. V. Ganduglia-Pirovano, A. Hofmann, J. Sauer. Oxygen Vacancies in Transition Metal and Rare Earth Oxides: Current State of Understanding and Remaining Challenges. *Surf. Sci. Rep*. 2007, 62, 219 – 270.

[203] A. Eichler, G. Kresse. First-Principles Calculations for the Surface Termination of Pure and Yttria-Doped Zirconia Surfaces. *Phys. Rev. B: Condens. Matter Mater. Phys*. 2004, 69, 045402 – 045419.

[204] R. Grena, O. Masson, L. Portal, F. Rémondière, A. Berghout, J. Jouin, P. Thomas. Stabilization Effect of Surface Impurities on the Structure of Ultrasmall ZrO_2 Nanoparticles: An Ab-Initio Study. *J. Phys. Chem. C* 2015, 119, 15618 − 15626.

[205] F. Zhang, Q. Jin, S. W. Chan. Ceria Nanoparticles: Size, Size Distribution, and Shape. *J. Appl. Phys.* 2004, 95, 4319 – 4326.

[206] A. Migani, K. M. Neyman, S. T. Bromley. Octahedrality Versus Tetrahedrality in Stoichiometric Ceria Nanoparticles. *Chem. Commun.* 2012, 48, 4199 – 4201.

[207] Y. Gao, S. A. Elder. TEM Study of TiO_2 Nanocrystals with Different Particle Size and Shape. *Mater. Lett.* 2000, 44, 228 – 232.

[208] A. S. Barnard, L. A. Curtiss. Prediction of TiO_2 Nanoparticle Phase and Shape Transitions Controlled by Surface Chemistry. *Nano Lett*. 2005, 5 (7), 1261 – 1266.

[209] L. Chen, T. Mashimo, E. Omurzak, H. Okudera, C. Iwamoto, A. Yoshiasa. Pure Tetragonal ZrO_2 Nanoparticles Synthesized by Pulsed Plasma in Liquid. *J. Phys. Chem. C* 2011, 115, 9370 – 9375.

[210] W. M. Haynes. CRC Handbook of Chemistry and Physics, 96th ed.; CRC Press/Taylor and Francis: Boca Raton, FL, 2015

[211] X. Huang, M. J. Beck. Surface Structure of Catalytically-Active Ceria Nanoparticles. *Comput. Mater. Sci.* 2014, 91, 122 – 133.

[212] E. Bersch, S. Rangan, R. A. Bartynski, E. Garfunkel, E. Vescovo. Band Offsets of Ultrathin High-κ Oxide Films with Si. *Phys. Rev. B: Condens. Matter Mater. Phys*. 2008, 78, 085114 – 085124.

[213] R. A. Koeppel, A. Baiker, C. Schild, A. Wokaun. Carbon Dioxide Hydrogenation over Au/ZrO_2 Catalysts from Amorphous Precursors: Catalytic Reaction Mechanism. *J. Chem. Soc., Faraday Trans.* 1991, 87, 2821 – 2828.

[214] X. Zhang, H. Shi, B.-Q. Xu. Catalysis by Gold: Isolated Surface Au^{3+} Ions are Active Sites for Selective Hydrogenation of 1,3-Butadiene over Au/ZrO_2 Catalysts. *Angew. Chem., Int. Ed*. 2005, 44, 7132 – 7135.

[215] Z.-P. Liu, C.-M. Wang, K.-N. Fan. Single Gold Atoms in Heterogeneous Catalysis: Selective 1,3-Butadiene Hydrogenation over Au/ZrO_2. *Angew. Chem., Int. Ed*. 2006, 45, 6865 – 6868.

[216] B. Yoon, H. Häkkinen, U. Landman, A. S. Wörz, J. M. Antonietti, S. Abbet, U. Heiz. Charging Effects on Bonding and Catalyzed Oxidation on Au_8 Clusters on MgO. *Science* 2005, 307, 403 – 407.

[217] Z. Yan, S. Chinta, A. A. Mohamed, J. P. Fackler, D. W. Goodman. The Role of F-Centers in Catalysis by Au Supported on MgO. *J. Am. Chem. Soc*. 2005, 127, 1604 – 1605.

[218] Z.-P. Liu, S. J. Jenkins, D. A. King. Origin and Activity of Oxidized Gold in Water-Gas-Shift Catalysis. *Phys. Rev. Lett*. 2005, 94, 196102 – 196105.

[219] S. Carrettin, P. Concepción, A. Corma, J. M. López-Nieto, V. F. Puntes. Nanocrystalline CeO_2 Increases the Activity of Au for CO Oxidation by Two Orders of Magnitude. *Angew. Chem., Int. Ed*. 2004, 43, 2538 – 2540.

[220] A. Del Vitto, G. Pacchioni, F. Delbecq, P. Sautet. Au Atoms and Dimers on the MgO(100) Surface: A DFT Study of Nucleation Defects. *J. Phys. Chem. B* 2005, 109, 8040 – 8048.

[221] A. S. Worz, U. Heiz, F. Cinquini, G. Pacchioni. Charging of Au Atoms on TiO_2 Thin Films from CO Vibrational Spectroscopy and DFT Calculations. *J. Phys. Chem. B* 2005, 109, 18418 – 18426.

[222] M. Sterrer, M. Yulikov, T. Risse, H.-J. Freund, J. Carrasco, F. Illas, C. Di Valentin, L. Giordano, G Pacchioni. When the Reporter Induces the Effect: Unusual IR Spectra of CO on Au_1/ MgO(001)/Mo(001). *Angew. Chem., Int. Ed*. 2006, 45, 2633 – 2635.

[223] H.-Y. T. Chen, S. Tosoni, G. Pacchioni. Adsorption of Ruthenium Atoms and Clusters on Anatase TiO_2 and Tetragonal ZrO_2 (101) Surfaces: A Comparative DFT Study. *J. Phys. Chem. C* 2015, 119, 10856 – 10868.

[224] H.-Y. T. Chen, S. Tosoni, G. Pacchioni. Hydrogen Adsorption, Dissociation, and Spillover on Ru_{10} Clusters Supported on Anatase TiO_2 and Tetragonal ZrO_2 (101) Surfaces. *ACS Catal*. 2015, 5, 5486 − 5495.

[225] A. Hofmann, S. J. Clark, M. Oppel, I. Hahndorf. Hydrogen Adsorption on the Tetragonal ZrO_2 (101) Surface: A Theoretical Study of an Important Catalytic Reactant. *Phys. Chem. Chem. Phys*. 2002, 4, 3500 – 3508.

[226] S. Tosoni, G. Pacchioni. Acetic Acid Ketonization on Tetragonal Zirconia: Role of Surface Reduction. *J. Catal.* 2016, 344, 465 – 473.

[227] J. Kondo, Y. Sakata, K. Domen, K. Maruya, T. Onishi. Infrared Study of Hydrogen Adsorbed on ZrO_2. *J. Chem. Soc., Faraday Trans*. 1990, 86, 397 – 401.

[228] C. Gionco, M. C. Paganini, E. Giamello, R. Burgess, C. Di Valentin, G. Pacchioni. Paramagnetic Defects in Polycrystalline Zirconia: An EPR and DFT Study. *Chem. Mater*. 2013, 25, 2243 – 2253.

[229] S. F. J. Cox, J. L. Gavartin, J. S. Lord, S. P. Cottrell, J. M. Gil, H. V. Alberto, J. Piroto Duarte, R. C. Vilao, N. Ayres de Campos, D. J. Keeble, et al. Oxide Muonics: II. Modelling the Electrical Activity of Hydrogen in Wide-gap and High-permittivity Dielectrics. *J. Phys.: Condens. Matter* 2006, 18, 1079 – 1119.

[230] C. Kilic, A. Zunger. N-type Doping of Oxides by Hydrogen. *Appl. Phys. Lett*. 2002, 81, 73 – 75.

[231] B. B. Straumal, A. A. Mazilkin, G. Svetlana, A. Protasova, A. A. Myatiev, P. B. Straumal, G. Schütz, P. A. Van Aken, E. Goering, B. Baretzky. Magnetization Study of Nanograined Pure and Mn-Doped ZnO Films: Formation of a Ferromagnetic Grain-Boundary Foam. *Phys. Rev. B* 2009, 79, 205206.

[232] Y. Matsumoto, M. Murakami, T. Shono, T. Hasegawa, T. Fukumura, M. Kawasaki, P. Ahmet, T. Chikyow, S. Koshihara, H. Koinuma. Room-Temperature Ferromagnetism in Transparent Transition Metal-Doped Titanium Dioxide. *Science* 2001, 291, 854 – 856.

[233] J. Zippel, M. Lorenz, A. Setzer, G. Wagner, N. Sobolev, P. Esquinazi, M. Grundmann. Defect-Induced Ferromagnetism in Undoped and Mn-Doped Zirconia Thin Films. *Phys. Rev. B* 2010, 82, 125208.

[234] A. Fert. Nobel Lecture: Origin, Development, and Future of Spintronic. *Rev. Mod. Phys.* 2008, 80, 1517 – 1529.

[235] H. Pan, J. B. Yi, L. Shen, R. Q. Wu, J. H. Yang, J. Y. Lin, Y. P. Feng, J. Ding, L. H. Van, J. H. Yin. Room-Temperature Ferromagnetism in Carbon-Doped ZnO. *Phys. Rev. Lett.* 2007, 99, 127201.

[236] L. Shen, R. Q. Wu, H. Pan, G. W. Peng, M. Yang, Z. D. Sha, Y. P. Feng. Mechanism of Ferromagnetism in Nitrogen-Doped Zno: First-Principle Calculations. *Phys. Rev. B: Condens. Matter Mater. Phys*. 2008, 78, 073306.

[237] J. G. Tao, L. X. Guan, J. S. Pan, C. H. A. Huan, L. Wang, J. L. Kuo, Z. Zhang, J. W. Chai, S. J. Wang. Density Functional Study on Ferromagnetism in Nitrogen-Doped Anatase TiO_2. *Appl. Phys. Lett.* 2009, 95, 062505.

[238] N. N. Bao, H. M. Fan, J. Ding, J. B. Yi. Room Temperature Ferromagnetism in N-Doped Rutile TiO_2 Films. *J. Appl. Phys*. 2011, 109, 07C302.

[239] H. Zhu, J. Li, K. Chen, X. Yi, S. Cheng, F. Gan. Nature of Charge Transport and P-Electron Ferromagnetism in Nitrogen-Doped ZrO_2: An Ab Initio Perspective. *Sci. Rep*. 2015, 5, 8586.

[240] M. A. Rahman, S. Rout, J. P. Thomas, D. McGillivray, K. T. Leung. Defect-Rich Dopant-Free ZrO_2 Nanostructures with Superior Dilute Ferromagnetic Semiconductor Properties. *J. Am. Chem. Soc.* 2016, 138, 11896 – 11906.

[241] B.Santara, P. K. Giri, K. Imakitab, M. Fujiib. Evidence of Oxygen Vacancy Induced Room Temperature Ferromagnetism in Solvothermally Synthesized Undoped TiO_2 Nanoribbons. *Nanoscale* 2013, 5, 5476 – 5488.

[242] G. Bouzerar, T. Ziman, J. Kudrnovský. Calculating the Curie Temperature Reliably in Diluted III-V Ferromagnetic Semiconductors. *Europhys. Lett*. 2005, 69, 812 – 818.

[243] L. M. Molina, M. D. Rasmussen, B. Hammer. *J. Chem. Phys.* 2004, 120, 7673 – 7680.

[244] Y. Lei, F. Mehmood, S. Lee, et al. Increased Silver Activity for Direct Propylene Epoxidation via Subnanometer Size Effects. *Science* 2010, 328, 224 – 228.

[245] M. Dion, H. Rydberg, E. Schroder, D. C. Langreth, B. I. Lundqvist. Van der Waals Density Functional for General Geometries. *Phys. Rev. Lett.* 2004, 92, 246401.

[246] R. Grau-Crespo, N. Cruz Hernandez, J. F. Sanz, N. H. De Leeuw. Theoretical Investigation of the Deposition of Cu, Ag, and Au Atoms on the ZrO_2(111) Surface. *J. Phys. Chem. C* 2007, 111, 10448 – 10454.

[247] G. C. Bond, P. A. Sermon. Gold Catalysis for Olefin Hydrogenation. *Gold Bull.* 1973, 6, 102 – 105.

[248] B. Nkosi, M. D. Adams, N. J. Coville, G. J. Hutchings. Hydrochlorination of Acetylene Using Carbon-Supported Gold Catalysts: A Study of Catalyst Reactivation. *J. Catal.* 1991, 128, 378.

[249] I. Andreeva, T. Tabakova, A. Andreev. Low-Temperature Water–Gas Shift Reaction over Au/α-Fe_2O_3. *J. Catal*. 1996, 158, 354.

[250] Q. Fu, H. Saltsburg, M. F. Stephanopoulos. Active Nonmetallic Au and Pt Species on Ceria-Based Water-Gas Shift Catalysts. *Science* 2003, 301, 935.

[251] M. D. Hughes, Y.-J. Xu, P. Jenkins, P. L. McMorn, P. Landon, D. I. Enache, A. Carley, et al. Tunable Gold Catalysts for Selective Hydrocarbon Oxidation Under Mild Conditions. *Nature* 2005, 437, 1132.

[252] D. I. Enache, J. K. Edwards, P. Landon, B. Solsona-Espriu, A. F. Carley, A. A. Herzing, M. Watanabe, C. J. Kiely, D. W. Knight, G. J. Hutchings. Solvent-Free Oxidation of Primary Alcohols to Aldehydes Using Au-Pd/TiO_2 Catalysts. *Science* 2016, 311, 362.

[253] M. C. Kung, R. J. Davis, H. H. Kung. Understanding Au-Catalyzed Low-Temperature CO Oxidation. Understanding Au-Catalyzed Low-Temperature CO Oxidation. *J. Phys. Chem. C* 2007, 111, 11767 – 11775.

[254] M. Haruta, T. Kobayashi, H. Sano, N. Yamada. Novel Gold Catalysts for the Oxidation of Carbon Monoxide at a Temperature Far Below 0ºC. *Chem. Lett*. 1987, 405 – 408.

[255] M. Okumura, S. Tsubota, M. Haruta. Preparation of Supported Gold Catalysts by Gas-Phase Grafting of Gold Acethylacetonate For Low-Temperature Oxidation of CO and of H_2. *J. Mol. Catal. A* 2003, 199, 73.

[256] H. Iddir, V. Komanicky, S. Ogut, H. You, P. Zapol. Shape of Platinum Nanoparticles Supported on $SrTiO_3$: Experiment and Theory. *J. Phys. Chem. C* 2007, 111, 14782 – 14789.

[257] C.-M. Wang, K.-N. Fan, Z.-P. Liu. Origin of Oxide Sensitivity in Gold-Based Catalysits: A First Principle Study of CO Oxidation over Au Supported on Monoclinic and Tetragonal ZrO_2. *J. Am. Chem. Soc*. 2007, 129, 2642 – 2647.

[258] T. V. W. Janssens, B. S. Clausen, B. Hvolbæk, H. Falsig, C. H. Christiensen, T. Bligaard, J. K. Nørskov. Insights into the Reactivity of Supported Au Nanoparticles: Combining Theory and Experiments. *Top. Catal*. 2007, 44, 15 – 26.

[259] N. Lopez, T. V. W. Janssens, B. S. Clausen, Y. Xu, M. Mavrikakis, T. Bligaard, J. K. Nørskov. On the Origin of the Catalytic Activity of Gold Nanoparticles for Low-Temperature CO Oxidation. *J. Catal.* 2004, 223, 232.

[260] M. Okumura, J. M. Coronado, J. Soria, M. Haruta, J. Conesa. EPR Study of CO and O_2 Interaction with Supported Au Catalysts. *J. Catal.* 2001, 203, 168.

[261] Z. P. Liu, X. Q. Gong, J. Kohanoff, C. Sanchez, P. Hu. Catalytic Role of Metal Oxides in Gold-Based Catalysts: A First Principles Study of CO Oxidation on TiO_2 Supported Au. *Phys. Rev. Lett.* 2003, 91, 266102.

[262] I. N. Remediakis, N. Lopez, J. K. Nørskov. CO Oxidation on Rutile-Supported Au Nanoparticles. *Angew. Chem.* 2005, 117, 1858 – 1860.

[263] L. M. Molina, B. Hammer. Some Recent Theoretical Advances in the Understanding of the Catalytic Activity of Au. *Appl. Catal. A: General* 2005, 291, 21 – 31.

[264] J. Gong, C. B. Mullins. Surface Science Investigations of Oxidative Chemistry on Gold. *Acc. Chem. Res.* 2009, 42, 1063 – 1073.

[265] Y. Maeda, Y. Iizuka, M. Kohyama. Generation of Oxygen Vacancies at a Au/TiO_2 Perimeter Interface During CO Oxidation Detected by in Situ Electrical Conductance Measurement. *J. Am. Chem. Soc.* 2013, 135, 906 – 909.

[266] L. R. Merte, M. Ahmadi, F. Behafarid, L. K. Ono, E. Lira, J. Matos, L. Li, J. C. Yang, B. Roldan-Cuenya. Correlating Catalytic Methanol Oxidation with the Structure and Oxidation State of Size – Selected Pt Nanoparticles. *ACS Catal*. 2013, 3, 1460 – 1468.

[267] Z. Yang, Z. Lu, G. Luo. First-Principles Study of the Pt/CeO_2 (111) Interface. *Phys. Rev. B: Condens. Matter Mater. Phys*. 2007, 76, 075421.

[268] Z. Yang, Z. Lu, G. Luo, K. Hermansson. Oxygan Vacancy Formation Energy at the Pd/CeO_2 (111) Interface. *Phys. Lett. A* 2007, 369, 132 – 139.

[269] I. X. Green. W. Tang, M. Neurock, J. T. Yates. Spectroscopic Observation of Dual Catalytic Sites During Oxidation of CO on A Au/TiO_2 Catalyst. *Science* 2011, 333, 736 – 739.

[270] M. A. Bollinger. M. A. Vannice. A Kinetic and DRIFTS Study of Low-Temperature Carbon Monoxide Oxidation over $Au\text{-}TiO_2$ Catalysts. *Appl. Catal. B* 1996, 8, 417.

[271] F. Solymosi. The Bonding, Structure and Reactions of CO_2 Adsorbed on Clean and Promoted Metal Surfaces. *J. Mol. Catal.* 1991, 65 (3), 337 – 358.

[272] X. Xia, R. J. Oldman, C. R. A. Catlow. Oxygen Adsorption and Dissociation on Yttria Stabilized Zirconia Surfaces. *J. Mater. Chem.* 2012, 22, 8594.

[273] M. Anpo, M. Che, E. Fubini, E. Garrone, E. Giamello, M. C. Paganini. Generation of Superoxide Ions at Oxide Surfaces. *Top. Catal.* 1999, 8, 189.

[274] L. N. Kantorovich, A. L. Shluger, J. Gunster, P. Stracke, D. W. Goodman, V. Kempter. Mg Clusters on MgO Surfaces: Study of the Nucleation Mechanism with MIES and Ab Initio Calculations. *Faraday Discuss.* 1999, 114, 173.

[275] Y. F. Li, U. Aschauer, J. Chen, A. Selloni. Adsorption and Reactions of O_2 On Anatase TiO_2. *Acc. Chem. Res.* 2014, 47, 3361 – 3368.

[276] E. Carter, A. F. Carley, D. M. Murphy. Evidence for O_2-Radical Stabilization at Surface Oxygen Vacancies on Polycrystalline TiO_2. *J. Phys. Chem. C* 2007, 111, 10630 – 10638.

[277] L. Brewer. A Most Striking Confirmation of the Engel Metallic Correlation. *Acta Metall*. 1967, 15, 553.

[278] W. Hume-Rothery. The Engel-Brewer Theories of Metals and Alloys. *Prog. Mater. Sci.* 1968, 13, 229.

[279] M. Antlanger, W. Mayr–Schmölzer, J. Pavelec, F. Mittendorfer, J. Redinger, P. Varga, U. Diebold, M. Schmid. Pt_3Zr (0001): A Substrate for Growing Well-Ordered Ultrathin Zirconia Films by Oxidation. *Phys. Rev. B: Condens. Matter* 2012, 86, 035451.

[280] H. Li, J. I. Jake-Choi, W. Mayr–Schmölzer, C. Weilach, C. Rameshan, F. Mittendorfer, J. Redinger, M. Schmidt, G. Rupprechter. Growth of an Ultrathin Zirconia Film on Pt_3Zr Examined by High-Resolution X-ray Photoelectron Spectroscopy, Temperature-Programmed Desorption, Scanning Tunneling Microscopy, and Density Functional Theory. *J. Phys. Chem. C*, 2015, 119, 2462.

[281] E. Napetschnig, M. Schmid, P. Varga. Ultrathin Alumina Film on Cu 9at% Al (111). *Surf. Sci.* 2008, 602, 1750.

[282] V. Maurice, M. Salmeron, G. A. Somorjai. The Epitaxial Growth of Zirconium Oxide Thin Films on Pt (111) Single Crystal Surfaces. *Surf. Sci.* 1990, 237, 116.

[283] K. Meinel, A. Eichler, S. Förster, K. M. Schindler, H. Neddermeyer, W. Widdra. Surface and Interface Structures of Epitaxial ZrO_2 Films on Pt (111): Experiment and Density-Functional Theory Calculations. *Phys. Rev. B* 2006, 74, 235444.

[284] K. Meinel, A. Eichler, K. M. Schindler, H. Neddermeyer. STM, LEED, and DFT Characterization of Epitaxial ZrO_2 Films on Pt (111). *Surf. Sci.* 2004, 562, 204.

[285] K. Meinel, K. M. Schindler, H. Neddermeyer. Growth, Structure and Annealing Behavior of Epitaxial ZrO_2 Films on Pt (111). *Surf. Sci. 2003,* 532, 420.

[286] M. Tomita, T. Tanabe, S. Imoto. An AES Study of Surface Oxidation of Zirconium. *Surf. Sci*. 1989, 209, 173.

[287] C. O. Gonzalez, E. A. Garcia. An X-Ray Photoelectron Spectroscopy Study of the Surface Oxidation of Zirconium. *Surf. Sci.* 1988, 193, 305.

[288] C. Morant, J. M. Sanz. L. Galan, L. Soriano, F. Rueda. An XPS Study of the Interaction of Oxygen with Zirconium. *Surf. Sci*. 1989, 218, 331.

[289] B. Predel, Pt–Zr (Platinum–Zirconium), Springer Materials – The Landbolt–Börnstein Database. Doi: 10.1007/10542753_2542.

[290] W. J. Qi, R. Nieh, B. H. Lee, L. Kang, Y. Jeon, J. C. Lee. Electrical and Reliability Characteristics of ZrO_2 Deposited Directly on Si for Gate Dielectric Application. *Appl. Phys. Lett.* 2000, 77, 3269.

List of Publications

- A. Ruiz Puigdollers, P. Schlexer, G. Pacchioni. Gold and Silver Clusters on TiO_2 and ZrO_2 (101) Surfaces: Role of Dispersion Forces. *J. Phys. Chem. C* 2015, 119, 15381.
- P. Schlexer, A. Ruiz Puigdollers, G. Pacchioni. Tuning the Charge State of Ag and Au Atoms and Clusters Deposited on Oxide Surfaces by Doping: A DFT Study of the Adsorption Properties of Nitrogen- and Niobium-Doped TiO_2 and ZrO_2. *Phys. Chem. Chem. Phys*. 2015, 17, 22342.
- A. Ruiz Puigdollers, F. Illas, G. Pacchioni. Structure and Properties of Zirconia Nanoparticles from Density Functional Theory Calculations. *J. Phys. Chem. C* 2016, 120, 4392.
- A. Ruiz Puigdollers, F. Illas, G. Pacchioni. Effect of Nanostructuring of the Reactivity of Zirconia: A DFT+U Study of Au Atom Adsorption. *J. Phys. Chem. C* 2016, 120, 17604.
- A. Ruiz Puigdollers, S. Tosoni, G. Pacchioni. Turning a Nonreducible into a Reducible Oxide via Nanostructuring: Opposite Behavior of Bulk ZrO_2 and ZrO_2 Nanoparticles Toward H_2 Adsorption. *J. Phys. Chem. C* 2016, 120, 15329.
- A. Ruiz Puigdollers, F. Illas, G. Pacchioni. ZrO2 Nanoparticles: A Density Functional Theory Study of Structure, Properties and Reactivity. *Rend. Fis. Acc. Lincei* 2017, 28, 19.
- A. Ruiz Puigdollers, G. Pacchioni. CO Oxidation on Au Nanoparticles Supported on ZrO_2: Role of Metal/Oxide Interface and Oxide Reducibility. *ChemCatChem* 2017, 9, 1.
- A. Ruiz Puigdollers, G. Pacchioni. Reducibility of ZrO_2/Pt_3Zr and ZrO_2/Pt 2D Films Compared to Bulk Zirconia: A DFT+U Study of Oxygen Removal and H_2 Adsorption. *Nanoscale* 2017, 9, 6866.
- A. Ruiz Puigdollers, F. Illas, G. Pacchioni. Reduction of Hydrogenated ZrO_2 Nanoparticles by Water Desorption. *ACS Omega* 2017, 2, 3878.
- A. Ruiz Puigdollers, P. Schlexer, S. Tosoni, G. Pacchioni. Increasing Oxide Reducibility: The Role of Metal/Oxide Interfaces in the Formation of Oxygen Vacancies. *ACS Catal*. 2017, 7, 6493.
- S. Tosoni, H.-Y. Tiffany Chen, A. Ruiz Puigdollers, G. Pacchioni. TiO_2 and ZrO_2 in Biomass Conversion: Why Catalyst Reduction Helps. *Philos. Trans.* 2017, In press.